Phase-transitions in amphiphilic self-assembling systems

A thesis submitted in partial fulfillment

of the requirements for the degree

of

Doctor of Philosophy

by

Guy Jacoby

Under the supervision of

Prof. Roy Beck

Presented to the senate of Tel Aviv University

May 2020

This work was carried out under the supervision of Prof. Roy Beck.

Abstract

Amphiphiles are molecules that possess hydrophilic and hydrophobic chemical groups. This property grants them the ability to spontaneously self-organize or *self-assemble* into various structures, such as micelles, vesicles, rods and bi-continuous structures. These molecular aggregates, also known as mesophases, are widely found in nature, for example in the cell or nucleus membranes. Amphiphiles are also utilized in various applications in nanotechnology, biomedicine and materials science.

The thermodynamic free-energy of self-assembly can be driven by either enthalpy or entropy, but is usually associated with weaker, non-covalent interactions, such as van der Waals, hydrogen bonds or entropic forces. Self-assembled systems are also characterized by their thermodynamic stability, i.e. the assembled structures are thermodynamically stable compared to the monomeric form. These two properties lead self-assembled systems to be sensitive to the external environment, but also flexible to the rearrangement of the molecules into a new phase, as determined by the thermodynamics.

Phase-transitions in self-assembled systems can be brought about by changes to thermodynamic variables, such as temperature and pressure, or to the environmental conditions of the assembly, such as salt concentration or pH. These parameters can be used to probe the phase-behavior of the system, study its unique physical properties and examine its applicability.

Although phase-transitions in amphiphilic systems have been extensively studied, and many of them can be modeled using well-established theoretical models, new systems displaying non-classical dynamics pose an interesting challenge. In this work, I experimentally studied two types of amphiphiles and the properties of their phase-transitions using various soft-matter characterization techniques. In addition, I propose a model to describe each of the underlying mechanisms that bring about their phase-transition and its characteristics.

The first amphiphilic system is comprised of phospholipids, a naturally occurring biomolecule best known as the main constituent of the lipid cell membrane. Specifically, I experimentally investigate a metastable liquid-crystalline phase, with a lifetime on the order of tens of hours or more, and its ensuing cooperative transition into the stable crystalline phase. I show that there are several timescales associated with the dynamics of the phenomenon, in contrast to what is expected from the classical theory of nucleation. The metastability is shown to be manipulatable by changing various system parameters, such as the number of lipid components, salt concentration and quenching temperature. I detail a model describing the mechanism behind the delay in crystallization; a mechanism that could be generalized to systems with similar properties.

The second type of amphiphile studied in this work is a synthetic hybrid molecule, having an intrinsically disordered peptide as a headgroup and phospholipid-like hydrocarbon chains. This molecule, belonging to a recently studied class of molecules named Peptide Amphiphiles, was designed with two goals in mind. The first is to utilize its self-assembly to study the interactions between a similarly interesting class of molecules – intrinsically disordered proteins. The second goal, which is more in line with recently published work, is to design novel peptide amphiphiles for biomedical applications.

I experimentally investigate two variants of peptide amphiphiles and show the existence of a spherical-to-cylindrical micelle structural phase-transition, brought about by a change in pH. I propose a free-energy model to describe the balance of electrostatic and elastic forces, which can bring about the transition. In addition, I use a model to predict sequence-specific interactions between neighboring headgroup peptides in the self-assembled structures. Based on the predictions, two modifications were introduced to the headgroup peptide, which led to macroscopic changes to the inter-particle interactions. These changes highlight the sensitivity of the assembly properties to the interactions of the headgroups.

The findings shown in this work demonstrate the richness and complexity one encounters in the study of phase-transitions in amphiphilic systems. On one hand, even systems that can be thought of as having been exhaustively studied can display unique and unexplored dynamics. On the other, I believe amphiphilic systems, and specifically peptide amphiphiles, have only begun to show their true potential, and that my work will help pave the way for future investigations of their use in biomedical applications.

Acknowledgements

I would like to thank many people whom helped me on my journey, culminating in this work.

First, my past lab mates who were my family away from home for several years. To Ram, for helping me in every stage of my journey, but mostly for the endless discussions on an endless list of topics. You share my curiosity and passion for learning everything, whenever possible. It was a great pleasure diverging with you. To Micha, for always being patient with my questions, regardless of how trivial or time-consuming they were for you. You were a big brother and a mentor when I needed one. To Eti, for bringing sanity, perspective and a shoulder to 'cry' on. You don't know how much you made my time happy at the lab. Oh, and for teaching me almost everything I know about biology and biochemistry. To Rona, for taking me under your wing in the beginning of my journey. Your dedication, hard work and especially discipline cannot be matched. To Adi, my past lab manager, for helping me with every and anything I needed. For knowing how to keep me in line, but also sharing my coffee breaks. To Yoni, for being like a younger brother, and teaching me that being Vegan is not only possible, it can also be fun. To Stive, for being cool as a French cucumber, merci beaucoup. And to the rest of the students who came and went, but each made my time better in his or her own way.

To the present lab members, who keep the fire going. To Tamara, for being my partner in science and friend in the last couple of years. Your free spirit and cheerfulness were always there to contradict my seriousness. To Gil, for being apathetically passionate about science and always willing to help. To Benjamin, for being religiously pragmatic, and occasionally diverging with Ram and me. It was a pleasure. And to the rest of the students and post-docs, thank you each for the conversations and interest.

To the Peer lab in the earlier days. Especially to Keren Cohen, for spending the time mentoring me and showing me how much fun fat can be, and to Meir Goldsmith, for endless patience, knowledge and big laughs (in an Irish accent).

To the Amir lab in the later days. Especially to Prof. Roey Amir and Merav Segal Asher for helping me keep the later stages of my journey just as interesting and challenging as the beginning, and for letting me rant endlessly about micellar phase-transitions. Merav, it was a big pleasure working with you, and mazal tov!

To Prof. Ishi Talmon and his group for a fruitful collaboration and showing me the wonders of Cryo-TEM firsthand.

To Prof. Dganit Danino's group for collaborating on the study of the self-assembly of the peptide amphiphiles and the metastability of the phospholipids. Especially to Prof. Dganit Danino and Dr. Irina Portnaya for the insightful discussions.

To Prof. Ehud Gazit, Dr. Sudipta Mondal, Dr. Kai Tao, Dr. Santu Bera and Dr. Michal Pellach for a longstanding collaboration that made my science truly interdisciplinary.

To the Center for Nanoscience and Nanotechnology staff and members for making my workplace as enjoyable as it could be.

To the TAU biosoft community, for providing the framework to learn from many people on many more subjects. The biosoft seminars were one of the highlights of my week for several years. Especially to Prof. Haim Diamant and Prof. Michael (Misha) Kozlov, for their guidance, patience and the chance to finally dabble in a bit of theory.

Finally, I would like to deeply thank my advisor and friend, Prof. Roy Beck, for making this journey possible. I came into your lab a silly and ‘slightly’ immature kid, but leaving as a husband and father. I’m happy I could share this with you, and grateful you were understanding and patient when I needed it. Thank you for teaching me all kinds of physics and showing me how much fun it can be. Thank you for always having my back, and providing the necessary support to flourish. Thank you for pushing me when I needed it (and there were times I really needed it) and for knowing when to let me explore on my own, fall and get back up. Thank you for introducing me to a great many interesting people, from whom I learned a lot. But most of all, thank you for helping me feel proud of my work. I will never forget it.

Table of Contents

Chapter 1 Introduction

1.1 Amphiphiles and their self-assembly

Amphiphiles are molecules that are made up of two distinct parts, hydrophilic and hydrophobic. The hydrophilic part is comprised of polar chemical groups and is usually referred to as the headgroup of the amphiphile, due to it "sticking out" into the surrounding aqueous environment. The hydrophobic part is made up of non-polar chemical groups, most notably hydrocarbon chains like in the case of lipids, and is usually referred to as the tail group. This water-attracting-water-repelling property of amphiphiles grants them the ability to self-assemble – the propensity to spontaneously organize into macromolecular structures that minimize the contact of the hydrophobic parts with water.

There is a wide variety of molecular aggregates formed in the process of self-assembly, such as micelles, bilayers, vesicles and continuous phases (Figure 1). The forces that hold amphiphilic molecules together in these structures are generally weaker than covalent and ionic bonds, hence these structures are usually considered as *soft matter*[1] – systems that are easily deformable due to their sensitivity to thermal fluctuations or external stimuli. The typical interactions associated with the self-assembly process include van der Waals, hydrophobic, hydrogen-bonding and screened electrostatics[2]. Since self-assembly occurs in solution, the solution conditions, e.g., salt concentration or pH, will set the stage for the interaction of molecules within aggregates and the interaction between aggregates.

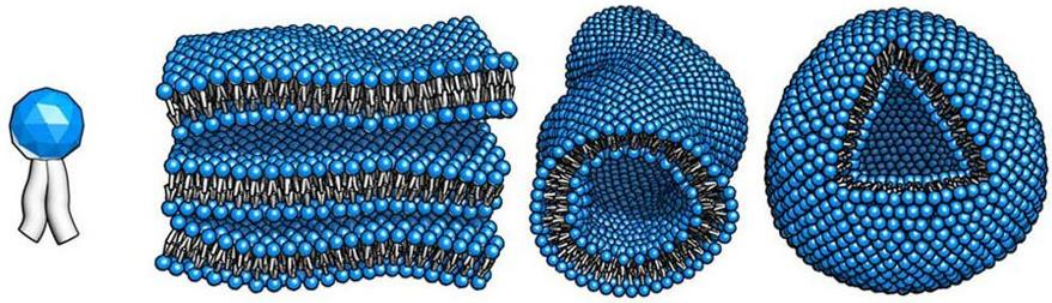

Figure 1. Schematic illustration of an amphiphile (left) and various self-assembled mesophases. Figure adapted from Ref. 3.

In order for self-assembly to initiate, the concentration of molecules in solution must exceed the critical micelle concentration (CMC). The CMC is set by the difference in chemical potential of the molecules in different sized aggregates. Below the CMC the molecules in solution will be isolated, however, above it, the concentration of monomeric structures (single molecules) will be fixed, and the fraction of molecules in aggregates will grow[1].

When amphiphilic molecules assemble into well-defined structures, such as micelles and bilayers, they interact via two opposing sets of forces. The interfacial tension at the hydrocarbon-water interface, which drives the molecules to associate, is countered by the hydrophilic, ionic and steric forces between the headgroups and between the tail groups. This competition of forces sets the optimal headgroup area – the area that the headgroup occupies to shield the hydrophobic core from water.

The adopted structure and morphology, however, will not be determined by this balance of forces alone. Given an optimal headgroup area, the geometry of the molecule is what determines which structures the molecules will favorably assemble into[4]. These geometrical considerations are manifested as a parameter called the "packing parameter". It is defined as the ratio of the volume the hydrophobic tail group occupies – v, to the product of the optimal headgroup area – a_0 – and the maximal effective chain length – l_c. The packing parameter, $p = \frac{v}{a_0 l_c}$, represents the ratio of the actual volume occupied by the hydrophobic tails to the maximal effective volume the hydrophobic tails can occupy. When $p < 1$, the amphiphiles form micelles or bicontinuous phase (e.g., cubic phase) with normal topology (hydrophobic core). When $p > 1$, they form the same phases but with inverse topology, i.e., the hydrophilic parts make up the core of the structures. When $p \approx 1$, amphiphiles form membranous structures with a large radius of curvature compared to the thickness of the membrane, namely, lamellar phases[1] (Figure 2).

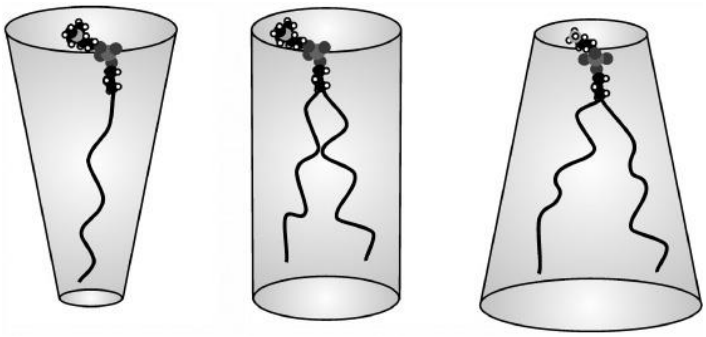

Figure 2. Illustration of the geometric shape of amphiphiles determined by their packing parameter. Left to right: coned shape ($p < 1$), cylindrical shape ($p = 1$) and inverted cone shape ($p > 1$). Figure adapted from Ref. 5.

1.2 Phospholipids

One of the most prominent classes of natural amphiphilic molecules are the lipids. These molecules have several main biological roles, including storing energy, signaling and serving as the building blocks of cell membranes[6]. The lipid class consists of many subclasses, including glycerides, sterols (e.g., cholesterol), waxes, glycolipids, and most relevant for this work, phospholipids.

Phospholipids are best known as a major constituent of cell membranes. Their hydrophilic part consists of a phosphate group, which is connected to an additional chemical group, such as an ethanolamine (PE), glyercol (PG) or choline (PC) (Figure 3). Their tails generally consist of two fatty acids of different lengths and states of saturation (the existence of double bonds in the hydrocarbon chains, as depicted in Figure 3). This results in a plethora of variants with distinct physiochemical properties. Cell membranes usually encompass a large number of variants, each contributing uniquely to the overall properties of the membrane to form a complex environment, suited for housing many other membranal molecules.

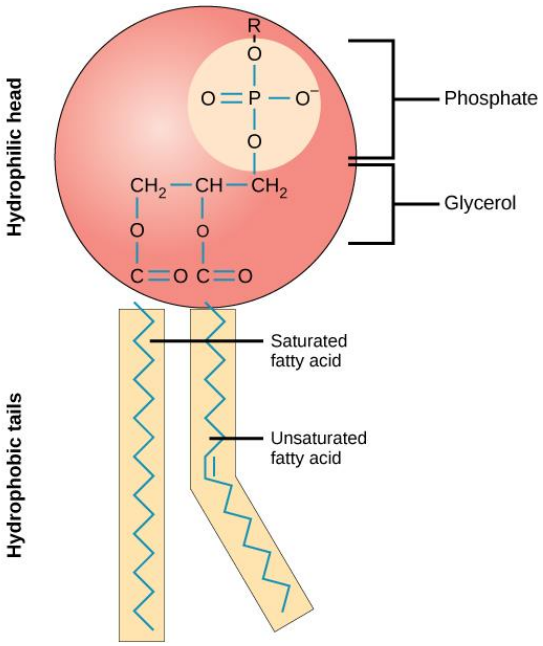

Figure 3. Schematic illustration of the chemical structure of a phospholipid. R denotes the headgroup connected to the phosphate. Figure adapted from Ref. 7.

Aside from the biological aspects of studying the building blocks of living systems, phospholipids, and the structures they form, are interesting from a biomedical point of view. They have been key components in the design of biomedical systems, such as targeted drug-delivery systems[8]. Because these biomolecules naturally form nanometer sized particles, they can be easily utilized as a platform on which to build “smart nano-carriers”, capable of transporting hydrophobic/hydrophilic cargo in a targeted manner throughout the body.

To better understand these molecules and harness their properties, they have been physically and chemically studied since the 1960's[9]. Since the physicochemical properties of these molecules depend on their structure, as stated above, many of these phospholipids were studied separately, and then combined to form more complex systems. Many experimental characterization techniques have been employed to understand the interactions between the molecules, as well as the structures they form, such as X-ray and neutron scattering[10], calorimetry, nuclear magnetic resonance (NMR) and electron microscopy (some of which will be discussed in Chapter 2). These techniques can be used to determine the phase adopted by the molecules, depending on the thermodynamic and environmental conditions[11].

In Section 3.1, I will discuss two predominant lamellar phases, namely, the liquid-crystalline (L_α) and crystalline (L_c) phases. Both have the phospholipids organized in bilayers, which are stacked together to form a three-dimensional structure, however, they differ in their degrees of freedom and spatial symmetry. In the L_α phase, the bilayers are curved and form concentric shells (onion-like) with layers of water between the bilayers (Figure 4). The bilayers are spatially correlated as a one-dimensional crystalline lattice in the radial direction, with a repeating distance between one membrane and the next. However, in the plane of the membranes, the lipids are diffusing freely in a liquid-like manner (a typical example of a liquid-crystal found in a smectic A phase[12]). The L_c phase, on the other hand, has the molecules organized in a three-dimensional ordered crystalline structure. The lipids still form bilayers, but now the membranes are flat and stacked together with a minimal amount of water between them. In addition, the lipids are "frozen" in place and are no longer diffusing in the membrane (Figure 4). A third lamellar phase worth mentioning is the so-called 'gel' phase (L_β). It is similar to the L_α phase, however it has a lower degree of symmetry, since the lipids adopt some short-range correlations within the membrane.

Figure 4. Left: Two stacked phospholipid membranes in a multi-lamellar vesicle. The membranes are curved bilayers with a water layer in-between, where the molecules are in liquid-like disorder in the plane of the membranes (L_α). Right: Stacks of flat bilayers with long-range molecular spatial correlations composing the ordered crystalline (L_c) phase.

1.3 Peptide amphiphiles

The second type of amphiphile, discussed in Section 3.2, is an example of a recently explored class of synthetic amphiphiles, namely, peptide amphiphiles[13] (PAs). Designed to self-assemble into functional structures, the molecules' headgroup, usually a bio-inspired peptide engineered to fulfill one or more active roles, is chemically conjugated to a hydrophobic tail group. The tails are usually single or double chain fatty acids like those found in lipids. Due to their highly flexible design scheme, PA self-assemblies can act as organic scaffolds for bone-like mineralization[14], anisotropic actuators mimicking skeletal muscle[15], produce new versatile soft materials[16], and enhance neural progenitor cell differentiation into neurons[17]. PAs can contain spacers or linkers in their design, connecting the hydrophobic tails from the functional headgroup[18,19], or be conjugated to an "external" functional group such as an MRI contrast agent[20] (Figure 5).

Comprehensive research is done to understand the properties and roles of the different parts of PAs and their contribution to the specific self-assembly[21,22]. In many cases, the bio-inspired peptide is designed or derived from a protein with some degree of secondary structure[23]. Nonetheless, PA headgroups are not exclusively bio-inspired, and can be made to be any polypeptide sequence, including intrinsically disordered peptides as we shall see.

However, to better understand why these amphiphiles were designed and studied, I will first briefly discuss proteins in general and a subtype of proteins called intrinsically disordered proteins.

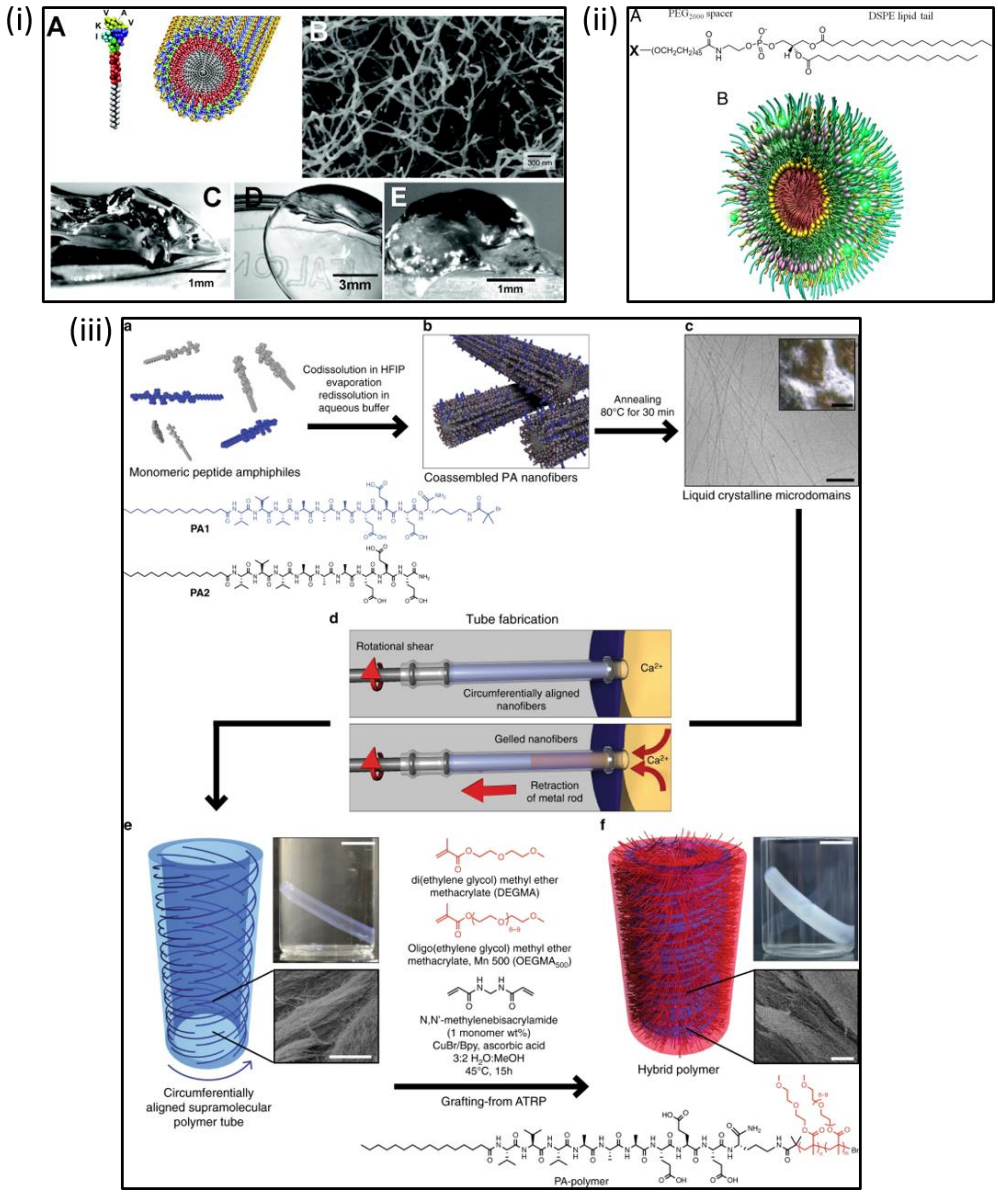

Figure 5. Examples of PA designs, the structures they form and the materials they are used to create. PAs designed to produce (i) a three-dimensional scaffold for cell differentiation, (ii) targeted micellar nanoparticles for in-vivo imaging and therapeutics, and (iii) hybrid muscle-inspired anisotropic actuators. Figures adapated from Refs. 15,17,18, respectively.

1.3.1 Proteins

Proteins are natural polymers found ubiquitously in living cells. Formed in the ribosome via the transcription-translation process, they are a linear sequence of amino acids (i.e. polypeptides) bound together by the covalent peptide bond (Figure 6). The amino acids constituting the protein are called residues, and each type of amino acid has a unique chemical group called a side-chain. These side chains can come from one of 4 general groups: negatively or positively charged, polar (hydrophilic) and non-polar (hydrophobic).

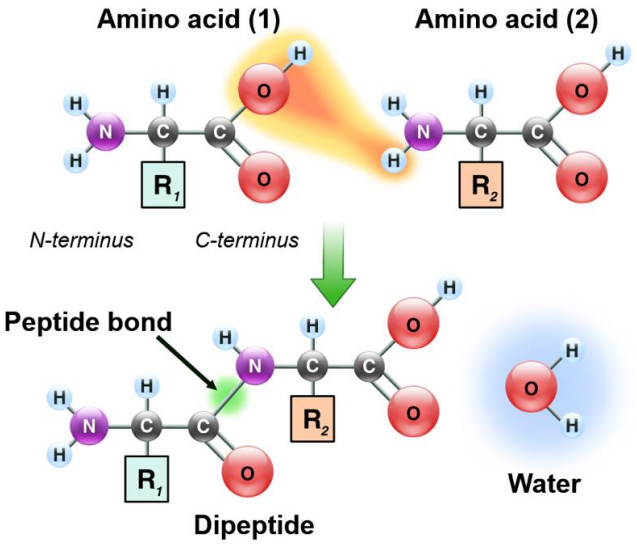

Figure 6. Peptide bond formation. Figure adapted from Ref. 24.

Proteins serve as the molecular machinery in living organisms, performing many roles in the cell[6]. To fulfill their roles, the linear sequence of amino acid can fold into one or more specific spatial conformations driven by a number of non-covalent interactions such as hydrogen bonding, ionic interactions, van der Waals forces, and hydrophobic packing. The final form of the protein structure is generally thought of as having four levels, the first being the specific amino acid sequence. The second is called "secondary structure", where local regions within the sequence usually fold into a few distinct structures, the most famous of which are the α-helix and β-sheet. The "tertiary structure" is the global structure adopted by the protein, which has been generally associated with its direct biological function. The "quaternary structure" is the assembly of several proteins into a macromolecular functional structure.

1.3.2 Intrinsically disordered proteins

In the past, it was thought that only a single conformation of the protein, namely, the 'native' conformation, is required for the protein to function. However, this rigid structure-function relationship, which is the central idea behind the field of structural biology, has been put to question in recent decades[25]. An increasingly large number of proteins have been found to fully, or partially, lack a fixed or ordered structure[26]. As such, these proteins have been deemed 'intrinsically disordered' proteins (IDPs) or proteins containing intrinsically disordered regions (IDRs). Another, more operational definition of an IDP, is a protein that doesn't have a single functional conformation, but rather it can fold into an ensemble of functional conformations depending on the setting. This flexibility in possible conformations is the result of relatively weaker and transient interactions between proteins segments.

The disordered, flexible and transient nature of their interactions make IDPs and IDRs better suited for certain roles than structured proteins. The function of IDPs and IDRs can be classified into six categories[27]: entropic chains, display sites, chaperons, effectors, assemblers and scavengers. The family of neurofilament proteins found in the cytoskeleton of neuronal cells are an example of proteins that contain a "head" domain that drives their self-assembly into filaments and a "tail" domain that serves as a shock absorber (i.e. entropic springs) within the cell[28].

Studies of the distribution of protein disorder in different organisms show that a large part (~37–50%) of human amino acids are predicted to be disordered[26,27]. This means that instead of being exceptionally unique and rare exceptions, IDPs/IDRs are highly prevalent in nature. Due to their important biological functions and central positions in protein interaction networks, many IDPs have been tied to human diseases. The prevalence of intrinsic disorder was shown in proteins associated with cancer, cardiovascular disease, neurodegenerative diseases and amyloidoses[29]. They have also been found to constitute liquid-like condensations within cells (also termed membraneless organelles) that play a role in intracellular organization. These droplets might also be tied to pathologies exhibiting protein aggregation[30].

The lack of rigid structures in IDPs is due first and foremost to the sequence of amino acids[29]. Studies have shown that IDPs and IDRs have distinct compositional biases, as they are enriched with charged and polar amino acids and depleted in bulky hydrophobic groups[31]. This combination of low mean hydrophobicity (leading to a low driving force of protein compaction) and high net charge (which causes strong electrostatic repulsion) will significantly decrease the chance of compact structure formation in the protein. Strong polyelectrolytes fit this description well, and indeed they tend to take the form of swollen coils. However, most of the IDPs are actually polyampholytes, which are enriched with positively and negatively charged residues but can have a net charge close to zero[32]. Simulations have shown that the degree to which the protein is a polyampholyte, either strong or weak, will affect the conformational preference of the protein[32]. Weak polyampholytes will form globules, whereas strong polyampholytes are expected to be random-coil-like if oppositely charged residues are well mixed in the linear sequence. Otherwise, one can expect compact or semicompact conformations (e.g. hairpins).

Predicting disordered regions from amino acid sequence is an important part of the study of IDPs/IDRs, as it allows for genome-wide scale analysis and provides initial hypotheses about the presence of structural disorder in proteins[33]. Currently, there are four general prediction strategies: (i) Scoring function based on physiochemical properties, such as interaction strength or hydrophobicity[34]. (ii) Machine learning based algorithms, which can output the propensity for disorder using a classifier (usually a neural net), based on sequence 'features' such as

evolutionary conservation (which is suppressed in IDPs when compared to structured proteins), predicted secondary structure and solvent accessibility[35]. (iii) Structure-based methods, which use predicted structures or templates[36]. (iv) Meta-predictors, which take as input other predictions and compute a prediction using voting, or combining other predictions with sequence derived properties to compute a prediction using a classifier[37].

In Section 3.2.2.2, I will show the results of two types of predictors used to predict disorder probability of a sequence.

1.3.3 Intrinsically disordered peptide amphiphiles (IDPAs)

Envisioning systems with intricate and precise self-organization potential requires better nanostructure fabrication and processing. A primary limitation of current block copolymer synthesis is the lack of general methods for producing precise chain structure (i.e. sequence control) and hence complex function. In contrast, the design and synthesis of IDPAs, benefits from the use of relatively short sequences that are easier to manufacture, while still retaining rich functionality. On the other hand, natural lipids are widely available and easy to produce, but lack the complex functionality that peptides possess. Moreover, an IDP headgroup greatly benefits from the sensitivity of peptides to changes in the environment, such as pH, temperature and ion concentration.

As mentioned earlier, PAs are synthetic amphiphiles that combine the functionality and flexibility of peptides with the naturally diverse set of hydrophobic tail groups already found in nature. Since there are 20 natural amino acids, there is practically an infinite number of possible sequences, even for short peptides such as the one studied in this work. This opens the door for novel design of PAs. Naturally, the design of headgroups can be inspired by biology, utilizing the immense pre-existing knowledgebase of proteins. In particular, IDPs are a good starting point due to their properties, discussed in Section 1.3.2.

In these respects, IDPAs are interesting candidates for the design of tunable and functional self-assembling systems that can form new materials and be used for applications. However, to the best of my knowledge, the few examples showing the potential of such molecules so far have only scratched the surface[38–40].

1.4 Structural phase-transition

1.4.1 Nucleation process

Nucleation is the main process by which a first-order phase-transition takes place. It is the process of forming a new phase in an old phase, driven by the difference in the free-energy of the phases. The process involves the formation of nuclei of the new phase in the volume of the old phase. A prominent feature of nucleation is the metastability of the old phase, i.e. the transformation requires passage over an energy barrier. This can be understood by considering the changes in the free-energy associated with the formation of the nucleus.

The most basic description of this process is called the classical nucleation theory[41] (CNT). Only a few key assumptions are needed for CNT: dominant short-range interactions, smooth interfaces (capillarity approximation), and that the nucleus has similar properties to the final bulk phase. The dynamics are then described as a single stochastic excitation process that governs the transition. The free-energy is a competition between two contributions. The first is a negative term, which favors the transition of the molecule in the bulk to the new phase due to its lower chemical potential. The second is a positive contribution, usually referred to as the interfacial free-energy (or surface tension), and it accounts for the penalty of creating an interface between the new and old phases. In three dimensions, therefore, the change in the free-energy is a sum of the bulk term (ΔF_b) and the interface term (ΔF_i):

$$\Delta F(R) = \Delta F_b(R) + \Delta F_i(R) = -\frac{4\pi}{3}R^3\Delta g + 4\pi R^2\gamma\,, \tag{1}$$

where R is the radius of the nucleus, Δg is the change in the bulk chemical potential per unit volume, and γ is the interfacial free-energy per unit area. It follows that there will be a critical size of the nucleus, $R^* = 2\gamma/\Delta g$, beyond which the nucleus will become stable. The rate at which nucleation occurs is proportional to $e^{-\frac{\Delta F^*}{k_B T}}$, where $\Delta F^* = \Delta F(R^*)$ is the free-energy at the critical size (or the free-energy barrier). In the absence of external perturbations, the metastable-to-stable energy barrier can be overcome by spontaneous thermal fluctuations. Therefore, in the bulk, nucleation is initiated by an independent stochastic process, resulting in an unpredictable and uncontrollable phase-transition.

Despite its simplifying assumptions and basic description of the interactions, when applicable, CNT can properly capture the quantitative features of the nucleation process of many systems. Mineral crystal formation[42–44], virus capsid assembly[45], and protein nucleation[46,47] are examples of phase transition dynamics that can be successfully modeled by CNT.

However, there is an increasing number of systems displaying nucleation processes that do not conform to this classical picture. Complex dynamics can arise due to intermediate states leading to multi-step nucleation[48–50], or long-range interactions that can result in macroscopic nucleation[51] or a cooperative delayed transition[52,53]. Such dynamics may require an extension of the classical theory or in some cases a comprehensive revision. Examples of such complex dynamics can be found in self-assembled amphiphilic systems, which display long-lived metastable phases upon temperature change.

1.4.2 Metastability in phospholipids

Ideally, a phase-transition takes place between two phases, each of them in thermodynamic equilibrium. This means that the transition should be reversible and follow the same pathway of equilibrium transition states in both directions. However, over the years, a large number of lipid systems have shown an 'irreversibility' of some of its transitions, at least in usual experimental time scales[54]. This has made the task of achieving thermodynamic reversibility, in experiment, quite difficult.

The melting transition between the L_β and L_α phases is an example of a 'fast' transition (on the order of seconds or minutes), occurring on similar time scales in both directions of the transition. However, the L_α/L_β to L_c transition can exhibit very slow dynamics upon cooling below the transition point, on the order of several hours or more[55–60]. The physical reasons behind these slow dynamics are still not known, including whether they can be attributed to very slow kinetics or if the parent phases are truly metastable[54]. Many rate-limiting factors have been suggested over the years, such as long hydration/dehydration times, slow reformation of hydrogen bond networks between lipid polar groups and low rate of appearance of critical size nuclei of the new phase[11,54,56,61]. Regardless of the physical reason, the phenomenological deviations from equilibrium are highlighted by the long-lived metastable states.

One such phospholipid displaying these non-equilibrium transitions is dilauroyl-phosphoethanolamine (DLPE). A fresh sample of DLPE in solution is found in the low energy L_c phase at temperatures below $T_{c\rightarrow\alpha} = 43°C$ (melting temperature). When heated above $T_{c\rightarrow\alpha}$, the molecules undergo a melting transition to the L_α phase. It was shown that if the same sample is then cooled to a quenching temperature $T_Q < T_{c\rightarrow\alpha}$, there are two possible pathways back to the equilibrium L_c phase[55]. If $T_Q < T_{\beta\rightarrow\alpha}$ (~30°C), the gel-to-liquid-crystalline transition, the system will rapidly transition to the L_β phase, which will subsequently become metastable until returning to L_c. However, if $T_{\beta\rightarrow\alpha} < T_Q < T_{c\rightarrow\alpha}$, the L_α phase will become metastable and directly transition to the L_c phase. This direct transition in the aforementioned range of temperatures will be the focus of Section 3.1.

1.5 Research questions and outline

The research questions I sought to answer in this work are:

a. What is the physical mechanism responsible for producing the long-lived metastability displayed by DLPE?
b. Can IDPAs and their self-assembly serve as a platform on which to study the interactions between IDPs?

I will briefly outline the contents of Chapter 3 as an overview of the way I addressed these questions.

Section 3.1 begins with a structural and temporal characterization of the metastability (Section 3.1.1). Next, the properties of the metastability are extensively studied by varying system parameters, measuring the thermodynamic process and applying external mechanical stimuli (Section 3.1.2). I present a rescaling of the metastability and address the issue of reproducibility (Section 3.1.3), as well as a microscopic structural characterization of the lipid bilayer (Section 3.1.4). Finally, I conclude with a detailed theoretical model to describe the underlying mechanism responsible for the non-classical metastability (Section 3.1.5).

In Section 3.2, I will present a comprehensive investigation of new IDPAs. It will include chemical and biophysical characterizations (Sections 3.2.1 and 3.2.2), a pH-dependent phase-transition analysis (Section 3.2.3), as well as propose a model to account for the observed phase-transition (Section 3.2.4). Finally, I will show how small variations to the IDP sequence, predicted using a simple interaction analysis tool, can lead to significant changes to inter-aggregate interactions (Section 3.2.5).

Chapter 2 Methods

2.1 X-ray scattering

X-ray scattering is one of the most common structure-determination techniques, partly due to its ability to probe a wide-range of length scales, which are often found in biological systems. Its small wavelength, comparable with the atomic scale (~Å), enables us to gather information on structures spanning from hundreds of nanometers, such as lipid vesicles and viruses, down to the sub-nanometer scale, as in protein crystallography. For further reading on the subject of X-ray scattering, I highly recommend the book "Elements of Modern X-ray Physics", second edition[62].

In X-ray scattering, highly energetic photons weakly interact with the electrons of the sample, and scatter onto a 2D detector. The scattering amplitude of an object, also known as the form factor, is given by

$$f(\mathbf{q}) = \int \rho(\mathbf{r}) e^{i\mathbf{q}\cdot\mathbf{r}} d\mathbf{r}\,, \tag{2}$$

where $\mathbf{q}$ is the momentum transfer vector, and $\rho(\mathbf{r})$ is the electron number-density. If a crystal is considered, then the scattering amplitude is given by

$$F(\mathbf{q}) = \sum_j f_j(\mathbf{q}) e^{i\mathbf{q}\cdot\mathbf{r_j}} \sum_n e^{i\mathbf{q}\cdot\mathbf{R}_n}\,, \tag{3}$$

where the first sum is sometimes referred to as the unit cell structure factor, and the second summation, called the lattice sum, is over the lattice sites found at $\mathbf{R}_n$. Finally, the intensity, which is the measurable quantity in the experiment, is given by

$$I(\mathbf{q}) = F(\mathbf{q}) F^*(\mathbf{q})\,. \tag{4}$$

When discussing scattering from a crystal, which is periodic in space, it is important to mention the condition for constructive interference of waves scattered with a scattering angle 2θ, from a crystal with a square lattice constant d. This condition is known as Bragg's law,

$$2d\sin(\theta) = n\lambda\,, \tag{5}$$

where n is an integer, and λ is the wavelength of radiation.

Scattering experiments in this work were conducted in one of two setups: Small or Wide Angle X-ray Scattering, SAXS and WAXS respectively. SAXS provides low-resolution information (large wavelength; $qR \ll 1$) on the large length scales of the scattering object. For instance, the famous Guinier approximation, used to calculate the radius of gyration of an object, is

performed on the scattering intensity at small scattering angles. WAXS, on the other hand, provides information on the correlations at smaller length scales (small wavelength; $qR \gg 1$), for instance molecular/atomic packing of crystals or differentiating between folded/unfolded states of polymers (Kratky analysis).

2.1.1 Solution X-ray scattering

Unlike conventional crystallography, nano-scale structural correlations can be measured in solution with X-ray scattering. Such solution X-ray scattering (SXS) experiments are used for investigating samples in various medias (e.g. an aqueous solution) that may affect their intermolecular interactions and their resulting structure. SXS is highly suited for studying self-assembling systems that contain correlations in the length scales mentioned earlier.

SXS experiments are bulk measurements, i.e. the scattering experiment measures a large volume containing many objects. The structure of these objects, as in the case of lipids, can have spherical symmetry (uni and multi-lamellar vesicles), and others a specific orientation (3D crystalline structures), yet these structures are much smaller than the scattering volume. Hence, the scattering volume contains many of these structures, and because they are randomly orientated in solution, the resulting scattering intensity depends only on the scattering angle or $|\mathbf{q}| = \mathrm{q}$. This orientational averaging, also known as powder averaging, results in a scattering intensity of the form[62]

$$I(\mathrm{q}) = \langle I(\mathbf{q})\rangle_{orien.\ av.} = \left| \int \rho(\mathbf{r}) \langle e^{i\mathbf{q}\cdot\mathbf{r}} \rangle_{orien.\ av.}\, d\mathbf{r} \right|^2 = \left| \int \rho(\mathbf{r}) \frac{\sin(\mathrm{qr})}{\mathrm{qr}}\, d\mathbf{r} \right|^2 . \quad (6)$$

Therefore, such scattering will be collected on the X-ray detector in the form of rings, centered around the direct beam. One should then perform an azimuthal integration of the intensity, which results in a 1D scattering profile; the scattering intensity as a function of the momentum transfer amplitude – $I(\mathrm{q})$ (Figure 7).

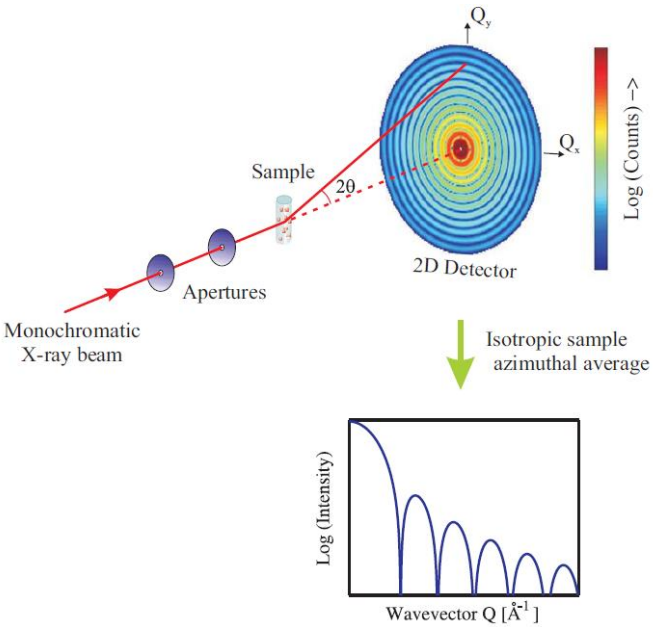

Figure 7. An illustration of an X-ray scattering experiment. A monochromatic beam of X-rays, collimated using apertures, is scattered off the sample to produce the 2D scattering pattern seen on the detector. The observed rings in the pattern are a consequence of the orientational randomness of the many objects in the sample. The 2D image is then azimuthally integrated to produce the radial profile of the scattering intensity. Figure adapted from Ref. 62. Note: momentum transfer denoted by Q in the adapted figure is equivalent to *q* in the text.

2.1.2 Practical methodologies in X-ray scattering

An important topic on its own deals with good practices that are necessary to produce high-quality X-ray scattering data. While I will mention just a few key ones, there is an exhaustive review on all the steps that should be taken, and how to perform them[63].

The first is data collection, the importance of which cannot be stressed enough. Once high-quality data have been collected for a particular sample, it can forever be subjected to a variety of analyses. This entails matching the right vessel to hold the sample with the requirements of the system and task at hand, choosing the appropriate system setup to probe the relevant length scales (SAXS/WAXS), and collecting enough data to establish good signal-to-noise.

The second step is data correction. There are many types of corrections but the most significant ones are corrections for dark current/natural background, normalization by transmission intensity and background subtraction.

Dark current (e.g. leak currents) and natural background (e.g. cosmic radiation) are independent signals detected by the detector in the absence of an X-ray beam. The correction for the two is usually performed by subtracting a constant from the pixel values.

Normalization by transmission accounts for the difference in absorbance of different media. This procedure is necessary to perform to achieve good background subtraction, which will be discussed next. Usually the normalization is performed by using the measured flux after the sample.

Background subtraction is key for quantitative analyses that depend on the most minute features of the scattering profile. The accuracy of measuring the scattering intensity originating from the studied system, especially at small scattering angles (e.g. Guinier analysis), can heavily influence our ability to report on comparable values and come to meaningful conclusions. Background subtraction is performed after adequately collecting data of the sample and its background (usually the surrounding solution and sample holding vessel), and performing the previous corrections.

Formulating these corrections together, the intensity can be expressed as

$$I(\mathrm{q})_{corrected} = \frac{I_s - I_{dc}}{n_s} - \frac{I_{bg} - I_{dc}}{n_{bg}}, \quad (7)$$

where I_s is the sample data, I_{bg} the background data, I_{dc} the dark current and natural background, and n_s (n_{bg}) the transmission measurement of the sample (background) taken with the pin-diode.

The third step is data analysis, and this obviously relies on high-quality data and appropriate and accurate data correction. As often heard, the 'no-free-lunch' theorem means different biophysical characterizations will call upon different analyses to extract the relevant physical parameters. Many times, older data-linearizing techniques such as Guinier, Kratky and Porod plots will be useful, however they can suffer from high sensitivity to noise and inaccurate data collection/correction. A more appropriate fitting methodology, thanks to modern computing power and automatic optimization, is performed on the full q-range data (as discussed in the next section, and demonstrated in Sections 3.1.4 and 3.2.3.2.3).

2.1.3 Form factor and structure factor modeling

2.1.3.1 Phospholipids

In the case of multi-lamellar lipid structures, the scattering objects are the bilayers, stacked together to form a 1D periodic lattice. There are numerous ways to model the electron density of the bilayer, including a common model in which N gaussian functions are summed, modeling the different chemical groups comprising the lipid molecule[64,65]. The number of functions used points to the desired level of detail needed from the model. For instance, the minimum number of functions required to generally describe a centro-symmetric bilayer is three. Figure 8 shows

a representation of such a model, with one gaussian located at the center, describing the tails of the opposing lipids, while two other functions on either side represent the headgroups (the structure of a bilayer can be seen in Figure 4 for reference).

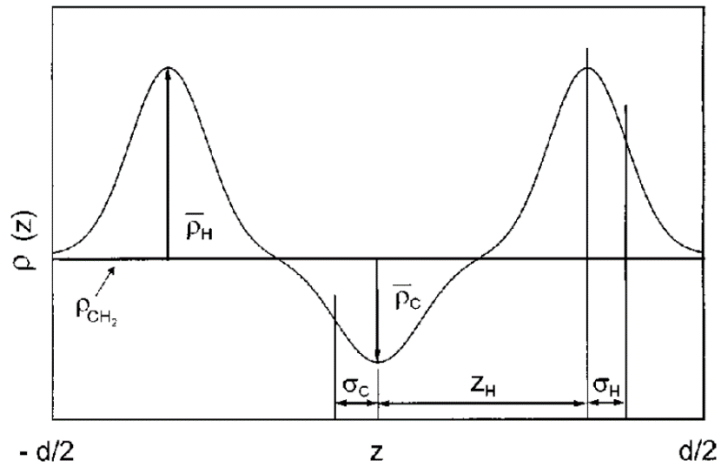

Figure 8. Electron density profile modelled using two identical Gaussians for the headgroups and one for the adjacent hydrocarbon chains. Adapted from Ref. 65.

The scattering amplitude can then be conveniently calculated analytically using Eq. (2). The summation over the lattice is then corrected for the change in Bragg peak intensity and shape caused by the thermal motion of the membranes in solution[66]. The function describing the correction is commonly known as the structure factor, $S(\mathrm{q})$. The scattering intensity now takes the form:

$$I(\mathrm{q}) = |F(\mathrm{q})|^2 \, S(\mathrm{q}) \tag{8}$$

The goal of scattering experiments is to determine the structure of the investigated sample. However, since only the intensity is measured in scattering experiments, methods are used to reconstruct the density function in real space. In the case of lipid structures, and multi-lamellar vesicles specifically, this can be achieved by means of a discrete Fourier synthesis, which samples the continuous form factor at q-values pertaining to lamellar correlation peaks. However, reconstruction is also possible using a continuous method, which takes advantage of the full q-range scattering line shape. I made use of such a continuous fitting method, which utilizes a modified Caillé theory structure factor in combination with a gaussian model representing the electron density profile[65,67,68] (Section 3.1.4)

2.1.3.2 Intrinsically disordered peptide amphiphiles (IDPAs)

For modeling the electron density and corresponding form factor of the micelles I used the analysis software X+[69]. The software performs a form factor fit using a prescribed geometrical model for the electron density. Specifically, I chose a Smooth Sphere model, effectively using

hyperbolic tangent functions to model two smoothly varying layers, the hydrophobic core and peptide shell. In the modeling process you are required to input the values of the center of the functions, their amplitude and slope. In addition, there is a possibility to add variance to the parameters, representing the polydispersity. One drawback of the software, which I encountered during my efforts to fit the data, is the lack of automatic optimization. The software has limited ongoing support, although the researchers at the Raviv Lab at HUJI are more than welcoming and helpful.

Once the form factor satisfactorily fits the data, one can output the fit and the corresponding electron density profile. The results of my fits are shown in Section 3.2.3.2.3.

2.1.4 Sample preparation and measurement protocol

2.1.4.1 Phospholipids

The saturated lipids 1,2-dilauroyl-sn-glycero-3-phosphoethanolamine (DLPE), 1,2-dilauroyl-sn-glycero-3-phosphoglycerol (DLPG), 1,2-dimyristoyl-sn-glycero-3-phosphoglycerol (DMPG), 1,2-dipalmitoyl-sn-glycero-3-phosphoglycerol (DPPG), 1,2-distearoyl-sn-glycero-3-phosphoglycerol (DSPG) and 1,2-dilauroyl-sn-glycero-3-phosphocholine (DLPC) were purchased from Avanti Polar Lipids Inc. The lipids were dissolved in chloroform (DLPE) and chloroform:methanol 5:1 (other lipids) separately, then mixed together to achieve desired stoichiometry. Total lipid concentration was 30 mg ml^{-1} per sample. The solution was evaporated overnight in a fume hood, and re-fluidized using a buffer at 6.7 pH containing 20 mM 2-(N-morpholino)ethanesulfonic acid (MES), 1mM $MgCl_2$ and 13mM NaOH (from titration). NaCl was added to achieve desired monovalent salt concentration. Samples were then placed in an incubator at 37°C for 3 hours, and homogenized using a vortexer every 25 minutes. Samples were then placed in quartz capillaries, containing about 100 μl, and centrifuged for 5 minutes at 3000 RPM, to create a pellet of lipids (Figure 9).

Figure 9. Photo of a pellet formed at the bottom of the capillary by centrifuging the lipid dispersion. Above the pellet is the phase-separated solution.

Samples at 30 mg ml^{-1} lipid concentration were measured in 1.5 mm diameter sealed quartz capillaries. Measurements were performed using an in-house solution X-ray scattering system, with a GeniX (Xenocs) low divergence Cu K_α radiation source (wavelength of 1.54 Å) and a scatter-less slits setup[70]. Two dimensional scattering data with a q range of 0.06–2 $Å^{-1}$ at a sample-to-detector distance of about 230 mm were collected on a Pilatus 300K detector (Dectris), and radially integrated using MATLAB (MathWorks) based procedures (SAXSi). Background scattering data was collected from buffer solution alone. The background-subtracted scattering correlation peaks were fitted using a Gaussian with a linearly sloped baseline. For each sample, time-resolved correlation peaks position, intensity and width were extracted.

2.1.4.2 IDPAs and peptide

The following procedure was adopted during this project to counter the acidic conditions of the synthesized IDPAs and peptides, with the intention of controlling sample pH. This is a common problem encountered during peptide synthesis and purification and should always be taken into consideration, as it can heavily misguide research if ignored! The challenges faced during amphiphile production are discussed further in Section 4.2.3.

The IDPA or peptide powder (supplied after synthesis and purification) was first fluidized in purified water (Milli-Q) at twice the desired concentration. The solution was then titrated with NaOH to a pH where the solution became more homogenous (preferably a pH where the IDPAs are soluble in water). Titration was monitored using a pH probe small enough to fit into an Eppendorf (Sentek P13 pH Electrode). Following titration, 50 µl of the solution was combined with 50 µl of 2X buffer of choice, to achieve a pH ‘close’ to the desired one (since we are

combining two solutions, the pH will not be exactly set by the buffer alone, and it will generally deviate up to half a pH). The 2X buffers Acetic Acid (pH 3-4.5), MES pH (5-6.5) and MOPS (pH 7-7.5), were prepared at 200 mM, so as to achieve a final buffer molarity of 100 mM after mixing with IDPA or peptide solution 1:1.

For this project samples were measured at two synchrotron facilities, Diamond Light Source in the UK and Advanced Light Source (ALS), Berkley, USA. For samples that were miscible (above the transition pH, usually above 6) the B21 beamline (Diamond) and SIBYLS 12.3.1 beamline (ALS) were used. Both have automatic robot samplers that are very convenient for soluble samples. In the case of SIBYLS beamline, I used a mail-in session. For phase-separating samples that display a sediment (below the transition pH, generally pH 3-5.5) beamline I22 (Diamond) was used.

2.2 Cryogenic transmission electron microscopy (Cryo-TEM)

One of the most prominent experimental techniques used for the study of soft nanostructures in liquids, Cryo-TEM is based on the ultra-fast vitrification of the liquid sample to take a 'snapshot' of the hydrated state of the material. Unlike the bulk and time averaged information provided by X-ray scattering, this is a direct-imaging method that can provide aggregate-specific information. This makes Cryo-TEM exceptionally well at complimenting indirect characterization methods.

2.2.1 Sample preparation and measurement protocol

2.2.1.1 Phospholipids

Measurements performed by Prof. Yeshayahu Talmon's laboratory, Department of Chemical Engineering, Technion.

Cryo-TEM specimens were prepared in a controlled environment vitrification system (CEVS), to preserve the native structure of the system at the desired temperature[71]. A drop of the solution was placed on a carbon-coated perforated polymer film, supported on a 200 mesh TEM copper grid, mounted on tweezers. Thin liquid films (preferably less than 300 nm thick) were formed by blotting excess solution with a metal strip wrapped with a filter paper. The specimen was then plunged into liquid ethane at its freezing point (-183°C). Cryo-TEM imaging was performed with an FEI Tecnai T12 G^2 electron microscope, operated at an accelerating voltage of 120 kV. The cryo-specimens were transferred under controlled conditions into a Gatan 626DH cryo-holder, using its "transfer station". After the specimens were equilibrated in the TEM below -175°C, they were imaged in the low-dose imaging mode to minimize electron-

beam radiation-damage. The images were digitally recorded by a Gatan US1000 high-resolution cooled CCD camera, using the Gatan DigitalMicrograph software.

2.2.1.2 IDPAs

Measurements performed by Prof. Dganit Danino's laboratory, Department of Biotechnology & Food Engineering, Technion.

Cryo-TEM specimen preparation was performed by applying a 6 µl drop of the studied solution to a perforated carbon film supported on a 200-mesh TEM copper grid, thinning (blotting) and removing excess solution, and then the sample was vitrified in liquid ethane at its freezing point (-183°C). The procedure was carried out at controlled temperature (25°C) and at water saturation. The vitrified specimens were stored under liquid nitrogen (-196°C) until examination. The samples were then examined using a Tecnai T12 G2 (FEI, The Netherlands) TEM operated at an accelerating voltage of 120kV, keeping specimen temperature below -170°C during transfer and observation. Images were digitally recorded on a Gatan Ultrascan 1000 cooled CCD camera by using the Gatan Digital Micrograph software package. Images were recorded using methodologies we developed[72] under low-electron-dose conditions to minimize electron beam radiation damage.

2.3 Differential scanning calorimetry (DSC)

DSC is a thermoanalytical technique in which the difference in the amount of heat required to increase the temperature of a sample and reference is measured as a function of temperature. It is one of the main experimental methods for measuring the heat capacity of a material, as well as detecting exothermic/endothermic phase-transitions and extracting their associated enthalpies of transition.

2.3.1 Sample preparation and measurement protocol

Measurements performed by Dr. Irina Portnaya from Prof. Dganit Danino's laboratory, Department of Biotechnology & Food Engineering, Technion.

DSC experiments were performed using a VP-DSC micro calorimeter (MicroCal Inc., Northampton, MA). Calorimetric data analysis was done with the Origin 7.0 software. Degassed systems of pure DLPE and 90:10 DLPE:DLPG (mole %) at a total concentration of 30 mg ml^{-1} were placed in the sample cell (0.5 ml), and MES buffer (20 mM MES + 130 mM NaCl at pH 6.7) in the reference cell. DSC thermograms were recorded during multiple heating–cooling cycles at various scan rates and different pre- and post-scan periods. First, each sample was heated from 25°C to 60°C with at a rate of 90°C $hour^{-1}$ and 15 minute pre- and 3 hour post-

scan periods. Then the sample was cooled from 60°C to 37°C with a scan rate of 90°C hour^{-1}, and identical 15 minute pre- and post-scan periods. The additional scans were carried out at a very slow rate of 0.1°C hour^{-1} for heating and 0.43°C hour^{-1} for cooling, with 1 minute pre- and post-scan periods. In this manner, the DSC was used in a quasi-isothermal mode, where the metastability was monitored until it ended in an exothermic transition to the crystalline state. Additionally, on the same instrument DSC measurements of 10-fold diluted samples (3 mg ml^{-1}) of pure DLPE, and 97:3; 95:5; 92:8; 90:10, 85:15 DLPE:DLPG (mole %) were performed, to measure the transition temperature and transition enthalpy. The buffer composition was the same. DSC thermograms were recorded during double heating–cooling cycles (between 25°C and 60°C) with a scan rate of 90°C hour^{-1}, and identical 15 min pre- and post-scan periods.

2.4 Turbidity

Turbidity measurements use the absorbance of light to determine the translucency of a solution, which reports on the presence of structures comparable to the light's wavelength or larger. This method can be used to detect a phase-transition if it involves a change in particle structure and inter-particle aggregations.

2.4.1 Sample preparation and measurement protocol

All measurements were recorded on a TECAN Infinite M200Pro device. The amphiphiles were treated and prepared in the same manner as previously described (Section 2.1.4.2) to achieve a final concentration of 5 mg ml^{-1}. 100 µL of each solution was loaded onto a 96 wells plate. The absorbance at 600 nm was scanned for each well.

2.5 Circular Dichroism (CD)

Circular Dichroism (CD) is an absorption spectroscopy method based on the differential absorption of left and right circularly polarized light, widely used for high level structure determination of proteins. Secondary structures of proteins can be analyzed using the far-UV (190-250 nm) region of light. The ordered α-helices, β-sheets, β-turn, and random coil conformations all have characteristic spectra. CD measurement data can be decomposed into a combination of these spectra, reporting on the relative presence of each. It should be noted that this technique cannot be used to determine where these structures are present, only to what degree they are.

I used CD to determine the disordered state of the conjugated peptides (IDPAs) and the free peptides by themselves[73] (Section 3.2.2.1).

2.5.1 Sample preparation and measurement protocol

CD measurements were performed using a commercial CD spectrometer (Applied Photophysics Chirascan). Both IDPAs, 2x12 and 4x7, as well as the unconjugated IDP were placed in a glass cuvette with a 10 mm path length. The IDPAs and peptide were mixed with a phosphate buffer to achieve a concentration of 0.05 and 0.1 mg ml^{-1}, respectively. Measurements were performed using phosphate buffer since the buffers used for the X-ray scattering experiments (mainly MOPS and MES) have high absorbance in the relevant CD wavelengths. The 190-260 nm wavelength range was probed in 1 nm steps, with 0.5 secs at each point. Three measurements were performed for each and averaged.

Chapter 3 Results

The body of work presented here consists of two major projects. The first focuses on a metastable liquid-crystalline to stable crystalline phase-transition in phospholipid membranes. The metastability is studied using various experimental techniques to characterize its dynamics and dependence on various system parameters, e.g., temperature, composition, heat cycles and solution salt concentration. In addition, a theoretical model is proposed to describe the underlying physical mechanism responsible for the delay in transition (work done in collaboration with Prof. Haim Diamant – School of Chemistry, Tel Aviv University). The results presented in Section 3.1 are based on two publications[74,75]:

- Guy Jacoby, Keren Cohen, Kobi Barkan, Yeshayahu Talmon, Dan Peer & Roy Beck. Metastability in lipid based particles exhibits temporally deterministic and controllable behavior. *Sci. Rep.* **5**, 9481 (2015).
- Guy Jacoby, Irina Portnaya, Dganit Danino, Haim Diamant & Roy Beck. Delayed nucleation in lipid particles. *Soft Matter* **16**, 247–255 (2020).

Since much of the work on both projects was done in collaborations, the following text includes many references in the plural form ‘we’, however, in all cases the majority of the work was done by me, unless explicitly mentioned otherwise (Chapter 2).

3.1 Metastability of phospholipid membranes

3.1.1 Time-resolved characterization of the metastability (WAXS, Cryo-TEM)

The metastable L_α to L_c phase-transition was recorded by time-resolved WAXS (Figure 10). In the experiments, the X-ray beam illuminating the sample had a cross sectional area of approximately 0.64 mm^2, which produced a bulk-averaged scattering signal. The scattering from a sample that has not been pre-heated was first recorded at T_Q ($T_{\beta\rightarrow\alpha} < T_Q < T_{c\rightarrow\alpha}$) as a reference point to the initial low-energy state of the system. The scattering pattern of this initial state pertains to a 3D crystal with an orthorhombic unit cell, with parameters a = 9.5 Å, b = 7.7 Å, and c = 45.6 Å, in close agreement with previous crystal indexations of fully hydrated DLPE[55,76] (Figure 11). The largest dimension corresponds to the lamellar repeating distance, and the shorter ones to the in-plane ordering of the lipids. Notably, the (002) reflection of the lamellar correlation peak is absent (Section 3.1.4).

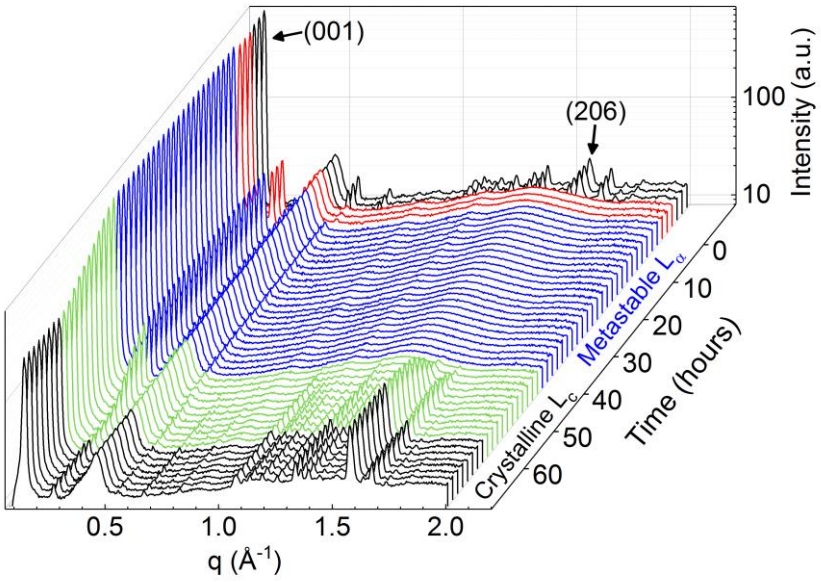

Figure 10. An example of time-resolved scattering spectra of lipid system containing 93:7 DLPE:DSPG (mole %). Initially, at T_Q = 37°C (black spectra before time 0), the crystalline phase is indicated by the presence of wide-angle correlation peaks. When heated to 60°C (red spectra) these peaks disappear with the loss of in-plane order. After cooling back to T_Q (blue spectra), the L_α phase remains metastable for 47 hours, and then phase-transitions (green spectra) back into the crystalline phase (black spectra). Figure taken from Ref. 75.

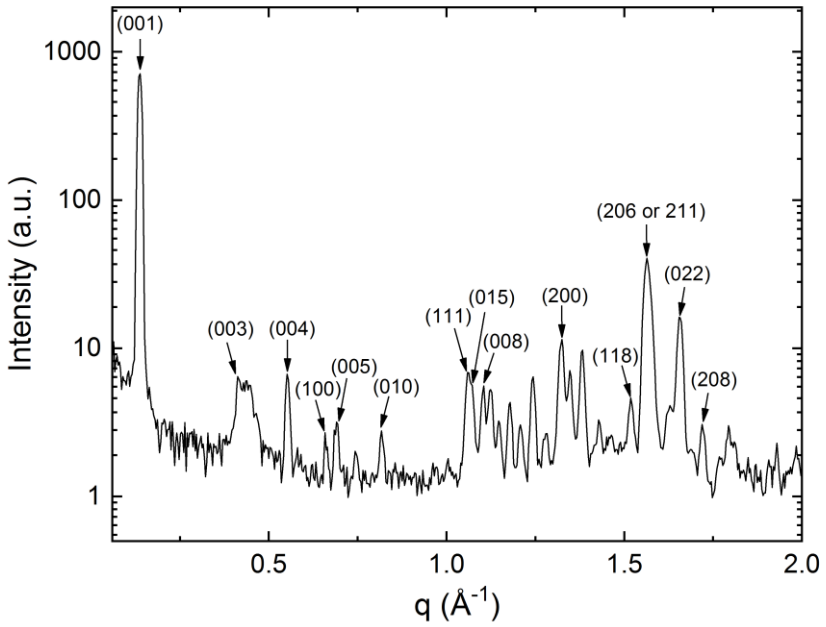

Figure 11. Crystal structure indexation of fully hydrated DLPE at 37°C prior to heating. Correlation peaks indexed as an orthorhombic lattice with parameters a = 9.5 Å, b = 7.7 Å and c = 45.6 Å. Figure taken from Ref. 74.

The scattering from the sample was then recorded after heating to 60°C (above $T_{c\rightarrow\alpha}$), where the lipid membranes transitioned to the smectic L_α phase, i.e., a lamellar structure with in-plane liquid-like disorder. This is indicated by the disappearance of the wide-angle peaks in the scattering profile. The phase change is accompanied by a change in morphology of the lipid particles, from faceted crystals (Figure 12) to curved multi-lamellar vesicles (MLVs) (Figure 13).

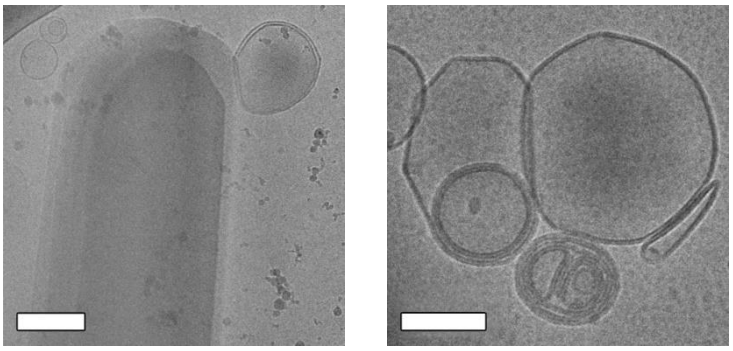

Figure 12. Cryo-TEM images of specimens vitrified at 37°C prior to heat treatment showing a large DLPE crystal structure along with uni- and multi-lamellar vesicles (left), and vesicles with sharp facets (right). Scale bars represent 200 and 100 nm, left and right, respectively. Figures taken from Ref. 74.

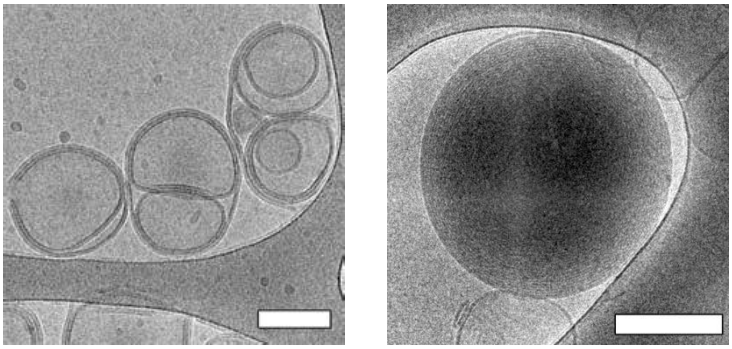

Figure 13. Cryo-TEM images of specimens vitrified from 60°C showing curved geometries (left) and a large MLV (right). Scale bars represent 100 and 200 nm, respectively. Left image taken from Ref. 74.

After three hours at 60°C, the sample was quenched (at a rate of 2.5°C min^{-1}) back to T_Q and measured every hour until it finished transitioning back to L_c. The metastability ends in a collective phase-transition back to L_c with identical in-plane spatial correlations to the initial L_c phase (Figure 10). Cryo-TEM confirmed recrystallization of the hydrocarbon chains through the appearance of straight facets on otherwise round vesicles and the fusion of adjacent bilayers (Figure 14).

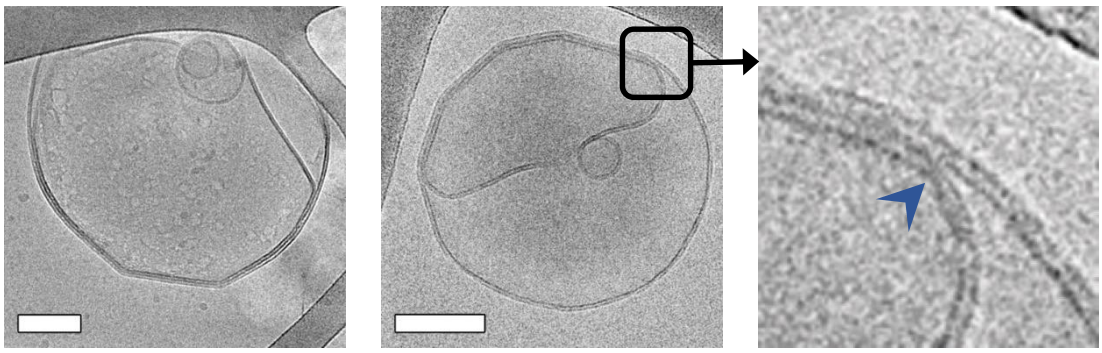

Figure 14. Cryo-TEM images of specimens vitrified from 37°C, 44 hours after cooling (left), 37°C, three days after cooling, showing multiple facets on a vesicle (middle). Detail of the previous micrograph showing the fusion of two membranes, accompanied by the removal of water from between them (right). Blue arrowhead indicates the fusion point of the two membranes, separating the crystalline phase (straight facets to the left) from the liquid-crystalline phase (disjoined, curved leaflets to the right). Scale bars represent 100 nm. Images taken from Ref. 74.

There are several prominent features in the evolution of the scattering spectrum after cooling back to T_Q. The first is the extended period in which the L_α phase remains metastable, which we denote as the delay time τ (Figure 15). The second is the time the system spends transitioning between phases, denoted as the transition period τ^*, which is by and large an order of magnitude shorter than τ. The third notable feature occurring in most of the experiments

accounted for in this work is a substantial change in the lamellar scattering intensity during the transition period. The intensity remains constant during the delay time, however it decreases, up to an order of magnitude, during the transition period. This indicates a decrease in the average number of lamellae per particle during the transition. This implies that the phase-transition is accompanied by a macro-scale structural change of the particles.

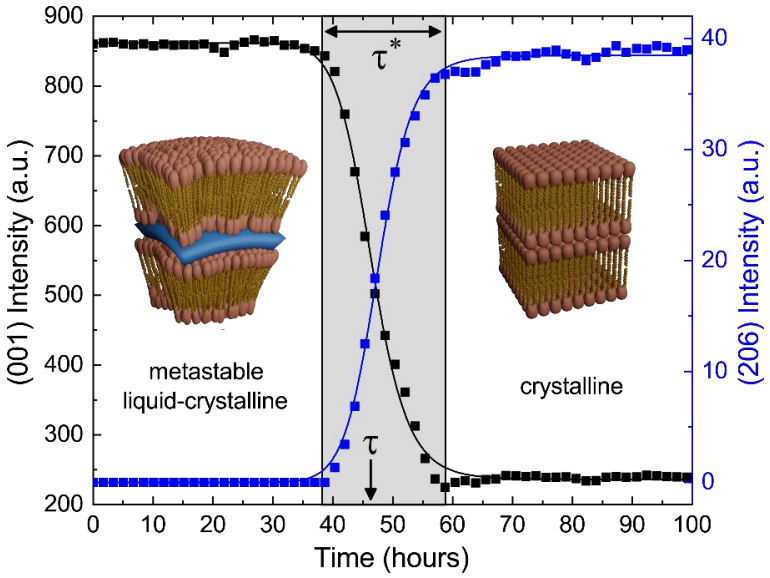

Figure 15. Scattering intensity over time of lamellar correlation peak (001) and mixed wide-angle peak (206) used to measure the order parameters and extract the temporal features of the dynamics (delay time – τ, transition period – τ^*). Inset: Schematic illustration of the lipid conformation in both the liquid-crystalline (L_α) and the crystalline (L_c) phases. Figure taken from Ref. 75.

According to the classical nucleation theory, a single timescale should be observed, namely, that associated with the rate of nucleation. However, given that WAXS produces bulk-averaged signals, one can immediately notice that the dynamics presented in the X-ray spectra do not readily conform to the classical picture of a single stochastic process culminating in a phase-transition. Instead of a gradual increase in crystalline scattering, we observe two distinct timescales, τ and τ^*, which are orders of magnitude larger than the melting transition times, with no detectable scattering at wide angles prior to the transition. This implies a collective bulk transition rather than stochastic events of crystallization within the macroscopic illuminated area.

The timescales τ and τ^* are extracted from the time-dependent correlation peak intensities, which are a direct measurement of the order parameters. Specifically, we fit a sigmoid function to the time-dependent intensity of the lamellar correlation peak (001) and to a mixed correlation peak in the wide angles (206) (Figure 15), to measure the out- and in-plane order parameters respectively.

3.1.1.1 Quenching temperature

The lifetime of the metastable phase depends on the strength of the thermodynamic force driving the transition. Close to the transition temperature the energy barrier that the system must overcome is high, which results in a slow rate of nucleation. As the temperature is lowered, the barrier becomes smaller and the rate increases. This is demonstrated here by the increasing persistence of the metastable L_α phase, closer to $T_{c\to\alpha}$. Figure 16 shows an exponential increase in the average delay time as a function of the quenching temperature, T_Q, for samples of pure DLPE. Remarkably, for most quenching temperatures the spread of experimental results is very small, further supporting the claim that τ is an intrinsic property of the system's dynamics set by its macroscopic parameters. However, due to larger fluctuations closer to the critical temperature ($T_{c\to\alpha}$) we notice a large spread of τ at T_Q = 41°C. There, two samples did not transition within the duration of the experiment (800 hours). In addition, at T_Q = 31°C the L_α phase rapidly transitioned to L_β, which then became metastable. Evidently, the delay time for the L_α phase at T_Q = 32°C is shorter than at T_Q = 31°C for the L_β gel phase, as the liquid phase is expected to be more labile[56].

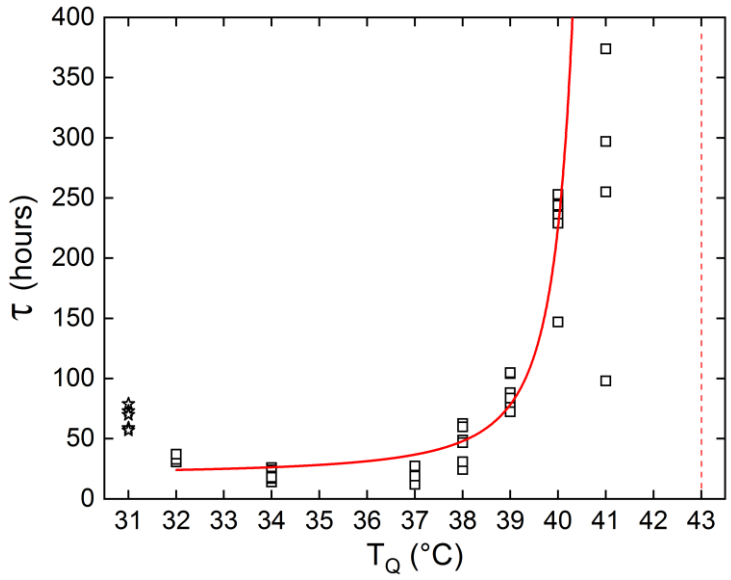

Figure 16. Delay time as a function of quenching temperature for pure DLPE. Empty squares represent measurements of individual capillaries at each quenching temperature. Solid red curve is the fit using Eq. (25) (Section 3.1.5.4), excluding the measurements at T_Q = 31°C (empty stars represent the $L_\beta \rightarrow L_c$ transition) and T_Q = 41°C due to the high variance caused by fluctuations. Red vertical dashed line indicates the estimated $T_{c\to\alpha}$ transition temperature. Figure taken from Ref. 75.

3.1.2 Manipulating the metastability

To understand the origins of the mechanism responsible for the delay in crystallization, we measured the dependence of the delay time on several system parameters, such as the system's composition, solution salt concentration, and successive phase-transition cycles.

3.1.2.1 Secondary phospholipid

In previous studies, the metastability was examined in samples of pure DLPE[55,59,76]. However, we found that the addition of a secondary phospholipid not only preserves the metastable phase, but also extends its lifetime (Figure 17). Moreover, the delay time is sensitive to changes in the hydrocarbon chain length and headgroup. Phosphoglycerols (PGs) were chosen as a secondary charged lipid due to the stabilizing effect they have on PE bilayers[77]. Specifically, DLPG was previously used along with DLPE as the building blocks for a drug delivery system[78–80]. PGs with 12 (DLPG), 14 (DMPG), 16 (DPPG) or 18 (DSPG) carbons in their saturated hydrocarbon chains were chosen as chain length variants. In addition, the zwitterionic dilauroyl-phosphocholine (DLPC) was chosen as a headgroup variant. The delay time seems to increase as a function of chain length for the PGs, and it is greatly increased when the PG headgroup is swapped with a PC.

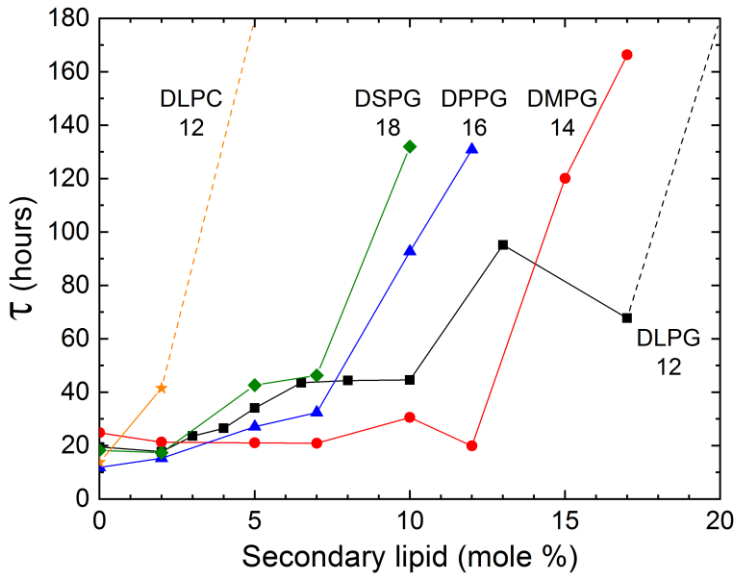

Figure 17. Delay time (τ) as a function of the molar fraction (mole %) of the secondary lipid, i.e., (100 - DLPE) (mole %). The labels indicate the abbreviated name of the lipid and the number of carbon atoms in its hydrocarbon chains. An increase in chain length results in an increase in delay time at a lower fraction. Dashed lines represent the minimal delay time for samples that did not transition within 180 hours. Samples with higher concentrations of DPPG and DSPG were measured but omitted from the results due to an alteration of the final crystalline form. Figure taken from Ref. 75.

3.1.2.2 The role of electrostatics and ions

The stabilization of membranous lipid systems comes from an interplay between several types of interactions. Measurements of the zeta-potential (the electrical potential at the double layer, used to estimate the surface charge) suggests the lipid dispersions are charge (Figure 18). However, the out-of-plane distance between the lamellae is not solely stabilized by electrostatic repulsion (Figure 19). Instead short-ranged van der Waals attraction between membranes are balanced by hydration repulsion[81], and long-range membrane undulations[82]. The former is pronounced for membranes separated by a distance of 30 Å or less, as is the case with the water layer thicknesses found between hydrated DLPE membranes[64,83] (Section 3.1.3). The latter is an entropic repulsion, typical of membranous systems at finite temperatures.

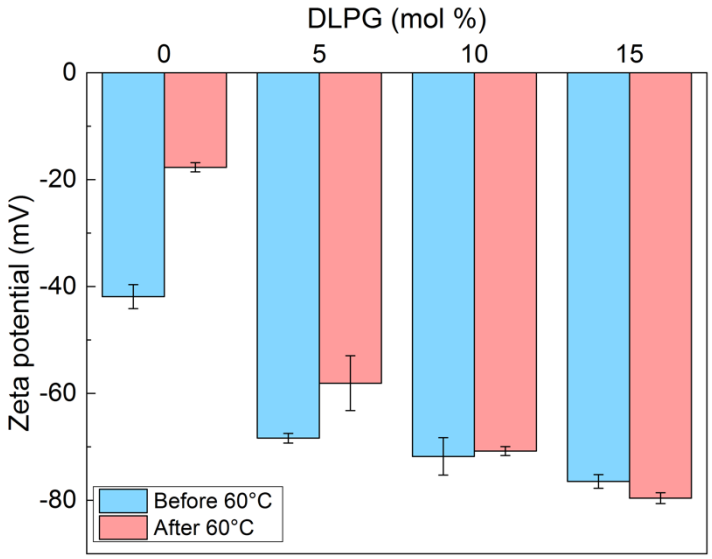

Figure 18. Zeta-potential measurements of mixed sample before and after heating to 60°C. Increasing the charged lipid concentration results in a higher zeta-potential of the lipid particles. Three measurements were performed for each sample. Error bars represent the standard deviation of the measurements. Figure taken from Ref. 74.

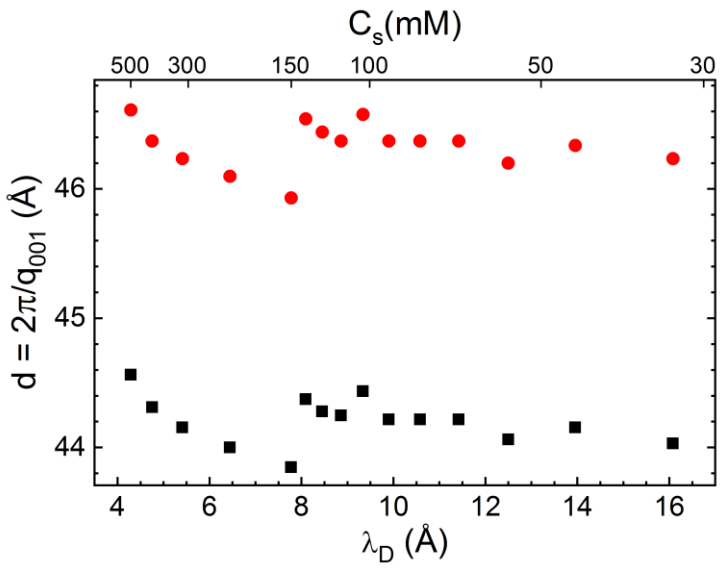

Figure 19. Inter-lamellar spacing vs. the Debye screening length or salt concentration. Increasing salt concentration did not have a noticeable effect on inter-lamellar spacing, both at 37°C (red circles) and at 60°C (black squares). Figure taken from Ref. 74.

Nevertheless, monovalent salt (NaCl) concentrations affect the metastability non-monotonically. We tested the effect of the solution salt concentration on the delay time of samples with different DLPE:DLPG ratios. Changing the average membrane charge density produces two features in the salt dependence: (a) there seems to be a minimum of the delay time at approximately 150 mM, splitting the dependency into two regimes, and (b) the delay time increases with the fraction of DLPG at a given salt concentration.

We propose that these two regimes originate from two different phenomena. At low salt concentrations (<150 mM), the decrease in delay time towards the minimum can be attributed to the decrease in the electrostatic screening length. At 150 mM the electrostatic screening length is comparable to the DLPG headgroup diameter (~8 Å)[84]. Segregation of non-DLPE lipids, which is essential for recovering the homogeneous DLPE crystals, is facilitated by the screening of interacting charged PG headgroups. On the contrary, high salt concentrations (>300 mM) can lead to adsorption of ions on the charged membrane. This can lead to an increase in τ, since ions must evacuate from between the lamellae, yet ion transport across membranes is unfavored. The adsorption of charges can result in an increase in the membrane's bending rigidity, which in turn can strengthen the metastability (Section 3.1.5). The results show that the delay time of samples containing charged headgroups responded to changes in salt concentration, yet no significant dependence was observed in samples containing only DLPE.

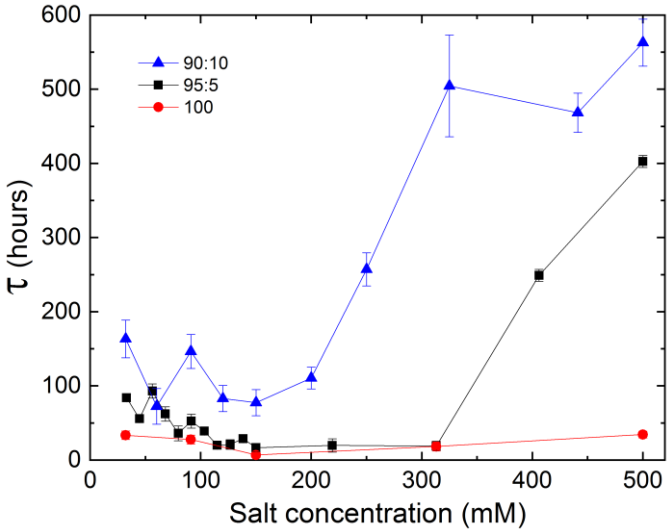

Figure 20. Delay time as a function of monovalent salt concentration, at different DLPE:DLPG ratios (mole %). At low salt concentrations (<150 mM), samples that contain DLPG (black and blue) show an increase in the delay time as salt concentration is decreased. At high salt concentrations (>300 mM) the opposite trend occurs. However, when the sample contains pure DLPE, there is no significant effect of the salt concentration on the delay time. Error bars represent the transition period, τ^*. Figure taken from Ref. 75.

With salinity having a profound effect on τ, we incorporated monensin, a sodium specific ionophore, into the lipid dispersions. The control sample, containing 90:10 DLPE:DLPG (mole %) without monensin, recrystallized after τ = 44.7 hours and τ^* = 9.7 hours. With the addition of monensin, we observed a decrease by up to a factor of three in the delay time (Figure 21).

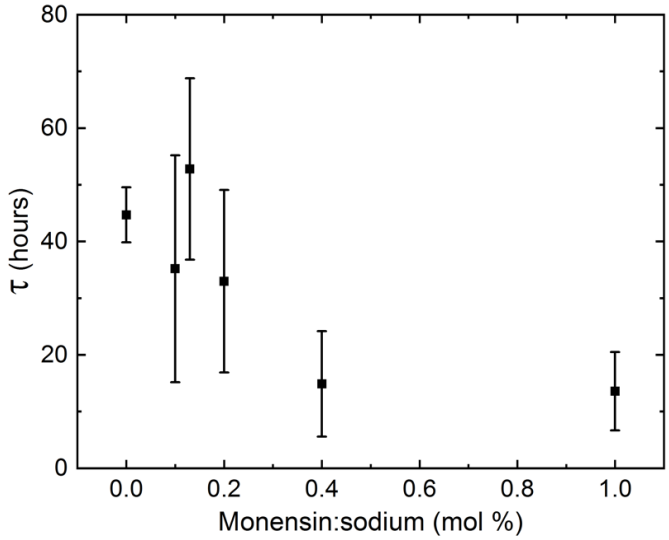

Figure 21. Effect of the monensin ionophore on the delay time. Control sample recrystallized at τ = 44.7 hours. The addition of monensin accelerates recrystallization – sample containing 1 mole % monensin:sodium recrystallized with τ = 13.6 hours. Experiments performed on samples containing 90:10 DLPE:DLPG at 150 mM monovalent salt. Error bars represent the transition period, τ^*. Figure taken from Ref. 74.

3.1.2.3 Thermal cycles

Thermal cycles, above and below the melting transition temperatures, are commonly used to homogenize lipid samples. Apparently, such a treatment has a remarkable effect on the metastable state and can be used to manipulate the delay time. We performed consecutive heating and cooling cycles to monitor successive phase-transition dynamics and observed two distinct features. Successive cycles show a prolongation of the delay time, up to a factor of five in the 5th cycle, and a reduction in the lamellar correlation peak intensity, measured at the metastable state (Figure 22).

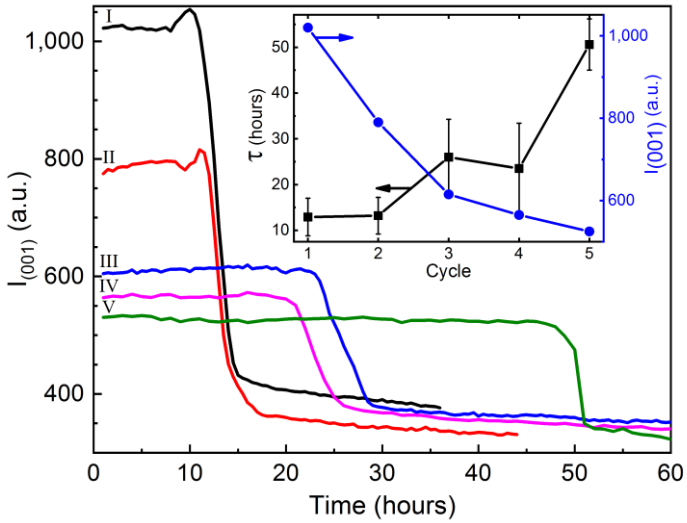

Figure 22. Consecutive heating-cooling cycles lead to a prolongation of the delay time accompanied by a decrease in the metastable lamellar scattering intensity. The curves represent the intensity of lamellar (001) scattering from the moment the temperature is brought back to 37°C after heating. Roman numbers indicate the measurement sequence. Inset shows extracted values of the two effects. Data of 95:5 DLPE:DLPG (mole %). Error bars represent the transition period, τ^*. Figure taken from Ref. 74.

3.1.2.4 Calorimetry

The structural study of the delayed nucleation phenomenon, using time-resolved X-ray scattering, does not directly report on the thermodynamic processes. To address this, calorimetric measurements are commonly used to investigate the thermodynamics of lipid systems, mostly in the form of differential scanning calorimetry (DSC). However, since we are investigating a time-delayed transition at a fixed temperature, we employed DSC in a non-trivial quasi-isothermal manner. After samples were incubated at 60°C for 3 hours, the temperature was lowered to T_Q = 37°C, and the samples were scanned back-and-forth between 36 and 37°C at a very slow rate (0.1°C $hour^{-1}$ on heating, 0.43°C $hour^{-1}$ on cooling).

We compare the quasi-isothermal energy flux measurements performed on a sample of pure DLPE and a sample containing 90:10 DLPE:DLPG (mole %) (Figure 23). The results in both cases show an exothermic signature, as expected for the transition back to the low-energy crystalline phase, with similar timescales to those in our X-ray scattering measurements (Figure 17). The sample with pure DLPE shows a broad and slow change in the excess heat capacity, peaking at 28 hours, while the mixed sample shows a much narrower peak, centered at 55 hours. The corresponding average delay times in the X-ray scattering experiments are 20 and 45 hours, respectively. In addition, a DSC measurement was performed to determine the enthalpy of

transition from the L_c to the L_α phase for a pure sample of DLPE, which yielded $h_c = 11.1$ kcal mole^{-1}.

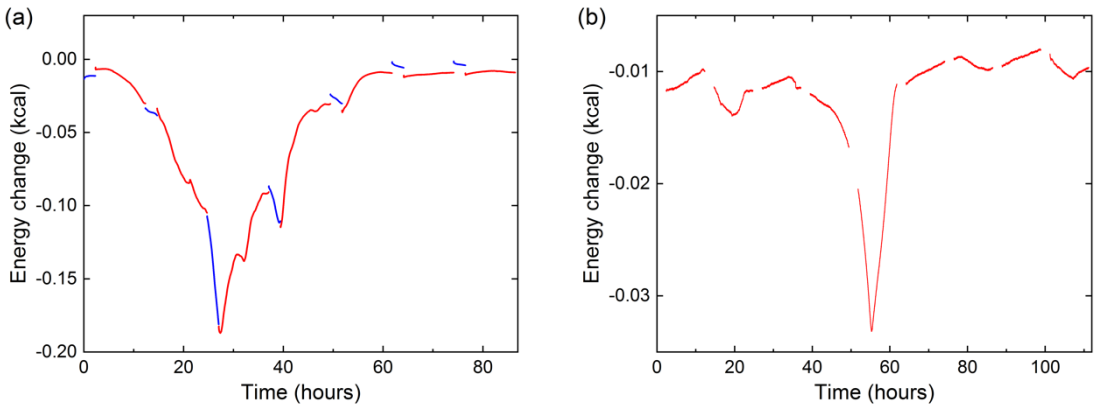

Figure 23. Time-resolved quasi-isothermal DSC measurements of two samples: (a) pure DLPE, (b) 90:10 DLPE:DLPG (mole %). The exothermic peak seen in both occurs at similar times as in the scattering experiments. The red curves (shown in both) are heating scans and the blue curves shown only in (a) are cooling scans. There is a mismatch between cooling and heating scan data possibly due to the different scanning rates, thus the cooling scans were shifted in (a) and omitted from (b), for clarity. Figure taken from Ref. 75.

3.1.2.5 Long-range spatial coordination

In the process of sample measurement and analysis of the phase-transition dynamics, the extracted temporal parameters represent the transformation occurring in the illuminated volume. However, this volume includes only a portion of the lipid pellet at the bottom of the capillary. If one follows a nucleation and growth framework, it is important to assess whether the transformation initiates concurrently throughout the sample or propagates successively from a starting point. To test this, we prepared a sample with a large pellet of several millimeters at the bottom of the capillary and measured the delay time at different locations along the vertically held capillary. Figure 24a shows the delay time as a function of the spatial coordinate along the capillary. The transition seems to propagate outward from a certain location, with neighboring locations transitioning at later times.

A similar experiment was performed on a horizontally held capillary. There, the transition began at the water–pellet interface and propagated at a steady velocity of approximately 100 μm hour^{-1} towards the end of the pellet (Figure 24b). In both experiments a new feature in the scattering spectra could be observed: a coordinated increase in lamellar scattering over a period of time prior to the transition (Figure 24c and Figure 24d). We denote the beginning of this period by τ_B, the point in time from which a slow increase in scattering culminates in a sharp drop of intensity. During this period, the amplitude of the peak increases significantly, which

implies an increase in the average number of scattering lamellae. In addition, the width of the peak slightly increases as well (Figure 25). The width of the scattering peak is inversely proportional to the number of lamellae in correlation per membrane stack[69]. Therefore, if stacks of correlated membranes would grow during the period before the transition (starting at τ_B), the peak amplitude would increase, but the width would decrease. However, the data shows an increase of both. This implies an increase in the number of different, independent stacks of correlated membranes, prior to crystallization. Only after the drop in the lamellar scattering intensity is there a detectable change in wide-angle scattering. Therefore, the metastable state remains during the build-up period. Surprisingly, this structural reorganization is coordinated over several millimeters in the sample (Figure 24c and Figure 24d).

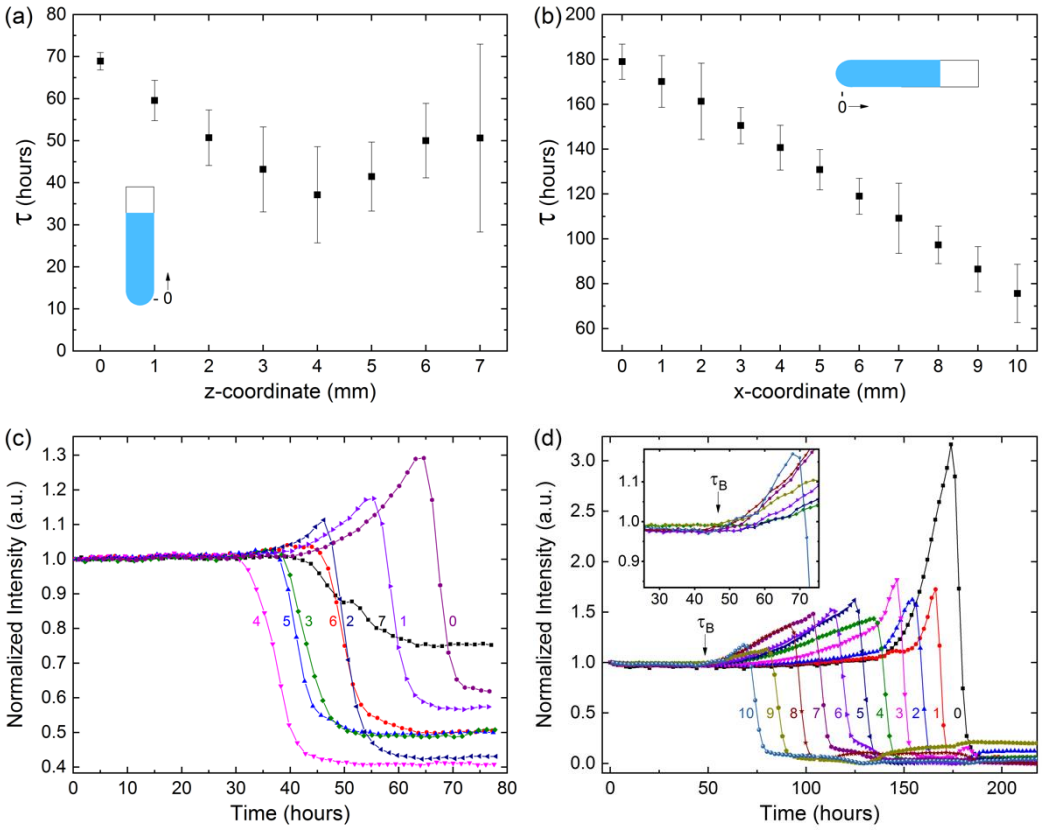

Figure 24. The delay time occurs at different times for different locations, but structural changes to the lipid particles are coordinated over millimeters. Delay time vs. spatial coordinate in vertically (a) and horizontally (b) held capillaries. (c-d) Time-resolved scattering intensity of (001) as a function of time of (a) and (b), respectively. Error bars in (a) and (b) represent τ^*, the duration of the transition. Numeric tags in (c) and (d) correspond to spatial coordinate in (a) and (b), respectively. Inset in (d) shows τ_B, the beginning of the build-up period. Figure taken from Ref. 75.

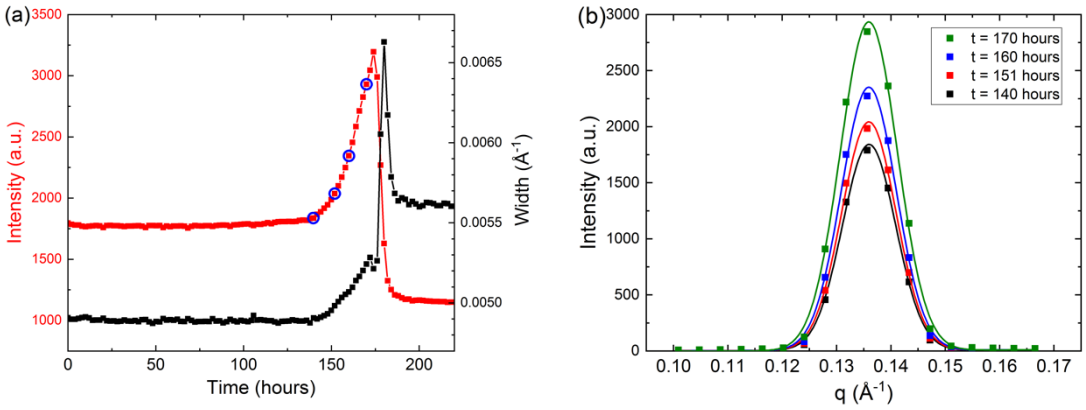

Figure 25. (a) The amplitude and width of the Gaussian fit to the (001) lamellar scattering peak as a function time. Data shown is from the bottom of the horizontally held capillary (coordinate x = 0). At t = 140 hours begins a significant increase of the amplitude, which ends with a sharp drop of the intensity during the phase-transition. Notably, the width of the gaussian also slightly increases before the transition. Blue circles mark the times at which the scattering peak and its fit are plotted in (b) for clarity. Figure taken from Ref. 75.

3.1.2.6 Mechanical agitation shortens the metastability

Metastable phases are often very sensitive to energy fluctuations as even minute inputs of energy can result in a transition to the stable phase. Since the lipid metastable phase is stable against various changes in system parameters, we tested its stability against external inputs of energy by subjecting lipid dispersions to mechanical agitation in the form of rigorous pipetting.

A lipid dispersion of approx. 1.5 ml, at 30 mg ml^{-1}, was prepared as a bulk dispersion from which samples would be pipetted out and measured intermittently. It was incubated at 37°C for one hour, followed by 3 hours at 60°C, as performed regularly with the X-ray scattering samples. The incubator was then set to T_Q = 37°C and a sample was drawn from the bulk dispersion after t = 1, 2, 3, 5.5 and 19.5 hours by pipetting out approximately 100 µl and placing into a capillary. The capillary was then placed in the WAXS temperature chamber, pre-heated to 37°C, and measured after Δt minutes (Figure 26). The control sample, taken from the bulk dispersion before it was placed in the incubator, underwent the regular temperature procedure in the WAXS temperature chamber, and transitioned after τ = 19.5 hours.

The samples from the bulk dispersion, taken during the first few hours, transitioned approximately an hour after being pipetted out. The sample taken after 5.5 hours was in the middle of transitioning when measured initially (Δt = 0 min), and the 19.5 hour sample had already transitioned (Figure 26). This experiment demonstrates that the lifetime of the metastable phase is significantly shortened by mechanical agitation applied after thermal incubation.

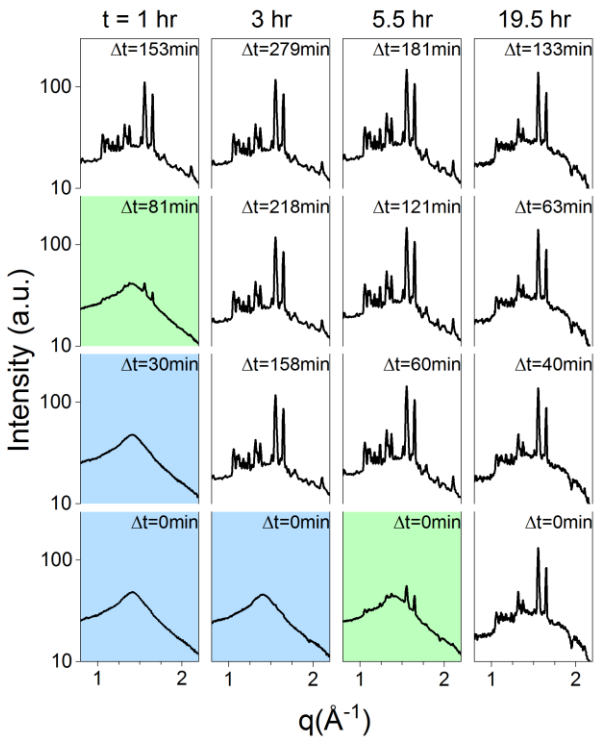

Figure 26. The metastable state's lifetime is significantly shortened by applying mechanical agitation in the form of rigorous pipetting. From left column to right, samples that were taken from a bulk reservoir t = 1, 3, 5.5 and 19.5 hours after temperature quenching from T = 60°C to T_Q = 37°C. Each sample is subjected to pipetting and measured immediately after extraction and Δt minutes afterwards. Blue background indicates the sample is still in the metastable L_α phase, and green that the sample is mid-transition. Figure taken from Ref. 75.

3.1.2.7 Effects of cargo

Lastly, phospholipids are utilized in bio-medicine as building blocks of vesicles designed for specific targeting and controlled release. When designing such drug-delivery systems, it is crucial to assert the stability of the carrier with its cargo. Since DLPE and DLPG have been used as the lipid components of such systems[78–80], we tested the stability of the metastable phase in the presence of cargo.

Figure 27 shows the delay time of samples containing 90:10 DLPE:DLPG (mole %) and the hydrophobic drug Prednisolone; an established and commercially available steroid used to treat a wide range of conditions and illnesses. The results show that the addition of the drug had a large impact on the delay time, shortening it by almost an order-of-magnitude. Since lipid systems continue to serve as appealing ingredients in drug delivery systems, controlled delayed nucleation may serve as a novel designing factor to deposit cargo in a predetermined timing. Nonetheless, the effect of cargo on transition dynamics should not be overlooked when designing such systems.

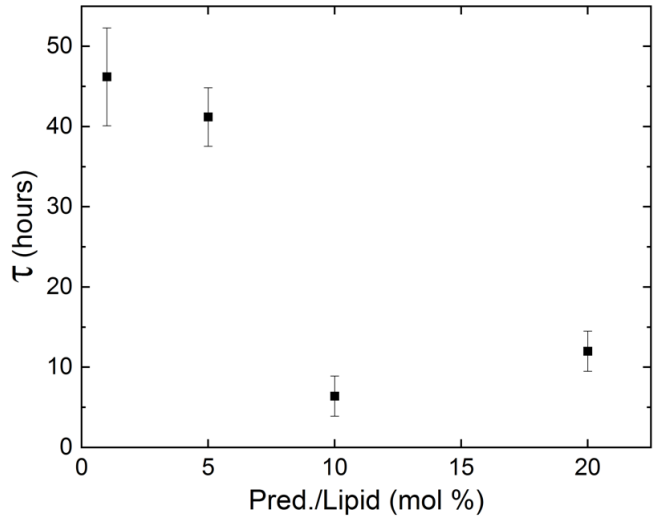

Figure 27. The delay in transition still persists in the presence of prednisolone, a commercial hydrophobic drug, but it decreases the delay time. Figure taken from Ref. 75.

3.1.3 Scaling and reproducibility

Since the thermodynamic state of DLPE at 37°C is a dehydrated lamellar crystalline structure, perturbations applied initially (e.g., sonication – a common method to treat lipid dispersions), would be absent at 37°C following the metastability. Hence, the lipid particles at T_Q without additional homogenization or defect reducing procedures were chosen as the starting point for the investigation of the metastability. In fact, dynamic light scattering (DLS) measurements could not determine the size distribution of the particles, indicating high poly-dispersivity in the samples. Supported by the Cryo-TEM images, we were able to detect that initial crystalline structures range from 0.5 to 10 mm in size. Nevertheless, the dozens of different samples prepared in this study showed the delayed metastability in a robust and reproducible manner.

The findings presented so far are in clear contrast to those expected from a system described by classical nucleation theory. Instead of a single stochastic process, which would produce a single timescale for the transition, we present multiple experimental evidence of coordinated delayed nucleation and multiple timescales (τ, τ^* and τ_B), representing the complexity of the dynamics. These timescales are orders of magnitude larger than the typical microscopic timescales associated with lipid systems. To emphasize the separation of timescales and highlight the collective behavior of the transition, we re-scale our entire data set of lamellar-scattering peak intensities by the delay time τ (Figure 28). The time-dependent intensities collapse onto roughly the same sigmoidal shape, with slight variations in width representing the variations in τ^*.

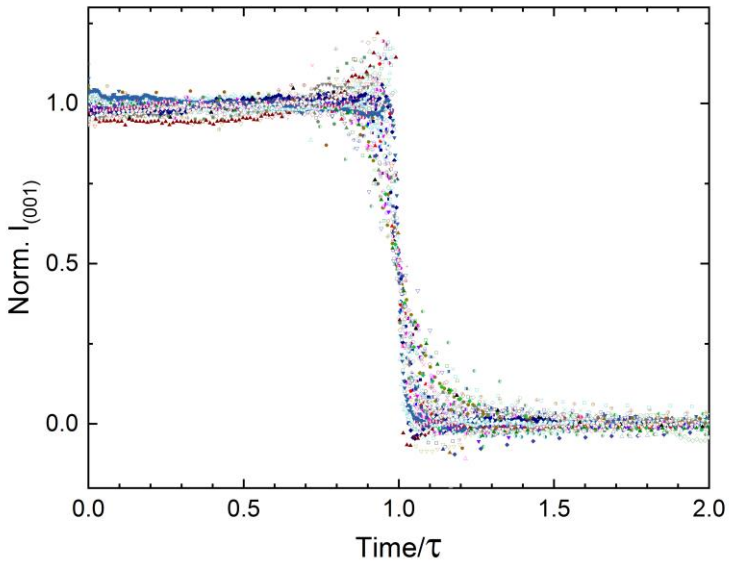

Figure 28. The lamellar correlation peak intensity over time can be re-scaled by τ to highlight the cooperative nature of the transition, regardless of the conditions changed in the experiments. The residual variation in the time-dependent scattering curves is due to τ^*. The data set presented here consists of 85 different experiments. Figure taken from Ref. 75.

To address reproducibility, we show the delay time distribution of 42 samples containing 95:5 DLPE:DLPG (mole %) (Figure 29). The distribution has an average delay time of $<\tau>$ = 36.5 hours, and a standard deviation of 15.9 hours, resembling the average duration of the phase-transition $<\tau^*>$ = 17.9 hours.

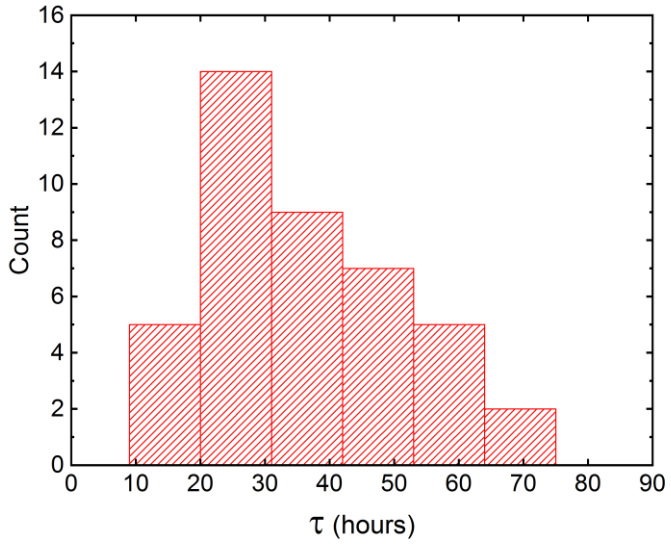

Figure 29. Distribution of τ from measurements of 42 different samples containing 95:5 DLPE:DLPG at 150 mM monovalent salt. The distribution has a mean delay time of $<\tau>$ = 36.5 hours and a standard deviation of 15.9 hours. The minimal delay time measured was 9.7 hours.

If the metastability were to stem from a stochastic Poisson process, as expected from a classical barrier-hopping model, the distribution of the time until crystallization would be exponential. However, the shape of the distribution does not resemble an exponential, and moreover, there were no occurrences of the delay time being shorter than 9 hours. We hypothesize that partial insolubility of DLPE may lead to uncontrolled polydispersity in the desired lipid ratio and could be the cause for a wide delay time distribution.

3.1.4 Lipid bilayer structural characterization

Reconstructing the electron density profile of the lipid bilayer is an essential part in the study of uni- or multi-lamellar lipid systems. This can be achieved by means of a discrete Fourier synthesis, while sampling the continuous form factor at q-values pertaining to lamellar correlation peaks. However, reconstruction is also possible using a continuous method, which takes advantage of the full q-range scattering line shape. I applied such a continuous fitting method, which utilizes a modified Caillé theory structure factor in combination with a Gaussian model representing the electron density profile[65,67]. In this approach the diffuse scattering between Bragg peaks is considered, in addition to a divided contribution by multi- and uni-lamellar vesicles. Moreover, this method allows for the derivation of additional structural parameters.

In Figure 30 I show the result of the line-shape analysis and fitting to pure DLPE in solution, in the metastable L_α phase, a few hours after cooling from 60°C to 37°C. The fitting procedure produces an electron density profile (Figure 31) and fitted parameters (Table 1). In addition, the derived structural parameters, which agree with previous studies[64,83], are summarized in Table 2.

The fitting process involves setting constraints for the fitting parameters. Those constraining values reflect physical/chemical knowledge of the system. Some of the parameters prove difficult to accurately assess for the convergence of the fit, such as the average number of lamellae per vesicle and the fraction of uni-lamellar vesicles (not contributing to the lamellar Bragg peaks). This degeneracy is probably due to the high polydispersity in the samples.

We noticed the scattering profile of mixed DLPE/DLPG dispersions show a widening of the Bragg peak bases with respect to the DLPG content (Figure 32). Such change in the scattering line-shape trend can be achieved by changing either the fluctuation parameter (η) or the Gaussian width representing the electron density of the hydrocarbon tails (σ_C). However, these lipids mixtures present a more complex system than the single component model used for the fit. Therefore, the fitting procedure is unable to accurately model the physical changes occurring in the system with the addition of DLPG.

As mentioned in Section 3.1.1, the Bragg peak of the second harmonic, denoted (002), is absent only for the initial crystal phase[55,76] (Figure 10). In order to explain the disappearance of the (002) reflection in the crystallized state, we assume a unit cell of two identical lipid molecules comprising a symmetric bilayer of length *d*, with the molecules' chains facing each other in opposite directions. The form factors of both molecules are given by

$$f_1(k) = \int_0^{d/2} dz\, \rho(z) e^{-ikz},$$

$$f_2(k) = \int_{\frac{d}{2}}^{d} dz\, \rho(d-z) e^{-ikz} = e^{-ikd} f_1(-k).$$

Due to the electron density being real, it follows that

$$f_1(-k) = f_1^*(k).$$

Therefore, the intensity of the Bragg peak at $k = \frac{2\pi}{d} n$ is proportional to

$$\left(f_1(k) + f_1^*(k)\right)^2.$$

Finally, the intensity of the second harmonic is given by

$$I_{002} = \left(\int_0^d dz\, \rho(z) \cos\left(2\frac{2\pi}{d} z\right)\right)^2.$$

The removal of water from between the lamellae in the crystal state, while maintaining a similar repeating distance, can be described as the elongation of the hydrocarbon chains in an extended conformation of the lipid molecules. To account for the conformational change, we increased the width and lowered the amplitude of the hydrocarbon chains' Gaussian and increased the head-to-head distance. We find that by varying the head-to-head distance by less than 10%, while maintaining the area of the hydrocarbon Gaussian (within 1%), we can reduce the (002) reflection scattering profile by orders of magnitude. The altered fitting parameters for the crystal state are shown in Table 1.

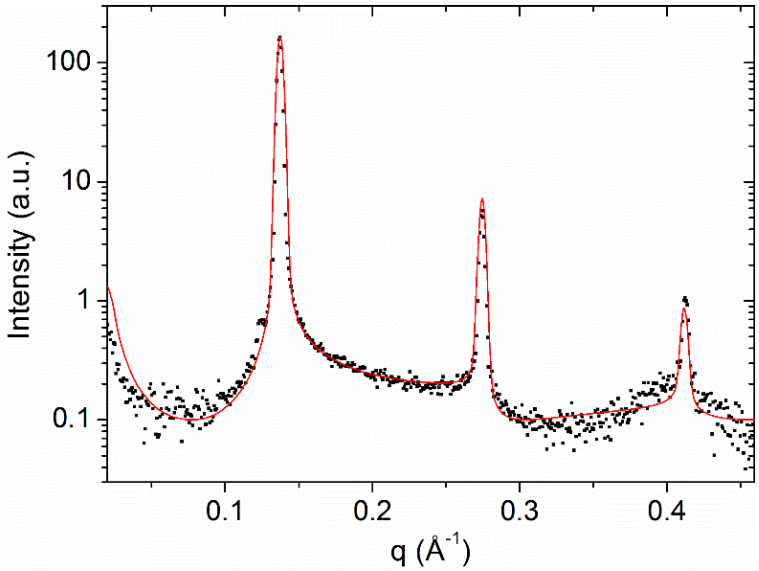

Figure 30. Full q-range fit using line-shape analysis software GAP (Section 2.1.2). X-ray scattering data (points) and the line-shape analysis fit (red curve). Features like the diffuse scattering around Bragg peaks are taken into account in the fitting process. Discrepancies between the data and the fit arise due to the model's limited ability to account for a multi-component system with high polydispersity. Data shown of sample containing DLPE in 150 mM monovalent salt solution. Figure taken from Ref. 74.

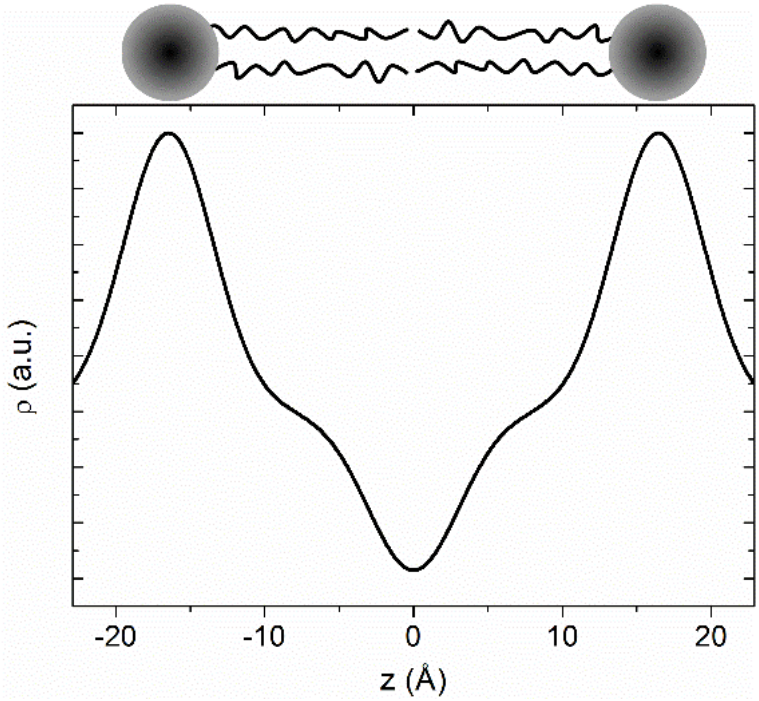

Figure 31. Bilayer electron density profile of DLPE. Profile generated from the fitted scattering curve using line-shape analysis software GAP (Section 2.1.2). Figure taken from Ref. 74.

Fit parameter	T = 37°C	
	L_c	L_α
Z_H (Å)	17.8	16.46
σ_H (Å)	3	3
ρ_C (e/Å^3)	-0.354	-0.57
σ_C (Å)	5	3.064
d (Å)	45.78	45.78
η_1	0.01	0.017
N	297.4	297.4
N_{diff}	0	0

Table 1. Fitting parameters for line-shape analysis both at the crystalline and metastable phases. Fitting parameters are presented as in Refs. 65,67. Right column (denoted L_α) displays the fitting parameter results for a sample at 37°C, 1 hour after cooling back from 60°C. Left column (denoted L_c) displays the fitting parameters for a sample at 37°C prior to heating, which diminish the (002) reflection. Fitting performed on scattering data from samples containing 95:5 DLPE:DLPG (mol:mol%) in 150 mM monovalent salt solution, using GAP software provided by Dr. Georg Pabst and Refs. 65,67. Table taken from Ref. 74.

Structural parameter	37°C		35°C§
	L_c	L_α	
Area per lipid (A)	45.4 Å^2	50.4 Å^2	51.2 Å^2
Bilayer thickness (d_B)	42.7 Å	40 Å	42.8 Å
Chain length (d_C)	14.3 Å	12.9 Å	12.9 Å
Water layer thickness (d_W)	3.1 Å	5.8 Å	5 Å
Total number of water molecules per lipid† (n_w)	7.7	10.8	8.8
Number of free water molecules per lipid‡ (n^*_w)	2.3	4.9	4.1

Table 2. Structural parameters derived from the fitting parameters in Table 1, according to the procedures in Ref. 65, along with the values given in Ref. 64 for comparison.
†including water molecules inside the headgroup, ‡water layer between opposing headgroups, §values taken from Ref. 64. Steric parameters: D_B', D_C, D_W', (n_W - n_W'). Table taken from Ref. 74.

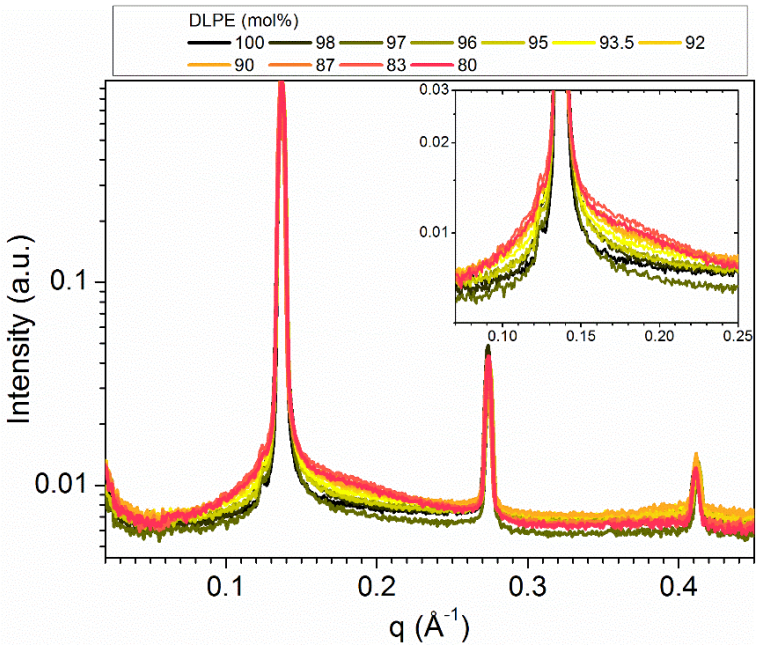

Figure 32. Scattering of mixed DLPE:DLPG samples. Widening of the Bragg peak bases with respect to the DLPG content is observed. Figure taken from Ref. 74.

3.1.5 Lipid crystallization in MLVs

This section details a theoretical model that describes the underlying physical mechanism responsible for the metastability and the strong cooperativity of the transition. The work on this model was done in collaboration with Prof. Haim Diamant from the School of Chemistry, Tel Aviv University.

3.1.5.1 Single isolated membrane

First, we shall restrict ourselves to a domain in a single isolated membrane. Its free-energy has a negative contribution due to phase separation and a positive contribution due to interfacial line tension,

$$F_1^{(0)}(r) = -(\pi r^2)\Delta g + (2\pi r)\alpha, \tag{9}$$

where Δg and α are the liquid/solid difference in chemical potential per unit area and line tension per unit length, respectively. Crystallization occurs at $\Delta g = 0$, corresponding to the crystallization temperature $T = T_c^{(0)}$, with a critical radius $r_{nuc}^{(0)} = \alpha/\Delta g$ and nucleation barrier

$$F_{nuc}^{(0)} = \pi\alpha^2/\Delta g. \tag{10}$$

We can find $\Delta g(T)$ for $T < T_c^{(0)}$, using the heat of transition per molecule h_c, by expanding $\Delta g(T) = -\left(g_c(T) - g_l(T)\right)/a$ around $T_c^{(0)}$, where g_c and g_l are the chemical potentials of the crystalline and liquid phase, respectively, and a is the area per lipid. We get $\Delta g(T) \simeq \left(T - T_c^{(0)}\right)(\partial(\Delta g)/\partial T)_c = \left(T - T_c^{(0)}\right)(s_c - s_l)/a$, where s_c and s_l are the entropy of the crystalline and liquid phases, respectively. And so,

$$\Delta g(T) \simeq h_c a^{-1}\left(T_c^{(0)} - T\right)/T_c^{(0)}. \tag{11}$$

3.1.5.2 Crystallization of a single membrane in the stack

Now, we would like to find how crystallization is affected by the arrangement of membranes in a spherical stack. Let's consider a multi-lamellar vesicle (MLV) of N membranes, with radius R and periodicity λ. The individual membranes have thickness δ and bending modulus κ. The stack has a compression modulus B and bending modulus $K = \kappa/\lambda$, giving it an effective surface tension[12] $\gamma = \sqrt{BK}$. The temperature is lowered $T < T_c^{(0)}$, such that an isolated membrane would crystallize via a first-order transition. Namely, the free energies per unit area of the liquid and solid phases satisfy $\Delta g \equiv g_l - g_s > \Delta g\left(T_c^{(0)}\right) = 0$.

In this case, when considering a circular crystalline domain of radius $r \ll R$ on the outer membrane of the MLV (the same qualitative argument holds also for a membrane inside the stack), the rigidity of the domain makes it essentially flat, deforming the stack down to a penetration depth of $l_p = \sqrt{K/B}$ (Figure 33).

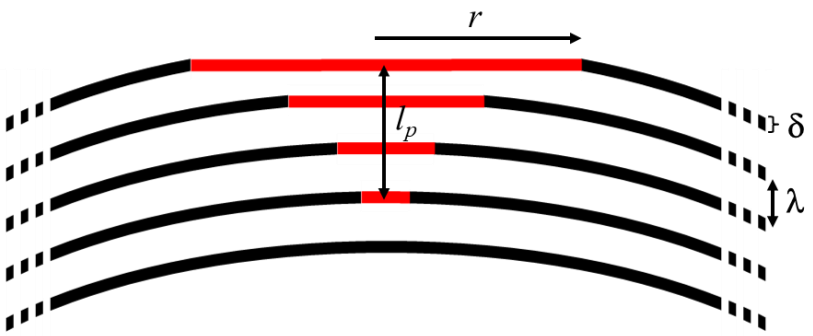

Figure 33. Schematic of a section of a large MLV with periodicity λ and membrane thickness δ, along with a crystalline domain (red) of radius r on the outer membrane, deforming the stack down to a depth l_p.

Under a fixed-volume constraint, the deformation increases the area of the MLV by

$$\Delta A(r) \simeq \frac{2\pi r^2}{3}\left(1 + \frac{7}{24}\frac{r^2}{R^2}\right), \tag{12}$$

resulting in a free-energy penalty, $\gamma\Delta A$, being added to $F_1^{(0)}$ (assuming that Δg and α are the same as in an isolated membrane and neglecting additional deformations in the line-tension of order $\mathcal{O}\left(\frac{r^2}{R^2}\right)$ or higher). The free-energy of the domain then becomes

$$F_1(r) = -\pi\left(\Delta g - \frac{2\gamma}{3}\right)r^2 + 2\pi\alpha r. \tag{13}$$

The first point to notice is that the free-energy per unit area of the solid phase has changed, due to the deformation, from g_s to $g_s + 2\gamma/3$. As a result, the transition temperature is shifted from $T_c^{(0)}$ to $T_c < T_c^{(0)}$, such that $\Delta g(T_c) \equiv \Delta g_c = 2\gamma/3$ (neglecting a correction of order $\mathcal{O}\left(\frac{\alpha}{\gamma R}\right)^{2/3} \ll 1$).

We can numerically estimate the shift in transition temperature using Eq. (11) and experimental values. By substituting the enthalpy $h_c = 11\,kcal/mole = 18.5\,T_{300}$ (T_{300} is the thermal energy k_BT at $T = 300K$), area per lipid $a = 0.5\,nm^2$, $T_c^{(0)} = 43\,°C$ and the effective surface tension $\gamma = 1\,T_{300}/nm^2$, we get $T_c \simeq 37\,°C$. Increasing γ to $2\,T_{300}/nm^2$, reduces T_c to $32\,°C$. This shows that in the experiments we have $0 < \Delta g < \Delta g_c$, i.e., *crystallization of a single membrane within the stack is suppressed*.

3.1.5.3 Crystallization of a membrane stack

We are now in a situation where, on the one hand, there is a molecular preference to crystallize ($\Delta g > 0$), yet, on the other hand, crystallization of a single membrane is suppressed ($\Delta g < \Delta g_c$). This implies that the stack must ultimately crystallize, but only through a multi-membrane cooperative process. A key point to notice is that the free-energy penalty due to deformation is intensive in the number of membranes (because of the finite penetration depth l_p from the edges of the stack), whereas the free-energy gain due to crystallization is extensive. Thus, for a sub-stack of n crystalline membranes the free-energy per unit area per membrane is $-\Delta g + 2\gamma/(3n)$, so that for a sufficiently large sub-stack,

$$n > n^* = \frac{2\gamma}{3\Delta g}, \tag{14}$$

crystallization is no longer suppressed. According to the experimental values used above, this should not be more than a few membranes.

3.1.5.3.1 Free-energy

Other than the deformation free-energy, which owes its existence to the stack's spherical shape, we treat the membranes as flat and parallel. The total free-energy of the stack is

$$F = \sum_{n=1}^{N} \int d^2\boldsymbol{\rho} \left[\frac{1}{2} C |\nabla_\perp \phi_n|^2 + g(\phi_n) + \frac{2\gamma}{3n}\phi_n + \frac{1}{2} E \lambda^{-2} (\phi_n - \phi_{n-1})^2 \right], \tag{15}$$

where $n = 1$ is taken as the outer membrane. Here, $\phi_n(\boldsymbol{\rho}) \in [0,1]$ is a local order parameter at the two-dimensional position $\boldsymbol{\rho}$ on membrane n, $\nabla_\perp$ is a 2D gradient, and C and E are the interfacial stiffness coefficients parallel and perpendicular to the membranes, respectively.

The first term is related to the solid/liquid line tension, i.e., the penalty for creating an interface on a single membrane. The second term, the free-energy per unit area, $g(\phi)$, accounts for the liquid/solid transition in an isolated membrane (e.g., a Landau free-energy), such that $g(\phi = 0) = g_l$ and $g(\phi = 1) = g_s$. The third term accounts for the deformation penalty. The last term accounts for the coupling between adjacent membranes, suppressing changes in ϕ across layers. It is related to the free-energy of the experimentally observed alignment of domains[85] – adjacent liquid and solid domains are less favorable than either two liquid domains (due to fluctuation entropy) or two solid ones (due to attraction)[86].

The anisotropy of the system can (almost) be eliminated from the model by replacing the discrete index n with a continuous and rescaled coordinate z according to

$$z \equiv \lambda \sqrt{C/E}\, n. \tag{16}$$

Note that z is not the actual perpendicular coordinate, $z_{real} = \lambda n$, but is dilated or compressed by a factor of $\sqrt{C/E}$. The transformation turns the free-energy into

$$F = \lambda^{-1}\sqrt{E/C}\int d^3\boldsymbol{r}\left[\frac{1}{2}C|\nabla\phi|^2 + g(\phi) + \frac{\beta}{z}\phi\right], \tag{17}$$

where now $\phi = \phi(\boldsymbol{r})$, $r = (\boldsymbol{\rho}, z)$ is a 3D position vector, and ∇ is a 3D gradient. The transformation has turned the interfacial stiffness coefficients C and E into a single isotropic stiffness. The deformation term, with $\beta = 2\gamma\lambda\sqrt{C/E}/3$, still breaks rotational symmetry.

3.1.5.3.2 Critical nucleus

To find the 3D critical nucleus we examine the (unstable) solution of the equation $\delta F/\delta\phi = 0$. The resulting equation is

$$C\nabla^2\phi - g'(\phi) - \beta/z = 0. \tag{18}$$

We consider a roughly spherical nucleus of radius R_c. This oversimplification is meant to get an estimate for the characteristic size of the nucleus. The nucleus is assumed spherical in the dilated/compressed coordinate; in the real coordinate it is an elongated spheroid of aspect ratio $\sqrt{E/C}$. Since C and E are related to lipid cohesion within a membrane and between adjacent membranes, respectively, the aspect ratio should not be far from unity. Assuming the interface between the phases is sharp on the scale of R_c, we approximate Eq. (18) as

$$C\left(\partial_{rr}\phi + \frac{2}{R_c}\partial_r\phi\right) - g'(\phi) - \frac{\beta}{R_c} = 0. \tag{19}$$

Multiplying by $\partial_r\phi$ and integrating radially from the center of the nucleus (where $\phi = 1$) to a point far away from it (where $\phi = 0$), we get

$$R_c = \frac{4\lambda\sigma\sqrt{C/E} + \beta}{\Delta g}, \tag{20}$$

where

$$\sigma \equiv \frac{1}{2}\lambda^{-1}\sqrt{CE}\int dr(\partial_r\phi)^2 \tag{21}$$

is an effective 3D surface tension. We expect $\gamma < \sigma < \alpha/\lambda$. The number of membranes in the critical nucleus is $n_c = \sqrt{E/C}\,R_c/\lambda$, which gives

$$n_c = n^*(1 + 6\sigma/\gamma), \tag{22}$$

where $n^* = 2\gamma/(3\Delta g)$ as presented above in Eq. (14). The fact that we got a nucleus larger than n^*, the number of membranes required to overcome the suppression of the transition,

makes the analysis consistent. In fact, since $\sigma > \gamma$, we have n_c significantly larger than n^*, i.e., the critical nucleus contains at least a few tens of membranes.

Based on the classical nucleation theory for the free-energy as a function of domain radius, we estimate the nucleation barrier as

$$F_c = \frac{4\pi}{3}\sigma R_c^2 = \frac{4\pi}{3}\sigma\lambda^2(C/E)n_c^2, \tag{23}$$

which is orders of magnitude larger than T (since $\sigma\lambda^2 > \gamma\lambda^2 \gtrsim T$, which is then multiplied by n_c^2, amounting to many T).

3.1.5.4 Fitting experimental data

To compare with the experiment discussed in Section 3.1.1.1, we use Eqs. (14), (22) and (23) to rewrite

$$F_c = \frac{64\pi}{3}(C/E)\frac{\sigma^3\lambda^2}{(\Delta g)^2} = \frac{64\pi}{3}(C/E)\sigma^3\lambda^2\frac{a^2}{h_c^2}\left(\frac{T_c^{(0)}}{T_c^{(0)} - T}\right)^2. \tag{24}$$

We have assumed $6\sigma/\gamma \gg 1$ and replaced the quench Δg by its estimate given in Eq. (11). The barrier diverges near $T_c^{(0)}$, as it should, as the original (isolated-membrane) transition point is approached. We can now express the delay time in the form

$$\tau = \tau_0 e^{F_c/k_B T} = \tau_0 e^{b/\left(T_c^{(0)} - T\right)^2}, \tag{25}$$

where the coefficient b is extracted from Eq. (24). Using the experimental values of λ, a, h_c, and $T_c^{(0)}$, and taking $\sigma \sim 0.05\, T_{300}\, nm^{-2}$, we get b of order $10\, K^2$. This value is sensitive to the value of σ and should be regarded just as a consistency check. Figure 16 above shows the fit of the function in Eq. (25) to the data, where $T_c^{(0)}$ was fixed to 43°C. The fitting parameter b yields a value of approximately $22\, K^2$, consistent with the qualitative estimate shown above. Changing $T_c^{(0)}$ to be 42 or 44°C changes b to be approximately 8 or 44 K^2, respectively.

3.2 Intrinsically disordered peptide amphiphiles (IDPAs)

The second project, presented in this section, focuses on the characterization of synthetic amphiphile self-assembly, used as a platform to study the interactions of IDPs and design novel systems for cargo hold-and-release. In addition to the experimental results, a theoretical model is proposed to describe the spherical-to-cylindrical micelle phase-transition (work done in collaboration with Prof. Michael Kozlov – Sackler School of Medicine, Tel Aviv University). Work on this project was done in collaboration with Prof. Roey Amir and his student Merav Segal Asher. These results are currently in preparation for submission for publication.

3.2.1 Synthesis and chemical characterization (CMC and CD)

IDPAs were synthesized by conjugating a short IDP to a hydrophobic tails via a connective aromatic ring (Figure 34). Two tail-group variants were used to create two IDPAs, named 2x12 and 4x7, with 2 chains with 12 hydrocarbons or 4 chains with 7 hydrocarbons, respectively. The peptide is a short polyampholyte, inspired by the intrinsically disordered tail-domain of the protein neurofilament-low (NF-L), found in the cytoskeleton of nerve cells[28,87–90]. The peptide's sequence, which is 18 amino acids long, includes 11 protonatable residues.

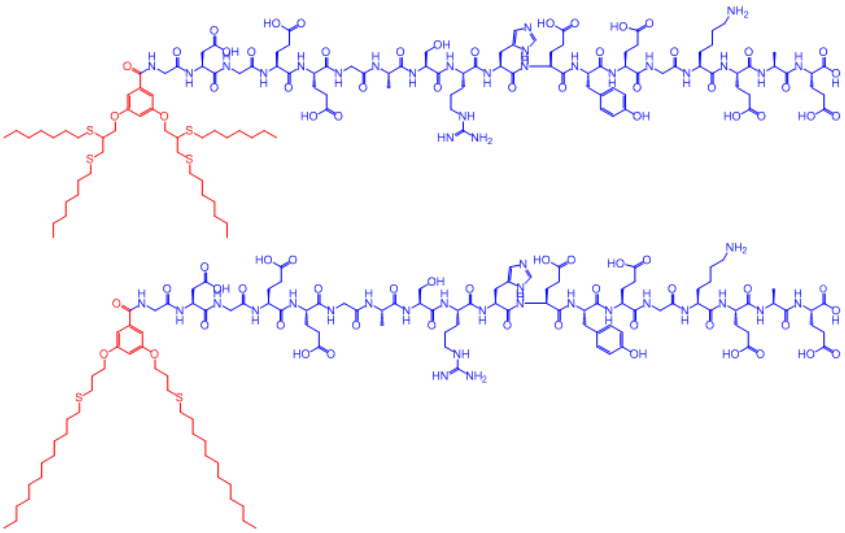

Figure 34. Variants of the synthesized IDPAs. Both 4x7 (upper) and 2x12 (lower) have the IDP sequence attached to tail groups via a connective group. The (one letter) amino acid sequence is: GDGEEGASRHEYEGKEAE.

Figure 35 shows the net charge and number of charged amino acids as a function of pH. Above pH 6 both are approximately constant. However, at approximately pH 5.5 a decrease in net charge and the number of charged residues can be seen, caused by the protonation of the Aspartic Acid and Glutamic Acid residues.

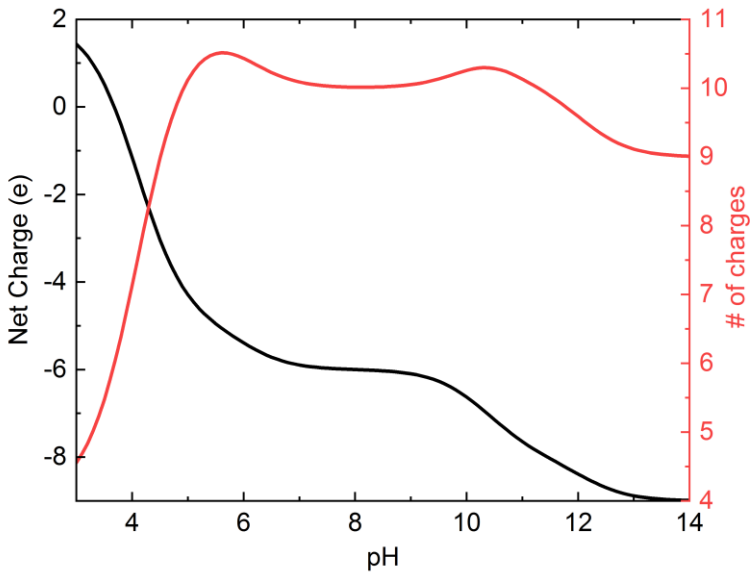

Figure 35. Net charge (black) and number of charged amino acids (red) of the IDP headgroup as a function of pH. The peptide's pI is approximately 3.9.

The CMC of both variants was determined using the solvatochromic dye Nile Red (Figure 36). Below the CMC the fluorescence intensity of the dye is minimal due to the polar environment. Above the CMC, when the IDPAs self-assemble, the fluorescence increases with the fraction of molecules in aggregates. A CMC of 5 μM is in the typical micro molar range for peptide amphiphiles[19,39,40,91].

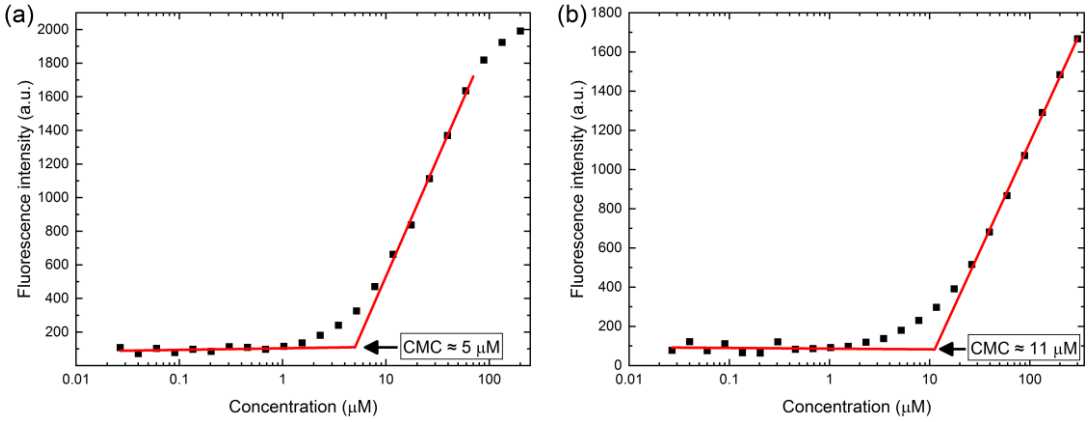

Figure 36. CMC measurements of (a) 2x12 and (b) 4x7 IDPAs. The CMC is taken to be the concentration at the intersection of the linear fits to the fluorescence intensity in both regimes. The concentrations are approximately 5 and 11 μM, respectively. Experiments performed by Merav Segal Asher.

3.2.2 Verifying the disorder

3.2.2.1 Circular Dichroism

The degree of disorder of the peptide was experimentally verified by measuring the CD spectrum of samples of the peptide (unconjugated) and the IDPAs. The free peptide and the conjugated peptide both display spectra that can be classified as disordered (lacking a secondary structure signal) (Figure 37).

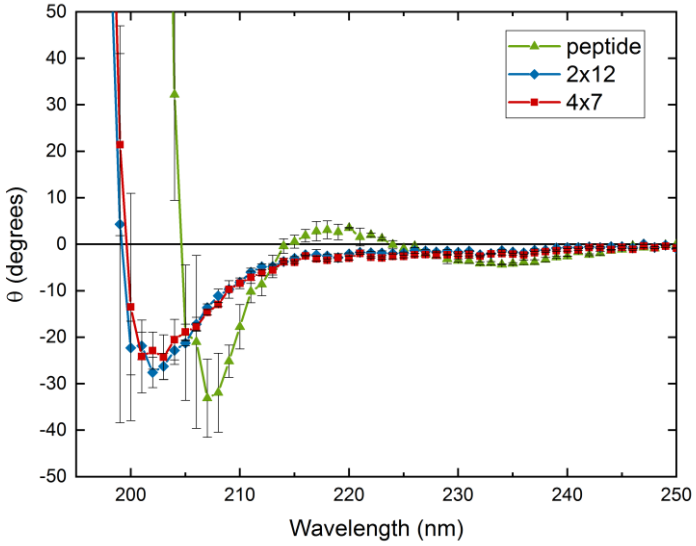

Figure 37. CD measurements of the IDPAs and the unconjugated peptide in phosphate buffer (the buffer was changed due to strong absorption of the normal buffers used for sample preparation). All show similar line shapes to that of an "irregular structure" (disordered)[73].

3.2.2.2 Software prediction

In addition, the peptide sequence was analyzed for disorder using software-based protein disorder predictors. Two predictors were used to predict the probability for disorder, PrDOS[92] and a more recent engine based on neural networks, NetSurfP-2.0[93], which provides additional information, such as surface accessibility and secondary structure assignment. Both predictors show a high probability for disorder in our sequence and the absence of regular secondary structure (the sequence is assigned the random coil structure by NetSurfP-2.0) (Figure 38).

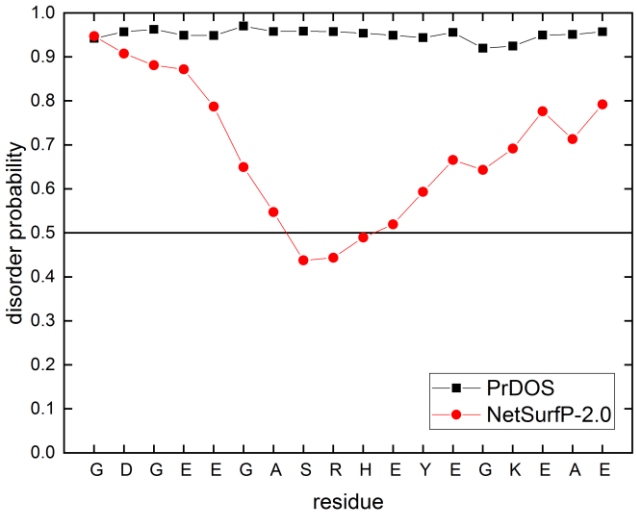

Figure 38. Results of software disorder predictions. The output of the PrDOS (black squares) and NetSurfP-2.0 (red circles), both showing a high probability for disorder of the peptide sequence.

3.2.3 Phase-transition characterization

As discussed in the introduction, amphiphile self-assembly is governed by a balance between the hydrophobic interactions of the tail-groups and the electrostatic interactions of the charged headgroups. Since the peptide is a strong polyampholyte, the IDPA self-assembly will depend on the pH of the solution, which determines the net charge of the headgroup and its distribution. Most of the protonatable residues have their pKa (the pH at which there are equal amounts of protonated and deprotonated forms of the acid) between 3 and 6, which means the largest change in net charge will be in that range. A decrease in net charge when the pH is lowered towards the pI (isoelectric point – the pH at which the average molecule's net charge is zero) can facilitate a phase-transition that depends on the charge density of the headgroup region.

The phase-space of the self-assembly was studied at different pH using turbidity measurements, SAXS and cryo-TEM. These techniques provided us with information on the pH dependence of the assembly (turbidity), accurate measurements of the spatial correlations present in each phase (SAXS), and direct observations of the structures in real-space that could be used to cross validate the information gathered from SAXS (cryo-TEM). For all three techniques, samples of both IDPAs were prepared in the pH range of 3-7.5.

3.2.3.1 Turbidity

Turbidity measurements performed on both IDPAs revealed a clear difference between pHs above 6 and below (Figure 39). This transition point indicates a change in the macromolecular

aggregation of the self-assembled structures present in solution. Above pH 6 the structures do not aggregate, while below 6, they increasingly interact to produce larger (and more ordered) aggregates. The images in Figure 39 showcase the transition from translucent solutions to opaque. From the turbidity measurements we could predict a turning point in the X-ray scattering profile of the samples.

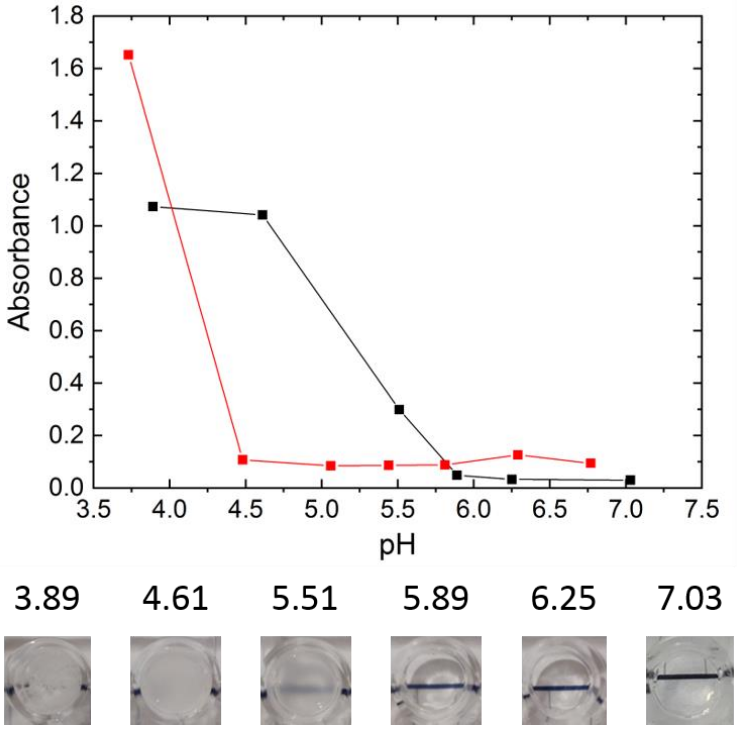

Figure 39. Turbidity measurement of 4x7 (black) and 2x12 (red) IDPAs. Results show an increase in turbidity when lowering the pH, indicating a transition into large aggregates. Below: photographs of the 4x7 samples measured in the experiment (numbers above photos indicate the pH), showcasing the change in turbidity.

3.2.3.2 SAXS and Cryo-TEM

3.2.3.2.1 Unconjugated IDP

The unconjugated peptide by itself was measured using SAXS at different pH, to test the effect of the charging state of the peptide on its folding. The peptide at each pH was measured at four different concentrations, and from this an extrapolation to zero-concentration was performed using the scattering data analysis software PRIMUS[94], to better approximate non-interacting peptides. From the low *q* regime of the zero-concentration scattering curves we extracted the radius of gyration (R_g) and the extrapolated forward scattering, I(0), using the Guinier analysis (Figure 40). When examining the values of R_g from high to low pH, it seems to remain a constant until pH ~5.5 and gradually increase below it. However, this increase in size can be

explained by an increase in the effective mass of the peptides (increase in forward scattering) due to a decrease in inter-peptide repulsion near the pI.

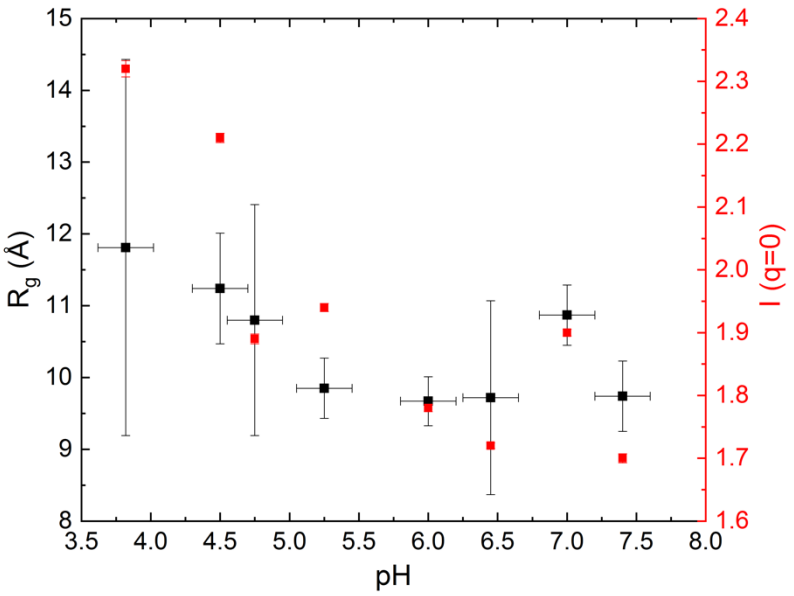

Figure 40. The radius of gyration extracted from the Guinier analysis at low *q* for the unconjugated IDP, as a function of pH. The observed slight increase in size is due to a decrease in repulsive interactions between the peptide closer to the pI, and an increase of forward scattering I_0.

3.2.3.2.2 IDPA

Figure 41 and Figure 42 show the SAXS data of IDPA 2x12 and 4x7 respectively. One can immediately notice the difference in scattering between high and low pH for each IDPA, and between the two IDPA variants at low pH. We shall discuss the high pH results first – show a form-factor fit to the scattering data and analyze the scattering data using a Kratky plot, followed by the results at low pH.

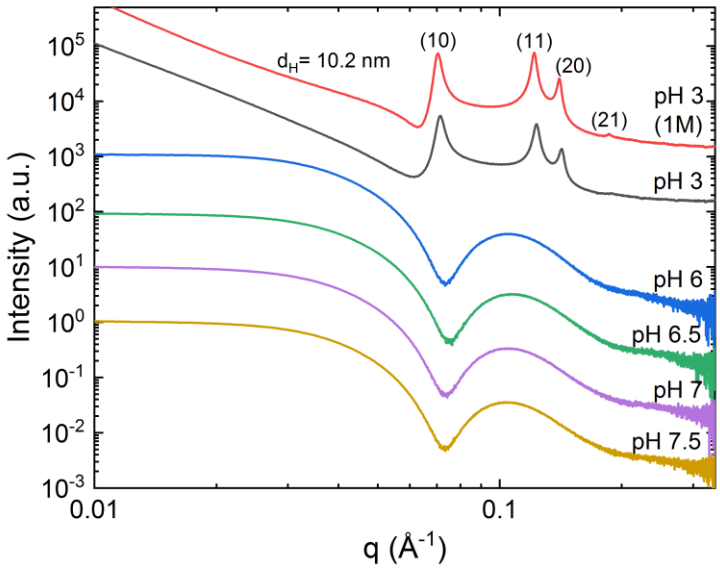

Figure 41. SAXS measurements of 2x12 at different pH. Above pH 6 the scattering profile pertains to spherical micelles. Below pH 6, the scattering is dominated by a structure factor of a hexagonal phase with a spacing of d_H = 10.2 nm. The red curve is a sample at pH 3 with 1M NaCl.

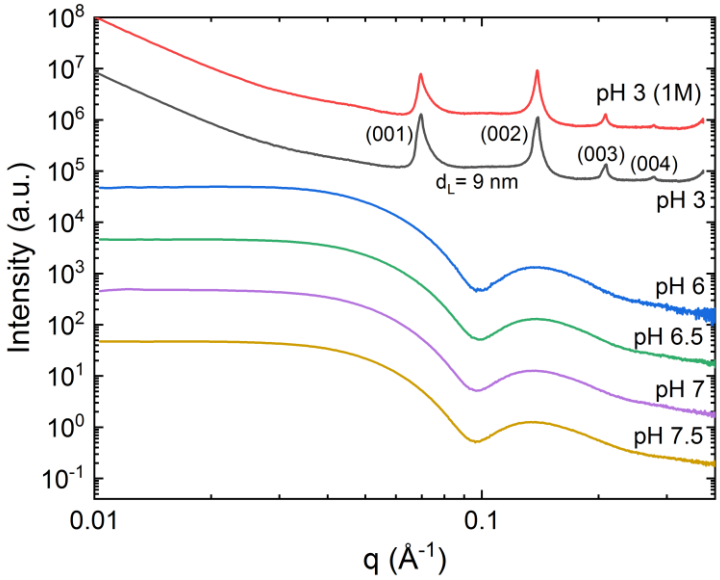

Figure 42. SAXS measurements of 4x7 at different pH. Above pH 6 the scattering profile pertains to spherical micelles. Below pH 6, the scattering is dominated by a structure factor of a 1D phase with a spacing of d_L = 9 nm. The red curve is a sample at pH 3 with 1M NaCl.

3.2.3.2.3 High pH - form factor fit

The scattering data of the IDPAs at pH 7.5 pertain to spherical micelles. A spherical core-shell form-factor was chosen to fit the SAXS data, using the X+ software[69]. The fit, as described in Section 2.1.3.2, provides the radius of the hydrophobic core $R_{core} = 1.25\ nm$, the width of the

peptide shell (headgroup region surrounding the core) $w_{shell} = 2.12\,nm$, as well as their respective average electron densities, $\rho_{core} = 284\,e/nm^3$ and $\rho_{shell} = 355\,e/nm^3$ (Figure 43).

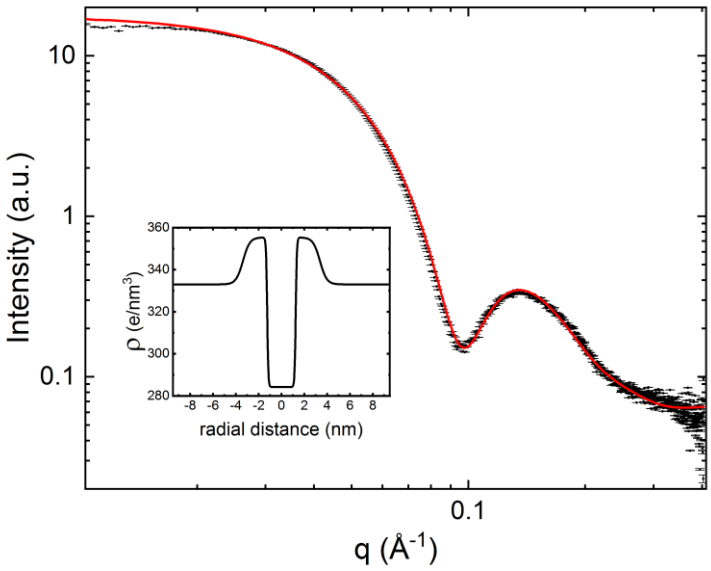

Figure 43. Spherical core-shell form factor fit to the SAXS measurement of 4x7 at pH 7.5 (2.5 mg/ml). Inset: corresponding radial electron density profile.

We can now estimate the total number of excess electrons in the headgroup layer,

$$Q = 4\pi \int_R^\infty r^2(\rho_{shell}(r) - \rho_{water})dr,$$

where $\rho_{water} = 333\,e/nm^3$ and $\rho_{shell}(r)$ is the radial electron density of the shell. Using Q we can now find the aggregation number of the spherical micelles,

$$aggregation\ number = Q/(\#e_{peptide} - v_{peptide}\rho_{water}),$$

where $\#e_{peptide}$ is the number of electrons per peptide and $v_{peptide}$ is the volume per peptide. The former can be calculated by considering the specific peptide sequence, and in our case, it comes out to be 1032 electrons per peptide. However, the volume can be estimated using different approaches. The total volume can be the sum of volumes of free amino acids or of residues (amino-acids in a peptide bond), and the volume of residues varies depending on the folding state of the protein (residues can be exposed to the solution or buried inside inner regions). The larger estimate for the total volume, using free amino acids, and the smaller estimate, using buried residues can be used as upper and lower bounds for the aggregation number. However, since our peptides are highly charged IDPs with a random coil structure according to the structure predictions in Section 3.2.2.2, it is reasonable to approximate the aggregation number using the larger estimate in our case. Using the values from Ref. 95 and

the electron density shown in Figure 43, we estimate the number of monomers for the 4x7 at pH 7.5 to be approximately 13.

3.2.3.2.4 Kratky analysis

A Kratky analysis[96] of the same data reveals composite dimensionality of the spherical micelles. The bell-shaped curve at lower *q* corresponds to the 3D nature of the micelle at larger length-scales, while the plateau at larger *q* suggests an unfolded state of the peptides at smaller length-scales (Figure 44).

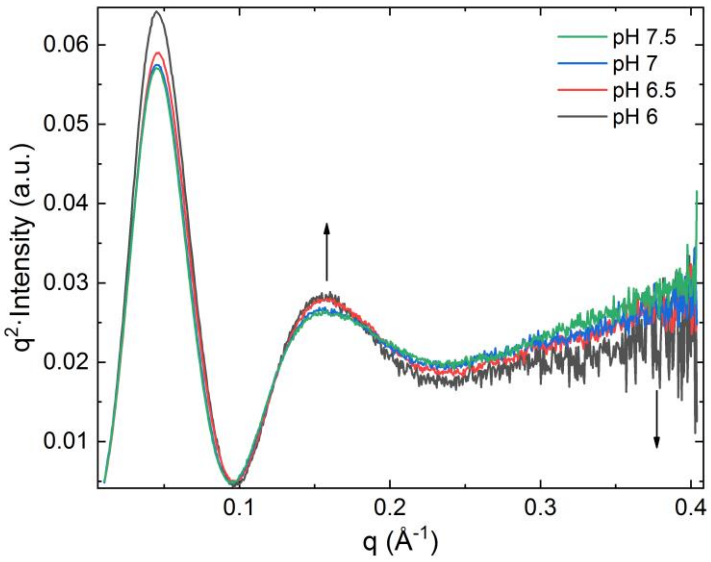

Figure 44. Kratky plot of the 4x7 data (pH 6-7.5) showing a bell-shape at long wavelengths, and a non-converging signal at short wavelengths. This indicates a mixture of the spherical nature of the micelles a longer length-scales and the unfolded state of the IDP at shorter length-scales. Arrows indicate the change in curve shape when pH nears the transition point. The peptides become less extended because they are less charged, seen as a decrease in divergence at short wavelengths.

3.2.3.2.5 Low pH – aggregation

At low pH the scattering is qualitatively different. It is no longer a sum of independent scattering from particles alone, producing a form factor scattering signal like shown above, but now includes an additional component. This additional scattering is the structure factor produced by the interaction between scattering objects that are in correlation[62]. It is seen as large peaks at specific scattering angles (*q*'s), implying inter-micelle correlations at specific length scales. The correlation peaks of both IDPAs can be indexed to match a 2D hexagonal lattice for 2x12 using: $q_{hk} = \frac{4\pi}{\sqrt{3}d_H}(h^2 + hk + k^2)$, and a 1D lattice for 4x7 using: $q_n = \frac{2\pi}{d_L}n$. The

corresponding lattice spacing can be calculated to be $d_H = \frac{4\pi}{\sqrt{3}q_{10}} = 10.2$ nm and $d_L = \frac{2\pi}{q_1} = 9$ nm, respectively.

3.2.3.2.6 Cryo-TEM

The scattering data alone, however, can sometimes be interpreted ambiguously, especially when different objects produce similar scattering profiles. To determine whether the IDPAs are still assembled as spherical micelles at low pH, or have transitioned to a different structure, real-space information from electron microscopy can be very valuable.

Cryo-TEM images of 2x12 samples at pH 3-5 revealed elongated worm-like micelles, rather than spheres (Figure 45). The images clearly show that the worm-like micelles are strongly interacting, which corroborates the conclusions drawn from the SAXS and turbidity measurements. The cryo-TEM images of 4x7 show a similar picture, however, the worm-like micelles at low pH appear shorter (Figure 46). Interestingly, the image taken of the sample at pH 5.9 very nicely shows a co-existence of spherical and worm-like micelles.

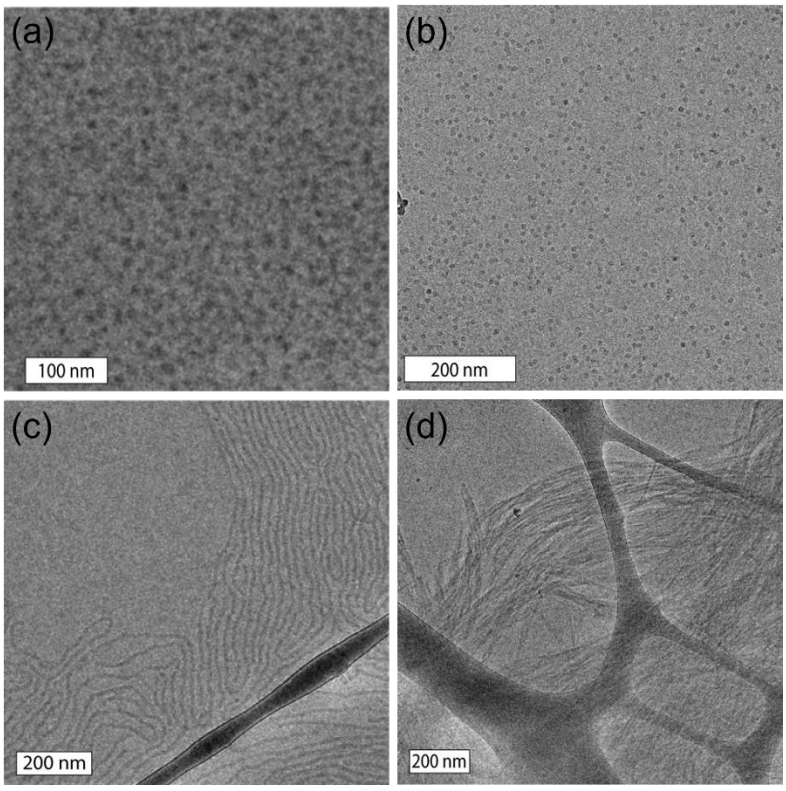

Figure 45. Cryo-TEM images of IDPA 2x12 at different pH. The images show the existence of spherical micelles at pH 6.5 and 6 (a and b) and elongated worm-like micelles at pH 5.1 and 3.2 (c and d).

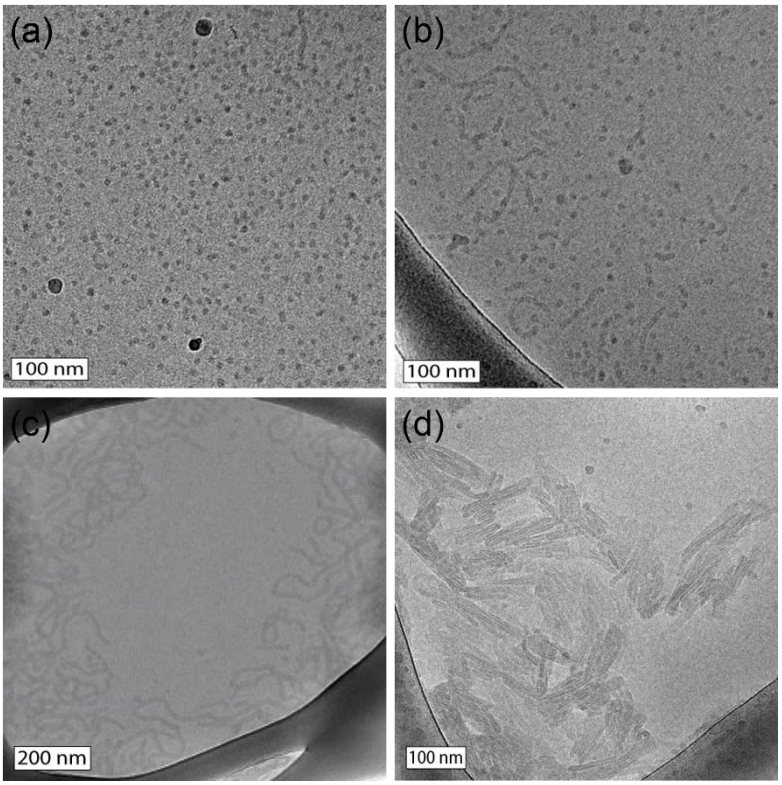

Figure 46. Cryo-TEM images of IDPA 4x7 at different pH. The images show the existence of spherical micelles at pH 6.5 (a), a coexistence of spheres and worm-like micelles at pH 5.9 (b) and worm-like micelles at pH 4.6 and 3 (c and d).

3.2.4 Modeling the phase-transition

In this section I will present a model for the observed spherical-to-cylindrical micelle phase-transition seen in our system, adapted from earlier work on a similar system of self-assembling amphiphiles with some charge density of the headgroup region[97].

First, in Section 3.2.4.1, we will discuss the free-energy function, show a schematic representation of the system that introduces the parameters used in the calculations, and lay out the general procedure for computing the different terms in the free-energy. In Section 3.2.4.2, I will detail the calculations I performed for our system. Finally, in Section 3.2.4.3, I will discuss predictions of the model and show experimental results.

The work on the model was done under the guidance of Prof. Michael Kozlov from the Sackler School of Medicine, Tel Aviv University.

3.2.4.1 Free-energy

The model's free-energy has two terms, representing the competition between the electrostatic free-energy, $\Delta F_E(Q)$, associated with the charge density of the peptides in headgroup region, and bending energy, ΔF_B, due to deviations from the intrinsic curvature of the amphiphiles. The

former depends on the peptide's charge, Q, which in turn depends on pH, and the latter is treated as a constant energetic penalty for having a curvature different from the intrinsic curvature. The free-energy is then:

$$\Delta F(Q) = \Delta F_E(Q) + \Delta F_B \tag{26}$$

To compute the different terms of the free-energy, we follow the procedure performed in Ref. 97, adapted to fit our system. Figure 47 shows a schematic representation of the cross section of the spherical and cylindrical micelles, assembled by the IDPAs. The figure also details the parameters used for the model, namely, the radius of hydrophobic core R, width of peptide shell δ, charging length ξ (used for integration), charge density ρ, Debye screening length in the shell and outside, λ_s and λ_o respectively, the dielectric constants in the core, shell and outside, ϵ_c, ϵ_s and ϵ_o respectively, and the electric potential ϕ, which we are required to solve.

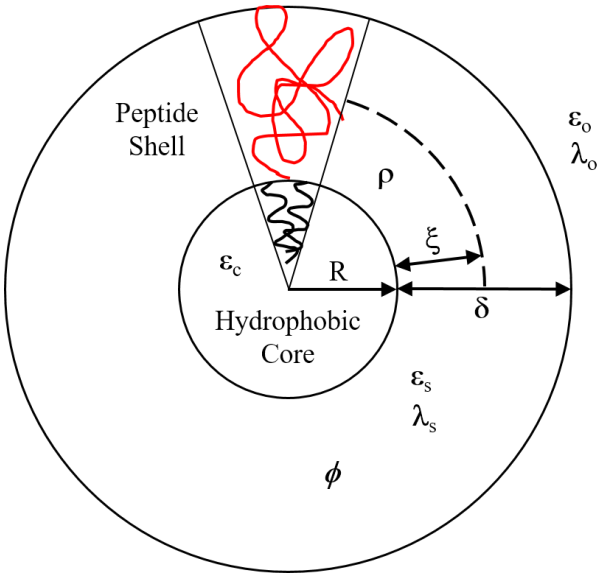

Figure 47. Schematic representation of a self-assembled spherical micelle of IDPAs.

To calculate the electrostatic free-energy, we perform a step-by-step charging process of concentric layers of thickness $d\xi$, and charge per layer $\rho(\xi)\, A(\xi)\, d\xi$. The electrostatic free-energy is given by:

$$F_E = \int_0^{\delta} \phi(\xi)\, \rho(\xi)\, A(\xi)\, d\xi \tag{27}$$

Integration can be performed only if the electrostatic potential for the system is known. The potential is found by solving the Poisson-Boltzmann equations in the three regions (the core, shell and outside):

$$\nabla^2\phi(r) = \begin{cases} 0 & r < R \\ \lambda_s^{-2}\phi - \dfrac{\rho}{\epsilon_s} & R < r < R + \xi \\ \lambda_o^{-2}\phi & R + \xi < r \end{cases} \tag{28}$$

under the following boundary conditions:

$$\begin{gathered} \phi_c(0) = \text{const}\,; \qquad \phi_c(R) = \phi_s(R)\,; \qquad \epsilon_c \frac{\partial \phi_c}{\partial r}(R) = \epsilon_s \frac{\partial \phi_s}{\partial r}(R) \\ \phi_o(\infty) = 0\,; \qquad \phi_s(R+\xi) = \phi_o(R+\xi)\,; \quad \epsilon_s \frac{\partial \phi_s}{\partial r}(R+\xi) = \epsilon_o \frac{\partial \phi_o}{\partial r}(R+\xi) \end{gathered} \tag{29}$$

To complete the calculation the values of R, δ and the aggregation number must be known, which can be extracted from the form factor modeling (Section 3.2.3.2.3). The charge density can then be calculated using the charge-pH curve (Figure 35).

The bending energy is modelled by[98]:

$$F_B = \frac{1}{2}\, a\, \kappa\, (J - J_i)^2 \tag{30}$$

where a is the area per monomer, κ is the bending modulus, J is the mean curvature and J_i is the intrinsic curvature.

3.2.4.2 Computing the free-energy[‡]

3.2.4.2.1 Electrostatic free-energy

To compute the electrostatic free-energy, one must first solve the Poisson-Boltzmann equation posed by the system, and find the potential in the shell, $\phi_s(r)$. To accomplish this, I used Wolfram Mathematica, formulating the problem and the relevant boundary conditions, under the relevant coordinate system (spherical/cylindrical). It should be noted that the correct functions must be used to solve the equation in the relevant coordinates (e.g., modified Bessel functions in the case of cylindrical coordinates). The result is ϕ_s in terms of ρ, R, λ_s, λ_o, ϵ_o, ϵ_s, and ξ the integration coordinate.

At this point, I would like to mention the assumptions I make for the proceeding calculations. I will discuss the validity of these assumptions and how they affect the calculations and predictions of the model in Section 4.2:

1. The dielectric constant inside the headgroup shell is the same as outside, $\epsilon_s = \epsilon_o$, which means that l_B will be the same in both regions.
2. Using the first assumption, and assuming the salt concentration in the solution outside is the same as inside the headgroup region, we set $\lambda_s = \lambda_o$.

[‡] All MATLAB and Mathematica calculations files are available at: https://www.becklab.sites.tau.ac.il/

3. The radius of the hydrophobic core, R, and the width of the peptide shell, δ, are fixed between spheres and cylinders.
4. The area per molecule is fixed between spheres and cylinders.
5. The charge density, ρ, is uniform over the width of the shell, hence it does not depend on ξ.

Under these assumptions, we can now calculate the following:

Area per molecule:

$$A_m^s = \frac{4\pi R^2}{N_m}$$

where N_m is the number of molecules, calculated in Section 3.2.3.2.3.

Volume per molecule in a sphere:

$$V_m^s = A_m^s \delta \left(1 + \frac{\delta}{R} + \frac{\delta^2}{3R^2}\right)$$

Volume per molecule in a cylinder:

$$V_m^c = A_m^s \delta \left(1 + \frac{\delta}{2R}\right)$$

The corresponding charge densities:

$$\rho_s = \frac{Q}{V_m^s} \; ; \; \rho_c = \frac{Q}{V_m^c}$$

Using the potential and charge density, we can now calculate the electrostatic free-energy using Eq. (27) for a specified salt concentration in solution.

3.2.4.2.2 Elastic free-energy

Computing the contribution to the total free-energy due to bending is straightforward for a given intrinsic curvature and bending modulus. However, since we have no experimental input for the values of these variables for our system (they are essentially fitting parameters), we can treat the difference in elastic free-energy in Eq. (26), $\Delta F_B = \frac{1}{2}\frac{\kappa a}{R}\left(\frac{3}{R} - 2J_i\right)$, as a single constant and find phase boundaries for different values of ΔF_B (lines of $\Delta F = 0$). The value of this constant is determined by using a combination of physically relevant values for the intrinsic curvature and bending rigidity. In order for the model to produce a phase-transition the intrinsic curvature, J_i, must be smaller than $\frac{3}{2R}$ (the midpoint between the curvature of a cylinder and a

sphere). A reasonable value for the bending modulus will be between 10 and 100 k_BT, based on values of widely studied amphiphiles[98].

3.2.4.3 Results and predictions

Based on the calculations described above, we can now produce a pH vs. salt concentration phase diagram and plot the phase boundary for different values of ΔF_B. This means that in experiments where we set the pH and salt concentration, we can determine the phase and set constraints on the other fitting parameters, which are difficult to directly measure.

Figure 48 shows the calculated phase diagram and boundaries for different values of ΔF_B between 0.5 and 6 k_BT using the values for R, δ and N_m from Section 3.2.3.2.3.

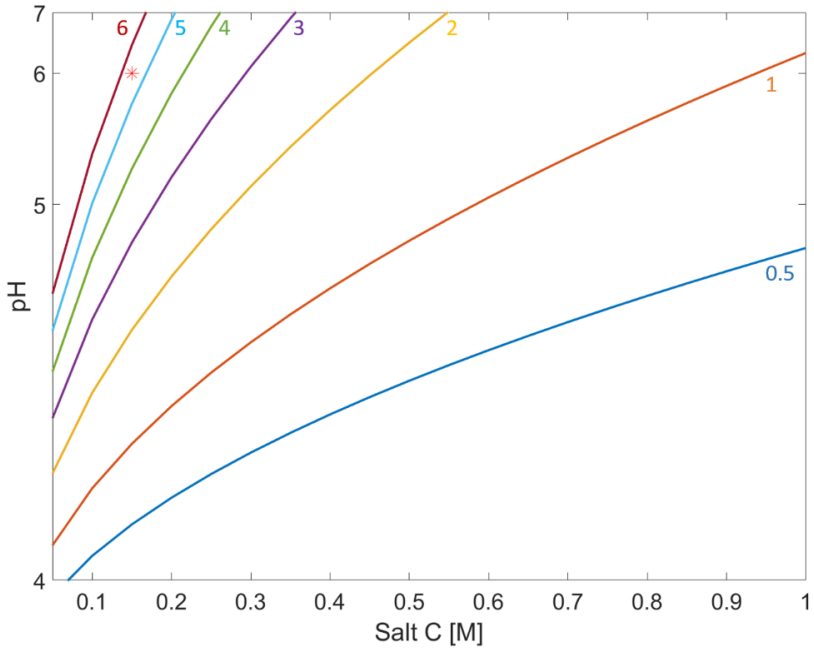

Figure 48. pH – salt concentration phase diagram solved for the system parameters given in Section 3.2.3.2.3. Plotted lines are phase boundaries for different values of ΔF_B in k_BT (colored values). Red asterisk represents the transition point suggested by the turbidity measurements.

The model can also provide a prediction regarding the phase behavior of amphiphiles with different tail lengths. Since the bending rigidity of membranes increases with amphiphile tail length[98,99], longer tailed amphiphiles should have their transition point pushed into higher pH. This is because a higher charge density (at higher pH) is compensated by a larger elastic energy penalty for spheres. Preliminary results on similar amphiphiles, using the same IDP as a headgroup but with different tail groups, indeed show an increase in the transition pH with tail length (Figure 49).

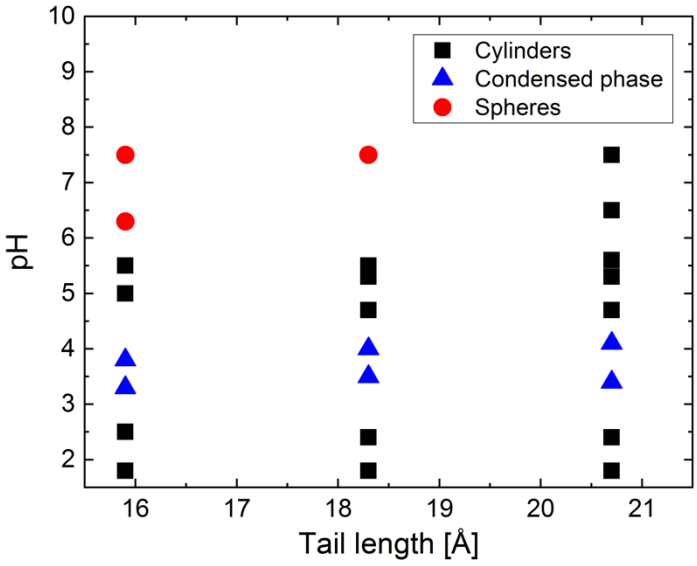

Figure 49. Phase diagram of amphiphiles, similar to 2x12, with the same IDP as a headgroup, but with varying lengths of their tails. The sphere-to-cylinder transition is pushed to higher pH with increasing tail length. Salt concentration of 100 mM was used.

3.2.5 Handshake analysis

Another possible explanation to the observed phase-transition takes into consideration the previously discussed model, which is a non-specific model, and adds a term to the free-energy which depends on the specific sequence of amino acids,

$$\Delta F(Q) = \Delta F_E(Q) + \Delta F_B + \Delta F_{HS}\,, \tag{31}$$

where ΔF_{HS} stands for a handshake interaction.

It is a specific electrostatic interaction between neighboring polyampholytes, due to the distribution of charges along the peptide. Specific relative conformations of neighboring peptides can result in an attractive interaction.

We qualitatively model this using the "Handshake analysis", previously described in Refs. 89,100. This analysis generates a heat-map of electrostatic interaction between different segments of interacting peptides, revealing "attractive conformations". The calculation of electrostatically interacting segments is performed by setting the peptide persistence length (PL), which determines the segment size (w amino acids are in contact in each segment), and the number of nearest neighbors (NN) that interact within that segment (each amino acid interacts with $2m + 1$ amino acids from the opposite segment)

$$\Delta E(n_1, n_2) = k_e \sum_{i=-w/2}^{w/2} \sum_{j=-m}^{m} \frac{eZ_1(n_1+i)eZ_2(n_2+i-j)}{|r_1(n_1+i) - r_2(n_2+i-j)|}. \quad (32)$$

The outcome of the analysis is a prediction regarding the possibility of a preferred conformation of attractively interacting peptides, as well as an approximation of the strength of interaction. Figure 50 and Figure 51 show the results of the analysis for two different sets of PL and NN.

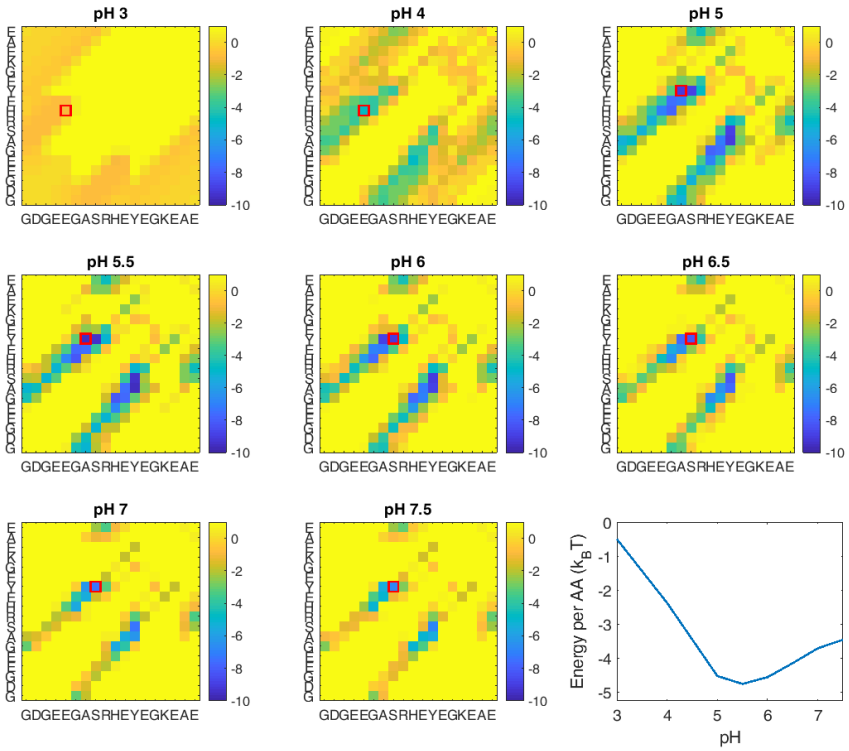

Figure 50. Handshake analysis heat-maps, for PL = 3 and NN = 3, showing the preferred attractive sliding-conformations as a function of pH. The color bar indicates the interaction strength in k_BT_{300K}. The bottom right graph shows our approximation of the strength of interaction at each pH, chosen to be the strongest point of attractive interaction (marked in red on the heat-maps).

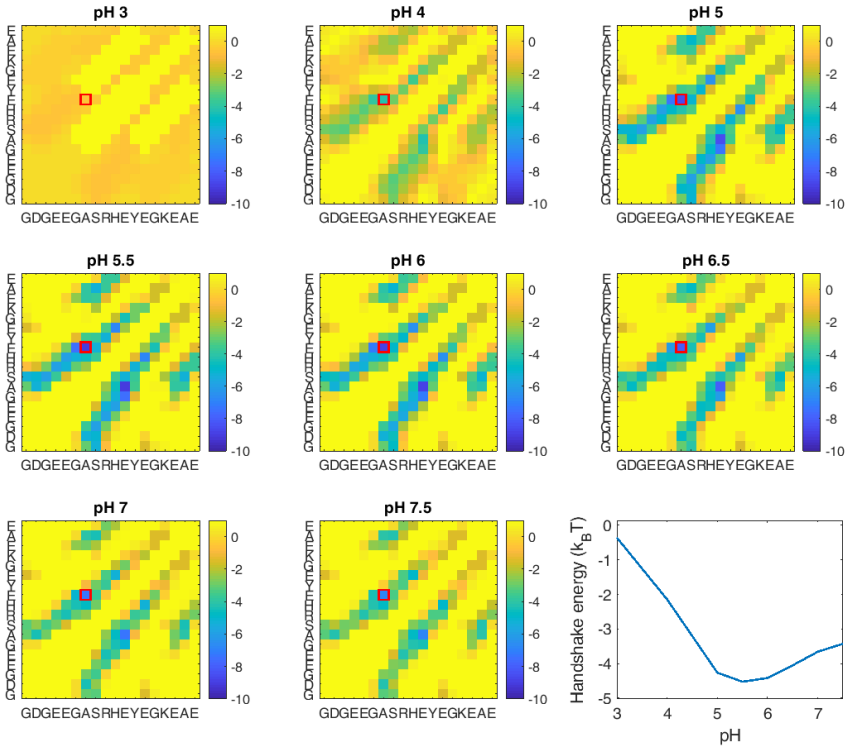

Figure 51. Handshake analysis heat-maps, for PL = 2 and NN = 1, showing the preferred attractive sliding-conformations as a function of pH. The color bar indicates the interaction strength in k_BT_{300K}. The bottom right graph shows our approximation of the strength of interaction at each pH, chosen to be the strongest point of attractive interaction (marked in red on the heat-maps).

The diagonal lines that increase in strength from pH 10 to 5.5 (dark color diagonal line) are a specific shifted conformation of adjacent peptides that is favorable. In this case, a shift of about 5 amino acids produces attractive interaction between parallel peptides, and the strength of the interaction is approximated by the strongest contact point (darkest square on the diagonal). Using these values, we can then approximate the dependence of the handshake interaction on pH (bottom right panel of Figure 50 and Figure 51). Mapping this dependence is useful for assessing the contribution of the conformation specific interaction to the overall interaction leading to the phase-transition, at least semi-quantitatively.

3.2.5.1 Sequence variants

When considering the sensitivity of the phase to pH, and more specifically, the phase-transition being located somewhere between pH 4 and 6, a possible explanation can be the charging state of the Histidine residue. Histidine is the only amino acid with a side chain group that gets protonated in this pH range.

We used the handshake analysis tool to design slightly modified headgroup sequences and predict their behavior of interaction. Two variants of the original sequence were produced: “no-His” – replacing the Histidine at position 10 by a Glycine, and “Switch” – swapping the Glutamic Acid at position 4 with the Arginine at position 9. It is important to note that the total (and net) charge of no-His has changed, as it will no longer have an additional positive charge below pH 6. Switch on the other hand retains the same total (and net) charge, but has a different distribution of charges along the sequence.

The handshake analysis also predicts a weaker interaction for the same conformation chosen for the original sequence (Figure 52). The Switch variation was predicted by the analysis to abolish the favorable interaction of the conformation seen in the original (Figure 53).

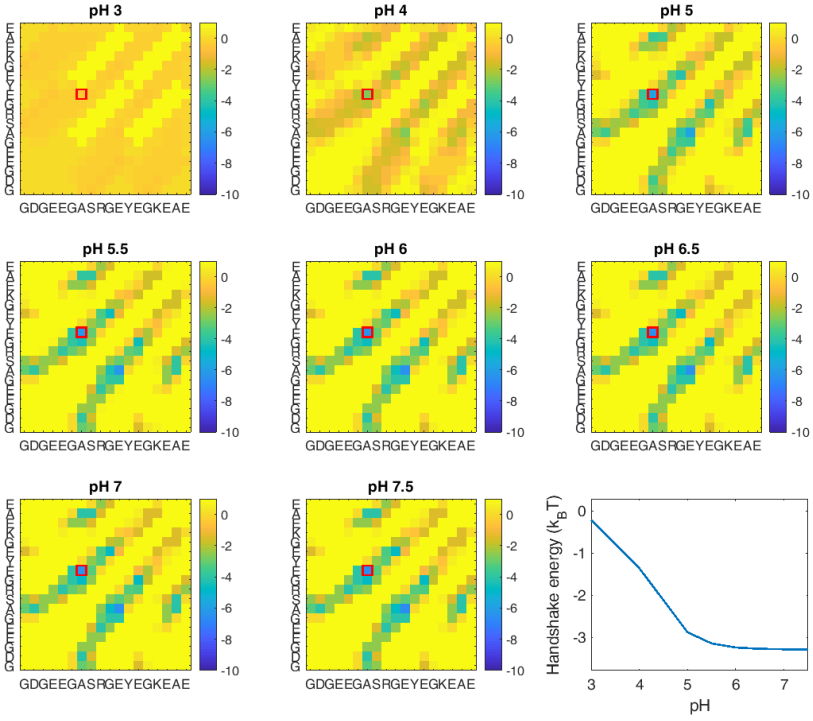

Figure 52. The handshake analysis, with PL = 2 and NN = 1, for the no-His sequence. The interaction energy is weaker than for the original sequence, and there is no longer a minimum around pH 5.5. The color bar indicates the interaction strength in k_BT_{300K}. The bottom right graph shows our approximation of the strength of interaction at each pH, chosen to be the strongest point of attractive interaction (marked in red on the heat-maps).

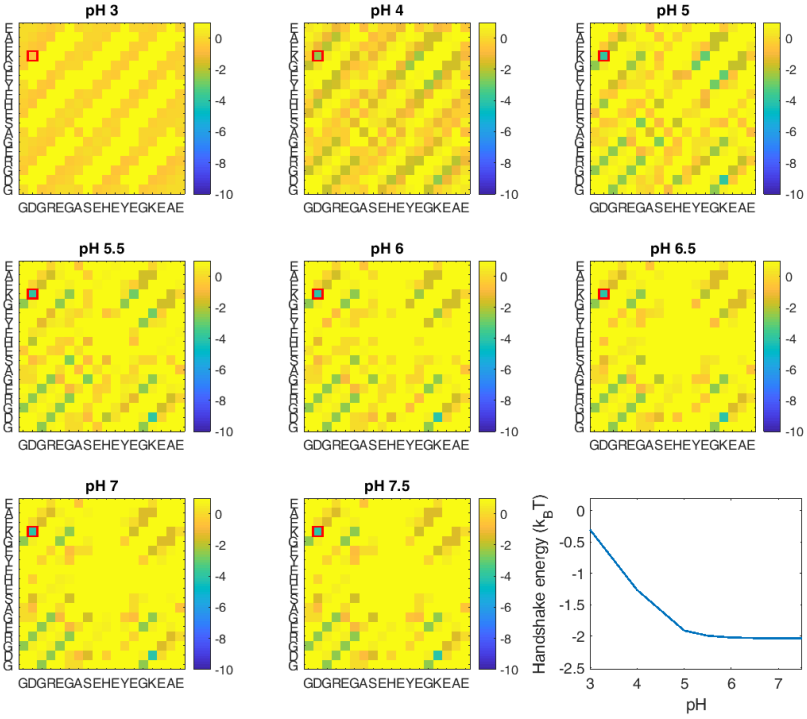

Figure 53. The handshake analysis, with PL = 2 and NN = 1, for the Switch sequence. The switching has abolished the attractive conformation from the original sequence. The color bar indicates the interaction strength in k_BT_{300K}. The bottom right graph shows our approximation of the strength of interaction at each pH, chosen to be the strongest point of attractive interaction (marked in red on the heat-maps).

Both of these variants are still considered highly disordered and are assigned the random coil conformation by the predictors used in Section 3.2.2.2 (Figure 54 and Figure 55).

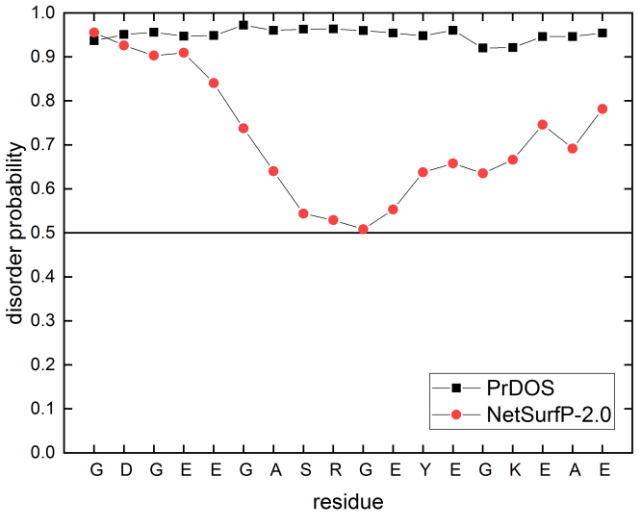

Figure 54. Results of software disorder predictions for the no-His sequence. The output of the PrDOS (black squares) and NetSurfP-2.0 (red circles), both showing a high probability for disorder of the peptide sequence.

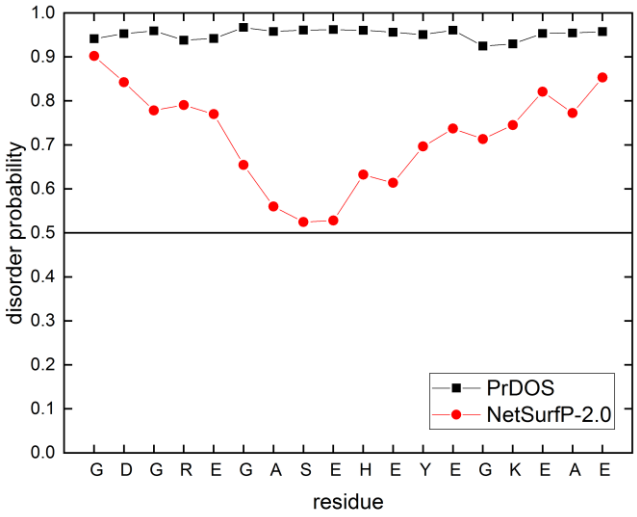

Figure 55. Results of software disorder predictions for the Switch sequence. The output of the PrDOS (black squares) and NetSurfP-2.0 (red circles), both showing a high probability for disorder of the peptide sequence.

3.2.5.2 Experimental results with sequence variants

To test our predictions and determine if specific interactions between the peptides in the assembly lead to complex aggregations at low pH, we performed SAXS measurements on the two headgroup variants at pH 3.

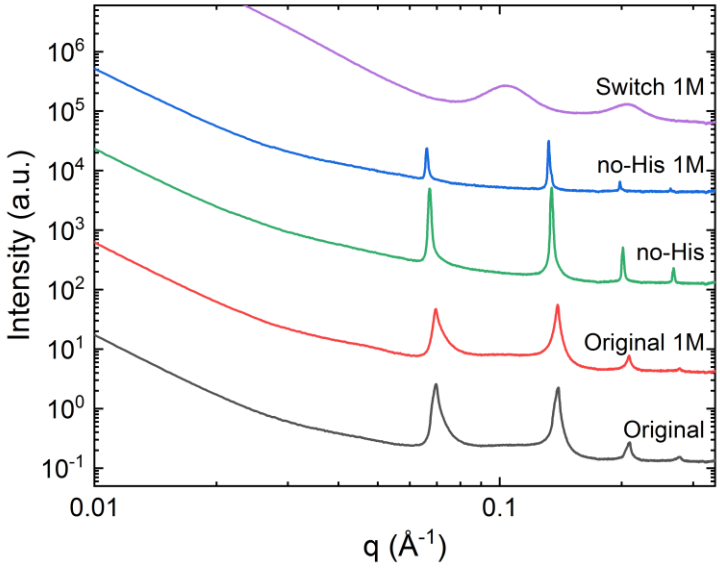

Figure 56. Comparison of SAXS measurements of 4x7 along with its no-His and Switch variants at pH 3, in either 150 mM salt or 1 M (labeled). The phase remains the same for no-His, while the Switch variant shows a pronounced weakening of the inter-micelle correlations.

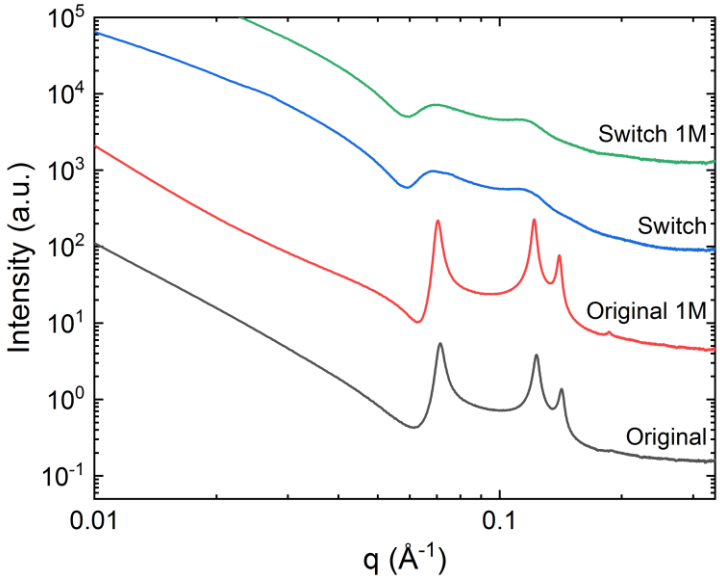

Figure 57. Comparison of SAXS measurements of 2x12 and its Switch variant at pH 3, in either 150 mM salt or 1 M (labeled). The small change in charge distribution, while maintaining total charge has a dramatic effect on the interaction of the worm-like micelles. The sharp structure factor peaks are replaced with wide and shallow peaks, indicating weaker correlations.

The results of the SAXS experiments show that replacing the Histidine with a Glycine served to strengthen the interaction between the worm-like micelles (Figure 56). However, slightly changing the order of the sequence (Switch varient), but maintaining the same net charge, can

lead to a significant weakening of the micelle-micelle interaction in the worm-like phase. This is demonstrated by the diminished structure factor scattering (Figure 56 and Figure 57).

Chapter 4 Discussion

4.1 Metastability of phospholipid membranes

4.1.1 Long-lived, cooperative metastability deviates from classical nucleation theory

Crystallization in lipid systems is categorized as a first-order phase-transition, and as such, it commonly occurs through the process of nucleation. We have shown that the basic theory to describe such a transition – classical nucleation theory – cannot properly capture the dynamics presented in this work. In contrast to the classical theory, which is described using short-range interactions, the cooperative nature of the dynamics suggests that long-range interactions are necessary to produce the observed delayed nucleation process.

Two works inspired the line of thought that resulted in the mechanism proposed in Section 3.1.5. The first is a study of a system displaying non-classical nucleation. Specifically, delayed nucleation was observed and studied theoretically in the paraelectric to ferroelectric phase-transition in $BaTiO_3$[52,53,101]. There, mediated by long-range elastic interactions, the metastability activation energy-barrier was modeled as time-dependent, which ultimately defined the delay time of the system. The delay time was measured to be six orders of magnitude larger than the expected timescale.

The second is a more recent study, which experimentally showed long-range inter-layer alignment of phase-separated intralayer domains across hundreds of lamellae, in multi-component supported lipid membranes[85]. The study proposed explanations for the alignment of phase-separated domains. The first explanation is that the height difference between the ordered and disordered domains can affect the organization of the layers, in favoring a specific morphology. The second proposes that a mismatch between the hydrogen-bonding networks hydrating the different headgroups leads to a surface tension between inter-layer domains.

This inter-layer alignment of phase-separated domains was theoretically addressed in a follow-up paper[86]. There, using a model of stacked 2D Ising spins to represent the stacked lipid membranes, they showed that the system forms a continuous columnar structure in equilibrium, for any finite interaction across adjacent layers.

In our model, the long-range interaction, the key ingredient for cooperativity, is manifested by the effective surface tension γ, which causes the suppression of crystallization of a single membrane in an MLV, and ultimately brings about the long-lived metastability. The coupling between domains in adjacent layers – à la Ref. 86 – needed to create a crystallization barrier in the perpendicular direction, was introduced as the last term in Eq. (15) (Section 3.1.5.3.1).

Essentially, the anisotropic effective surface tension σ must be met with a decrease in the intra-layer domain free-energy, associated with the liquid to solid transition, and an inter-layer coupling favoring similarly phased domains.

The model allows us to interpret our experimental results (Section 4.1.2), but it can possibly be used further by extending the mechanism to similar systems. The basic mechanism and arguments presented in Section 3.1.5 are not specific to phospholipids and should hold for any molecular system with the necessary properties, undergoing nucleation.

Generally, (1) the system must be organized in stacked two-dimensional layers, where (2) an effective surface tension of the stack, caused by a difference in curvature of the two phases, will suppress nucleation of a single layer in the stack (given $T < T_c^{(0)}$). (3) The layers' difference in curvature must be penalized, when transitioning to the new phase, in an intensive manner, and (4) there needs to be an attractive coupling of similarly phased domains in adjacent layers.

A system with this set of properties should, in principle, display a mechanism like the one discussed here.

4.1.2 Robust and reproducible metastability

The investigation of the metastability went well beyond the scope of a simple or pure system. The experimental results presented here show that despite changing system parameters, such as number of components or environmental properties, the metastability persisted in a surprisingly reproducible manner. I would like to point out a few of the key findings in the context of deviations from classical nucleation theory.

First, it is important to mention that at no point in the preparation of the samples was there any effort to homogenize the particles' sizes, as is common practice when studying lipid systems. Homogenization is usually performed to achieve a similar starting point of research. And yet, despite this heterogeneity of the sizes, the delay time was shown to be reproducible with a peak in the probability at a non-zero value (Figure 29).

However, in some sense, the preparation of samples with an uncontrolled size distribution of the lipid particles, which favors larger ones due to poor solubility of DLPE, played a crucial role in this study. According to our model, the size distribution and number of layers of the MLVs should be taken into consideration, since they can greatly affect the possibility of nucleation. The first requirement on the system that must be met for crystallization to commence is set by Eq. (14). If the number of layers in the MLV is smaller than n^*, the suppression of crystallization of a single membrane will not be lifted. Furthermore, the number

of layers must also exceed n_c, the critical number of layers for 3D crystallization, or a stable nucleus will not form (Eq. (22)). Finally, the size of the MLV cannot be too small as to violate the condition $\frac{r}{R} \ll 1$, or domains of size R_c might not be able to form.

Moreover, we hypothesis that the size distribution of the lipid particles should affect the dynamics of the metastability, namely, setting τ of the system. The larger the lipid particles, the greater the chance for crystallization to occur. Hence, the τ of the sample, which is comprised of many particles of different sizes, is dominated by the largest particles. This can possibly serve as an explanation to two experimental observations: the delay time increases with the amount of secondary lipid (Figure 17) and with consecutive phase-transitions (Figure 22).

In the former experiment, the addition of PG lipids could decrease the average size of the particles, which would lead to an increase in τ. The inclusion of PG lipids into the formulation of lipid particles has been shown to increase the stability and solubility of DLPE (Section 3.1.2.1), a necessary adjustment made for utilizing it as the main lipid component for small vesicles used in drug delivery systems. In the latter experiment, the average number of lamellae per particle dropped with each transition, seen as the decrease in the lamellar scattering intensity, in correlation with the prolongation of the delay time (Section 3.1.2.3).

The model provides another possible explanation to the increase of τ with the inclusion of the PG lipids. In classical heterogeneous nucleation, impurities are considered preferential nucleation sites due to a lower surface energy penalty compared to the homogeneous case. In our system, the inclusion of a secondary lipid not only served to delay crystallization but did so in a reproducible manner (Figure 17). This can be attributed to the increase of the compression and/or bending moduli of the L_α phase, and therefore also of γ, with increasing lipid chain length and increasing membrane charge. Such modifications, by increasing γ, should deepen the metastability.

Regardless of the change in system parameters in each experiment, e.g., changing the amount and/or type of secondary lipid, the concentration of salt in solution and their rate of crossing the membrane (ionophores), or performing thermal cycles, it seems the underlying mechanism remains the same. This implies a robust mechanism, which pre-determines the “clock” on the metastability lifetime. This notion of a long and predetermined timescale for a phenomenon, which classically is unpredictable and uncontrollable, has interesting ramifications. It allows one to access the complex dynamics, which would otherwise be a difficult obstacle, and it can benefit the design of applications wishing to harness it.

4.2 Intrinsically disordered peptide amphiphiles

4.2.1 Order from disorder, and rational design

The paradigm of the "structure-function" relationship in modern biology has shifted over the past three decades towards a split into a boarder range of protein classes[25]. The ever-expanding class of IDPs has become increasingly important and diverse in the challenges it presents[102,103]. Studies of IDPs have shown that the role of a protein isn't anchored to a single folding state but can span an ensemble of conformations[27,29]. Depending on the environment, IDPs can dynamically transition between folding states, facilitating the desired functionality of the specific setting. This means that IDPs can fulfill several functional rolls, in contrast to proteins adhering to the classic structural-biology dogma.

Single molecule characterization techniques for proteins, including SAXS, greatly benefit from having the information of the single molecule presented directly, decoupled from an interfering environment. However, IDPs present a challenge in this case as well. One on hand, the weaker interactions involved in the folding of IDPs enable the desired transitions between conformations, but on the other, they hinder our ability to accurately characterize these transient states.

The main intention of this work was to construct a platform on which the study of IDPs and their interactions will be made easier through self-assembly. This method allows for the simultaneous measurement of many molecules, interacting in a manner dictated by the assembly conditions. This platform also enables for "in-situ" modifications of the IDPs and measurement of the resulting changes made to the assembly.

The results of the experiments presented in Section 3.2 showcase, above all else, one important notion regarding IDPAs. Although their headgroups are weakly interacting and disordered by nature, which is generally associated with transient behavior, their self-assembly is remarkably "ordered". The self-assembly process of the IDPAs into spherical micelles produces a narrow distribution of micelle sizes, evident by the strong form-factor signal (Figure 43). Moreover, in the low pH aggregating phase, the IDPAs self-assemble into strongly interacting cylindrical elongated worm-like micelles, comprising crystalline-like phases (e.g., hexagonal packing) with pronounced Bragg peaks (Figure 41).

In the process of designing amphiphiles for functional self-assembling systems there are several advantages of using synthetic disordered peptides over biologically derived, ordered proteins. First and foremost, the number of biological proteins to draw from is significantly limited when compared to synthetic IDPs. Although there are many known proteins (e.g., human genome encodes for tens of thousands of proteins), the possibilities for constructing functional IDPs is,

for all intents and purposes, unlimited. Where proteins are specific sequences designed for a specific application, synthetic IDPs can be rationally designed for any task, including mimicking biological ones.

Second, and this point ties in with the first, because we are not restricted to a specific sequence, we can include any segment of amino-acids into the peptide, to allow for additional modifications to the sequence. For example, one can insert a cleavage-site in-between a block co-polymer of IDPs, designed to fulfill some biological rule, which allows for *in situ* modifications.

Third, the weaker interactions that govern IDP interactions, and grant them their dynamic behavior, are flexible tools for designing sensitive systems that can respond to small changes of the environment. However, this does not take away from their ability to form robust structures needed for applications.

Last, one of the major challenges when designing a platform that is intended for biological use in-vivo is bio-toxicity. Although synthetic peptides can have harmful biological effects, the fact that they are comprised of natural amino-acids serves as a good starting point, compared to non-biological building blocks.

4.2.2 Non-specific vs. specific interactions

A major challenge when designing synthetic IDPAs, for a specific functional purpose, is to be able to navigate a desired energetic landscape. When modeling their interactions and phase-transitions, it is important to understand whether the dominant interactions are non-specific, e.g., based on the total charge-density, or specific, e.g., conformational-based interactions.

The model presented in Section 3.2.4 is a generic model for a spherical-to-cylindrical micelle phase-transition (the model is agnostic to the details of the charged headgroup, aside from the charge distribution). The model describes the free-energy balance between the energy associated with the charge-density of the headgroup region and the energetic price paid for inducing a curvature that deviates from the intrinsic one. Essentially, the phase-transition is induced by a change in pH, which causes a change in the net charge of the headgroups. When the net charge is reduced (near the pI), compression of the headgroup region is facilitated by the decrease in bending energy to a cylindrical morphology, with a denser headgroup region.

For the free-energy to be computed, a few system parameters must be input from external analysis. In this case, the number of monomers, radius of hydrophobic core and thickness of headgroup region were all supplied by the fit of the core-shell form-factor to the spherical

micelle scattering (Section 3.2.3.2.3). In addition, several assumptions were made that can affect the outcome of the model.

The most significant assumption I made was to fix the radius of the hydrophobic core, R, and the width of the peptide shell, δ, between the sphere and cylinder. This assumption was made because it is difficult to extract these values for the cylindrical phase, due to the mixing of the form-factor and strong structure factor scattering in experiments. One can isolate and model the worm-like micelle form-factor by modeling the structure factor and dividing it from the total intensity. This should provide better estimates for the values of R and δ.

Another important assumption regards the shape of the charge density distribution in the headgroup region. For the calculations and results shown in Section 3.2.4 I took the simplest case of a uniform distribution. The distribution can be modeled in different ways to more accurately reflect the charge distribution along the peptide and the spatial conformation the peptide adopts. However, since we are dealing with a highly charged IDP, a uniform distribution is a reasonable assumption.

The last assumption I wish to discuss regards the screening length in and out of the headgroup shell. There is a longstanding challenge in assessing local ion concentrations and pH[104–106]. Since it is difficult to measure the local values of these quantities, we generally assume the bulk values apply to the system entirely, while in truth the local values may differ substantially, leading to erroneous results and conclusion. However, since we lack detailed information regarding the actual concentrations of ions in the headgroup region or ion adsorption to the peptide, I set the concentrations to be equal.

4.2.2.1 Handshake analysis and experimental results

To take into account the details of the distribution of charges along the peptide we added a specific interaction term to the free-energy (Eq. (31)), describing electrostatically interacting amino-acids along two parallel and offset peptides. The relative conformation and strength of interaction can be calculated using the handshake analysis, which produces a map of the interactions depending on the relative offset. This handshake analysis was performed similarly to previous works that modelled interactions between parallel and anti-parallel polyampholytic IDPs[89,100].

The utility of the handshake analysis was three-fold in our case. First, it served to give us an initial assessment of whether specific favorable interaction conformations exists within the context of our peptide sequence (Figure 50 and Figure 51). Later, it served as a prediction tool for the rational design of modifications to the original sequence, to either enhance the interaction or abolish it (Figure 52 and Figure 53). The two proposed peptide variants we

produced and measured, no-His and Switch, showcase the impact a small change to the sequence has on the macroscopic organization of the amphiphiles (Figure 56 and Figure 57).

The no-His sequence was designed with the intent of removing the hypothetical pH dependence the peptide has, regarding changes to charge with pH, around pH 6. Since the original IDPAs seemed to transition in the vicinity of pH 6, the removal of the only Histidine could make the system insensitive to changes of the pH around this value. The interaction map produced for this variant, indeed shows no change of the overall interaction strength close to pH 6 (Figure 52). Experiments showed that the aggregating phase at low pH remained the same (with stronger correlations – Figure 56), but experiments conducted on samples at high pH seemed to show scattering pertaining to spherical micelles (this data is not shown since the samples were prepared erroneously before the preparation protocol used in Section 2.1.4.2).

While the no-His variant does not conserve the original sequence's charge dependence on pH (we replaced a protonatable amino-acid with a neutral one), the Switch variant was chosen because it does. The rationale here was to make a small switch in the order of the sequence, and by doing so, greatly weaken the attractive conformation seen in the original sequence (Figure 53). The experimental results show that indeed this small change had a significant effect on the inter-micelle interactions, and as a result, the aggregation phase was dramatically changed.

While differing in nature, both variants are a testament to the usefulness of this simple analysis. Although it is a very simplistic model for electrostatically interacting polyampholytes, and should be used qualitatively, it can guide further progress in the design of useful IDPAs.

The third use we made of the handshake analysis was to get a rough quantitative estimate of the strength of the interaction between the peptides for the model. The interaction map is constructed in such a way that each amino-acid pair's value is the "weighted interaction", which depends on the nearest-neighbors and the persistence length of the segment in the sequence (for an in-depth explanation on the analysis please refer to Ref. 89 and its supplementary information). The value we took to estimate the interaction was the pair with the strongest interaction (most negative value, marked in the figures and plotted, e.g., Figure 50). However, the contribution of this specific interaction is manifested as a constant in the free-energy, effectively used to shift the transition point along the pH axis. Since it is taken as a constant, it cannot change the shape of the phase-boundary, which proved to be problematic when trying to fit the experimental data.

Since the model's predictions rely on an accurate value of the charging state of the peptide, according to the pH, any deviations of the actual state of the peptide from the "theoretical" one will result in a wrong prediction. One should keep this in mind when trying to find the exact phase boundary line.

4.2.3 Challenges in production and sample preparation

The production of the IDPAs was done in collaboration with Ms. Merav Segal Asher and Prof. Roey Amir, head of the Amir research group at the School of Chemistry, Tel Aviv University, and the Blavatnik Center for Drug Discovery (BCDD), Tel Aviv University.

The initial design of the tail groups of the IDPAs was inspired by previous works by the Amir research group on dendritic amphiphiles that form functional micelles[107–109]. This dendritic chemical architecture was used to create two variants with 2 or 4 hydrocarbon tails. A connective ring was used to conjugate the IDP headgroup to the hydrocarbon tails (Figure 34). The production of the hydrophobic part (the connective ring conjugated to the tails) was performed at the Amir lab, and the resulting compound was delivered to the BCDD for further conjugation to the IDP, and purification. This two-step process proved to be challenging due to the partial miscibility of the resulting IDPA in both the organic and inorganic phases. Now, options of single-step production of the amphiphiles are explored, which will facilitate the production and yield.

Further complications arose when it became apparent that the IDPAs produced in this process, and specifically the product of the purification process, were in very acidic conditions. This made it difficult to provide a reproducible starting point for the experiments, which requires us to accurately determine the equilibrium phase at each pH. Two possible preparatory steps were proposed to treat the samples before measurements.

The first is to fluidize the IDPA powder in water (Milli-Q), then titrate with NaOH to a pH where the solution becomes more homogenous (preferably a pH where the IDPAs are soluble in water). By doing so, we hope to counter the acidic environment of the amphiphiles. After titration, we can combine with a 2X buffer of choice to reach the desired pH.

The second option is to dialyze out the excess protons, responsible for the acidic pH, using a buffer at the target pH. This method has the advantage of not introducing extra ions (via titration), and is a slower process, which should clean the environment of the acidity, instead of countering it, like in the first option. However, there is the risk of material loss to the dialysis membrane.

The samples used to produce the results shown in this work were prepared using the first method. Since then, it has become clear that this process of counteracting the acidity using titration may not be the best option, especially for producing stable conditions near the phase-transition point. This became evident when attempting to reproduce the turbidity measurements, and "similarly" prepared samples displayed differences in their turbidity curves,

especially in the sensitive region between the phases (either a coexistence region, or a specific transition point).

In any case, reproducibility is of paramount importance in scientific work, which means production and preparation of samples should be front and center before proceeding with experiments.

Chapter 5 Future work

This final chapter summarizes the open questions I found to be interesting for further understanding the phenomena discussed in this work.

5.1 Metastability of phospholipid membranes

5.1.1 Nucleation dynamics (theory)

The model discussed in Section 3.1.5 details the mechanism necessary for producing the observed delay in cooperative crystallization. However, currently it does not include a microscale description of the dynamical process the system must undergo to complete crystallization. The events that occur, their sequence and associated timescales, e.g. the collision of membranes that form a cohesive stack and the growth dynamics in 2D, are necessary to complete the picture.

5.1.2 Controlling particle size to set τ

As discussed in Section 4.1.2, the model suggests that the delay time, τ, should depend on the distribution of particles sizes in the system. This can be tested by creating samples with controlled particle size distributions. To this end, several techniques such as extrusion, sonication or micro-fluidic devices are widely used to limit the sizes of lipid particles.

5.1.3 Crystal growth, the effect of pellet size and boundary conditions

One of the biggest open questions concerns the role τ^*, the transition period, and τ_B, the build-up time. While τ has been associated with the metastability of a single MLV, experiments indicate that τ^* and τ_B are somehow tied to the dynamics of the whole system. Figure 24 demonstrates that the transition occurs at different times at different locations (the difference in τ can be as large as 100 hours), yet the onset of the structural change in samples with large pellets, marked by τ_B, is macroscopically coordinated over millimeters. This length-scale is orders of magnitude larger than any microscopic length-scale associated with lipid self-assembly.

The samples used for these experiments differed from samples used in most other experiments by the size of the lipid pellet. A bigger pellet facilitates probing spatially distant regions in a sample, which, in turn, can reveal whether there is some sort of information flow prior to crystallization (as the build-up time suggests). Experimenting with different pellet sizes will not only help understand if there are prior events happening, but also separate regions at the

boundary (both water-lipid interface and lipid-glass) and study the effects of the boundaries on the dynamics.

5.1.4 Correlating X-ray and calorimetric measurements

The calorimetry experiments in Section 3.1.2.4 were very important because they revealed information on the thermodynamic process during the metastability. The timescales are comparable to the X-ray scattering experiments, yet, it is still unclear how the thermodynamic process and structural process (seen in scattering) are correlated. It would be informative to perform an experiment to measure both simultaneously and correlate both in time.

5.1.5 Pre-determined cargo release

The design of controlled cargo hold-and-release systems is one of the challenges of biomedical applications. Since DLPE has already been utilized as a component in such systems, harnessing the metastability to perform such a task could be greatly beneficial. The effects of a relevant cargo on the metastability were demonstrated and discussed to a small extent in Section 3.1.2.7. This, however, should only serve as a starting point for a much deeper investigation into the utility and applicability of the phenomenon in such tasks.

5.2 Intrinsically disordered peptide amphiphiles

5.2.1 Extending the theory

As discussed in Section 4.2.2, the model shown in Section 3.2.4 has been studied using simplifying assumptions. To better understand if the model is sufficient in describing the observed phase-transition more information must be collected. Modeling the worm-like micelle form-factor and extracting the spatial features will allow for a better assessment of the model's capabilities. The model can also be extended by allowing for non-trivial charge density distributions to be input, which should provide more accurate quantitative results.

5.2.2 Temperature dependence

When investigating the phase-behavior of an amphiphilic system, temperature almost always plays an important role as a thermodynamic variable. By varying the temperature, the current system can expose more interesting, and perhaps useful, phase-transitions. Temperature can also be considered as an additional variable for the theoretical model, setting additional constraints.

References

1. Israelachvili, J. *Intermolecular and Surface Forces*. *Intermolecular and Surface Forces* (Elsevier, 2011).

2. Pabst, G., Kučerka, N., Nieh, M.-P. & Katsaras, J. *Liposomes, Lipid Bilayers and Model Membranes*. *CRC Press* (CRC Press, 2014).

3. Wikipedia article 'Self-assembly'. https://en.wikipedia.org/wiki/Self-assembly.

4. Nagarajan, R. Molecular packing parameter and surfactant self-assembly: The neglected role of the surfactant tail. *Langmuir* **18**, 31–38 (2002).

5. Shearman, G. C., Ces, O., Templer, R. H. & Seddon, J. M. Inverse lyotropic phases of lipids and membrane curvature. *J. Phys. Condens. Matter* **18**, (2006).

6. Alberts, B. *Molecular Biology of the Cell*. (Garland Science, 2017).

7. Lumen Learning - Introduction to Chemistry. https://courses.lumenlearning.com/introchem/chapter/phospholipids/.

8. Pattni, B. S., Chupin, V. V. & Torchilin, V. P. New Developments in Liposomal Drug Delivery. *Chem. Rev.* **115**, 10938–10966 (2015).

9. Luzzati, V. & Husson, F. The structure of the liquid-crystalline phases of lipid-water systems. *J. Cell Biol.* **12**, 207–219 (1962).

10. Kučerka, N., Nagle, J. F., Sachs, J. N., Feller, S. E., Pencer, J., Jackson, A. & Katsaras, J. Lipid Bilayer Structure Determined by the Simultaneous Analysis of Neutron and X-Ray Scattering Data. *Biophys. J.* **95**, 2356–2367 (2008).

11. Laggner, P. & Kriechbaum, M. Phospholipid phase transitions: kinetics and structural mechanisms. *Chem. Phys. Lipids* **57**, 121–145 (1991).

12. de Gennes, P. G. & Prost, J. *The Physics of Liquid Crystals*. (Clarendon Press ; Oxford University Press, 1993).

13. Cui, H., Webber, M. J. & Stupp, S. I. Self-assembly of peptide amphiphiles: From molecules to nanostructures to biomaterials. *Biopolymers* **94**, 1–18 (2010).

14. Hartgerink, J. D., Beniash, E. & Stupp, S. I. Self-assembly and mineralization of peptide-amphiphile nanofibers. *Science.* **294**, 1684–1688 (2001).

15. Chin, S. M., Synatschke, C. V., Liu, S., Nap, R. J., Sather, N. A., Wang, Q., Álvarez, Z., Edelbrock, A. N., Fyrner, T., Palmer, L. C., Szleifer, I., Olvera De La Cruz, M. & Stupp, S. I. Covalent-supramolecular hybrid polymers as muscle-inspired anisotropic actuators. *Nat. Commun.* **9**, 1–11 (2018).

16. Hartgerink, J. D., Beniash, E. & Stupp, S. I. Peptide-amphiphile nanofibers: A versatile scaffold for the preparation of self-assembling materials. *Proc. Natl. Acad. Sci.* **99**, 5133–5138 (2002).

17. Silva, G. A., Czeisler, C., Niece, K. L., Beniash, E., Harrington, D. A., Kessler, J. A. & Stupp, S. I. Selective Differentiation of Neural Progenitor Cells by High-Epitope Density Nanofibers. *Science.* **303**, 1352–1355 (2004).

18. Peters, D., Kastantin, M., Kotamraju, V. R., Karmali, P. P., Gujraty, K., Tirrell, M. & Ruoslahti, E. Targeting atherosclerosis by using modular, multifunctional micelles. *Proc. Natl. Acad. Sci.* **106**, 9815–9819 (2009).

19. Acar, H., Samaeekia, R., Schnorenberg, M. R., Sasmal, D. K., Huang, J., Tirrell, M. V. & LaBelle, J. L. Cathepsin-Mediated Cleavage of Peptides from Peptide Amphiphiles Leads to Enhanced Intracellular Peptide Accumulation. *Bioconjug. Chem.* **28**, 2316–2326 (2017).

20. Bull, S. R., Guler, M. O., Bras, R. E., Meade, T. J. & Stupp, S. I. Self-assembled peptide amphiphile nanofibers conjugated to MRI contrast agents. *Nano Lett.* **5**, 1–4 (2005).

21. Tovar, J. D., Claussen, R. C. & Stupp, S. I. Probing the interior of peptide amphiphile supramolecular aggregates. *J. Am. Chem. Soc.* **127**, 7337–7345 (2005).

22. Paramonov, S. E., Jun, H. W. & Hartgerink, J. D. Self-assembly of peptide-amphiphile nanofibers: The roles of hydrogen bonding and amphiphilic packing. *J. Am. Chem. Soc.* **128**, 7291–7298 (2006).

23. Trent, A., Marullo, R., Lin, B., Black, M. & Tirrell, M. Structural properties of soluble peptide amphiphile micelles. *Soft Matter* **7**, 9572–9582 (2011).

24. Wikipedia article ‘Peptide Bond’. https://en.wikipedia.org/wiki/Peptide_bond.

25. Uversky, V. N., Gillespie, J. R. & Fink, A. L. Why are ‘natively unfolded’ proteins unstructured under physiologic conditions? *Proteins Struct. Funct. Genet.* **41**, 415–427 (2000).

26. Oates, M. E., Romero, P., Ishida, T., Ghalwash, M., Mizianty, M. J., Xue, B., Dosztányi, Z., Uversky, V. N., Obradovic, Z., Kurgan, L., Dunker, A. K. & Gough, J. D2P2: Database of disordered protein predictions. *Nucleic Acids Res.* **41**, 508–516 (2013).

27. Van Der Lee, R., Buljan, M., Lang, B., Weatheritt, R. J., Daughdrill, G. W., Dunker, A. K., Fuxreiter, M., Gough, J., Gsponer, J., Jones, D. T., Kim, P. M., Kriwacki, R. W., Oldfield, C. J., Pappu, R. V., Tompa, P., Uversky, V. N., Wright, P. E. & Babu, M. M. Classification of intrinsically disordered regions and proteins. *Chem. Rev.* **114**, 6589–6631 (2014).

28. Kornreich, M., Malka-Gibor, E., Zuker, B., Laser-Azogui, A. & Beck, R. Neurofilaments Function as Shock Absorbers: Compression Response Arising from Disordered Proteins. *Phys. Rev. Lett.* **117**, 1–5 (2016).

29. Uversky, V. N. Intrinsically disordered proteins from A to Z. *Int. J. Biochem. Cell Biol.* **43**, 1090–1103 (2011).

30. Shin, Y. & Brangwynne, C. P. Liquid phase condensation in cell physiology and disease. *Science.* **357**, (2017).

31. Uversky, V. N. & Dunker, A. K. Understanding protein non-folding. *Biochim. Biophys. Acta - Proteins Proteomics* **1804**, 1231–1264 (2010).

32. Das, R. K. & Pappu, R. V. Conformations of intrinsically disordered proteins are infl uenced by linear sequence distributions of oppositely charged residues. *Pnas* **110**, 13392–13397 (2013).

33. Meng, F., Uversky, V. N. & Kurgan, L. Comprehensive review of methods for prediction of intrinsic disorder and its molecular functions. *Cell. Mol. Life Sci.* **74**, 3069–3090 (2017).

34. Xue, B., Dunker, A. K. & Uversky, V. N. Retro-MoRFS: Identifying protein binding sites by normal and reverse alignment and intrinsic disorder prediction. *Int. J. Mol. Sci.* **11**, 3725–3747 (2010).

35. Yan, J., Dunker, A. K., Uversky, V. N. & Kurgan, L. Molecular recognition features (MoRFs) in three domains of life. *Mol. Biosyst.* **12**, 697–710 (2016).

36. Khan, W., Duffy, F., Pollastri, G., Shields, D. C. & Mooney, C. Predicting Binding within Disordered Protein Regions to Structurally Characterised Peptide-Binding Domains. *PLoS One* **8**, e72838 (2013).

37. Malhis, N., Jacobson, M. & Gsponer, J. MoRFchibi SYSTEM: software tools for the identification of MoRFs in protein sequences. *Nucleic Acids Res.* **44**, W488–W493 (2016).

38. Accardo, A., Leone, M., Tesauro, D., Aufiero, R., Bénarouche, A., Cavalier, J. F., Longhi, S., Carriere, F. & Rossi, F. Solution conformational features and interfacial properties of an intrinsically disordered peptide coupled to alkyl chains: A new class of peptide amphiphiles. *Mol. Biosyst.* **9**, 1401–1410 (2013).

39. Vincenzi, M., Accardo, A., Costantini, S., Scala, S., Portella, L., Trotta, A., Ronga, L., Guillon, J., Leone, M., Colonna, G., Rossi, F. & Tesauro, D. Intrinsically disordered amphiphilic peptides as potential targets in drug delivery vehicles. *Mol. Biosyst.* **11**, 2925–2932 (2015).

40. Klass, S. H., Smith, M. J., Fiala, T. A., Lee, J. P., Omole, A. O., Han, B. G., Downing, K. H., Kumar, S. & Francis, M. B. Self-Assembling Micelles Based on an Intrinsically Disordered Protein Domain. *J. Am. Chem. Soc.* **141**, 4291–4299 (2019).

41. De Yoreo, J. J. Principles of Crystal Nucleation and Growth. *Rev. Mineral. Geochemistry* **54**, 57–93 (2003).

42. Baumgartner, J., Dey, A., Bomans, P. H. H., Le Coadou, C., Fratzl, P., Sommerdijk, N. A. J. M. & Faivre, D. Nucleation and growth of magnetite from solution. *Nat. Mater.* **12**, 310–314 (2013).

43. Giuffre, A. J., Hamm, L. M., Han, N., De Yoreo, J. J. & Dove, P. M. Polysaccharide chemistry regulates kinetics of calcite nucleation through competition of interfacial energies. *Proc. Natl. Acad. Sci.* **110**, 9261–9266 (2013).

44. Hamm, L. M., Giuffre, A. J., Han, N., Tao, J., Wang, D., De Yoreo, J. J. & Dove, P. M. Reconciling disparate views of template-directed nucleation through measurement of calcite nucleation kinetics and binding energies. *Proc. Natl. Acad. Sci.* **111**, 1304–1309 (2014).

45. Zandi, R., van der Schoot, P., Reguera, D., Kegel, W. & Reiss, H. Classical Nucleation Theory of Virus Capsids. *Biophys. J.* **90**, 1939–1948 (2006).

46. Akella, S. V., Mowitz, A., Heymann, M. & Fraden, S. Emulsion-Based Technique To Measure Protein Crystal Nucleation Rates of Lysozyme. *Cryst. Growth Des.* **14**, 4487–4509 (2014).

47. Sleutel, M., Lutsko, J., Van Driessche, A. E. S., Durán-Olivencia, M. A. & Maes, D. Observing classical nucleation theory at work by monitoring phase transitions with molecular precision. *Nat. Commun.* **5**, 5598 (2014).

48. Sleutel, M. & Van Driessche, A. E. S. Role of clusters in nonclassical nucleation and growth of protein crystals. *Proc. Natl. Acad. Sci.* **111**, E546–E553 (2014).

49. De Yoreo, J. J., Gilbert, P. U. P. A., Sommerdijk, N. A. J. M., Penn, R. L., Whitelam, S., Joester, D., Zhang, H., Rimer, J. D., Navrotsky, A., Banfield, J. F., Wallace, A. F., Michel, F. M., Meldrum, F. C., Colfen, H. & Dove, P. M. Crystallization by particle attachment in synthetic, biogenic, and geologic environments. *Science.* **349**, aaa6760–aaa6760 (2015).

50. Loh, N. D., Sen, S., Bosman, M., Tan, S. F., Zhong, J., Nijhuis, C. A., Král, P., Matsudaira, P. & Mirsaidov, U. Multistep nucleation of nanocrystals in aqueous solution. *Nat. Chem.* **9**, 77–82 (2017).

51. Nishino, M., Enachescu, C., Miyashita, S., Rikvold, P. A., Boukheddaden, K. & Varret, F. Macroscopic nucleation phenomena in continuum media with long-range interactions. *Sci. Rep.* **1**, 1–5 (2011).

52. Neumann, D. A., McWhan, D. B., Littlewood, P., Aeppli, G., Remeika, J. P. & Maines, R. G. Nucleation near the tricritical point of BaTiO3. *Phys. Rev. B* **32**, 1866–1868 (1985).

53. Chandra, P. Nucleation in the presence of long-range interactions. *Phys. Rev. A* **39**, 3672–3681 (1989).

54. Tenchov, B. On the reversibility of the phase transitions in lipid-water systems. *Chem. Phys. Lipids* **57**, 165–177 (1991).

55. Seddon, J. M., Harlos, K. & Marsh, D. Metastability and polymorphism in the gel and fluid bilayer phases of dilauroylphosphatidylethanolamine. Two crystalline forms in excess water. *J. Biol. Chem.* **258**, 3850–3854 (1983).

56. Xu, H., Stephenson, F. A., Lin, H. & Ching-hsien, H. Phase metastability and supercooled metastable state of diundecanoylphosphatidylethanolamine bilayers. *Biochim. Biophys. Acta - Biomembr.* **943**, 63–75 (1988).

57. Lewis, R. N., Nanette Mak, N. M. & McElhaney, R. N. A Differential Scanning Calorimetric Study of the Thermotropic Phase Behavior of Model Membranes Composed of Phosphatidylcholines Containing Linear Saturated Fatty Acyl Chains. *Biochemistry* **26**, 6118–6126 (1987).

58. Reed, R. A. & Shipley, G. G. Structure and metastability of N-lignocerylgalactosylsphingosine (cerebroside) bilayers. *BBA - Biomembr.* **896**, 153–164 (1987).

59. Mantsch, H. H., Hsi, S. C., Butler, K. W. & Cameron, D. G. Studies on the thermotropic behavior of aqueous phosphatidylethanolamines. *BBA - Biomembr.* **728**, 325–330 (1983).

60. Serrallach, E. N., Shipley, G. G. & de Haas, G. H. Structure and Thermotropic Properties of Mixed-Chain Phosphatidylcholine Bilayer Membranes. *Biochemistry* **23**, 713–720 (1984).

61. Caffrey, M. The Study of Lipid Phase Transition Kinetics by Time-Resolved X-Ray Diffraction. *Annu. Rev. Biophys. Biophys. Chem.* **18**, 159–186 (1989).

62. Als-Nielsen, J. & McMorrow, D. *Elements of Modern X-ray Physics*. (Wiley, 2011).

63. Pauw, B. R. Everything SAXS: Small-angle scattering pattern collection and correction. *J. Phys. Condens. Matter* **25**, 383201 (2013).

64. Nagle, J. F. & Tristram-Nagle, S. Structure of lipid bilayers. *Biochim. Biophys. Acta - Rev. Biomembr.* **1469**, 159–195 (2000).

65. Pabst, G., Rappolt, M., Amenitsch, H. & Laggner, P. Structural information from multilamellar liposomes at full hydration: Full q-range fitting with high quality X-ray data. *Phys. Rev. E - Stat. Physics, Plasmas, Fluids, Relat. Interdiscip. Top.* **62**, 4000–4009 (2000).

66. Zhang, R., Suter, R. M. & Nagle, J. F. Theory of the structure factor of lipid bilayers. *Phys. Rev. E* **50**, 5047–5060 (1994).

67. Pabst, G., Koschuch, R., Pozo-Navas, B., Rappolt, M., Lohner, K. & Laggner, P. Structural analysis of weakly ordered membrane stacks. *J. Appl. Crystallogr.* **36**, 1378–1388 (2003).

68. Heftberger, P., Kollmitzer, B., Heberle, F. A., Pan, J., Rappolt, M., Amenitsch, H., Kučerka, N., Katsaras, J. & Pabst, G. Global small-angle X-ray scattering data analysis for multilamellar vesicles: the evolution of the scattering density profile model. *J. Appl. Crystallogr.* **47**, 173–180 (2014).

69. Ben-Nun, T., Ginsburg, A., Székely, P. & Raviv, U. X+ : a comprehensive computationally accelerated structure analysis tool for solution X-ray scattering from supramolecular self-assemblies. *J. Appl. Crystallogr.* **43**, 1522–1531 (2010).

70. Li, Y., Beck, R., Huang, T., Choi, M. C. & Divinagracia, M. Scatterless hybrid metal–single-crystal slit for small-angle X-ray scattering and high-resolution X-ray diffraction. *J. Appl. Crystallogr.* **41**, 1134–1139 (2008).

71. Bellare, J. R., Davis, H. T., Scriven, L. E. & Talmon, Y. Controlled environment vitrification system: An improved sample preparation technique. *J. Electron Microsc. Tech.* **10**, 87–111 (1988).

72. Danino, D. Cryo-TEM of soft molecular assemblies. *Curr. Opin. Colloid Interface Sci.* **17**, 316–329 (2012).

73. Kelly, S. M., Jess, T. J. & Price, N. C. How to study proteins by circular dichroism. *Biochim. Biophys. Acta - Proteins Proteomics* **1751**, 119–139 (2005).

74. Jacoby, G., Cohen, K., Barkan, K., Talmon, Y., Peer, D. & Beck, R. Metastability in lipid based particles exhibits temporally deterministic and controllable behavior. *Sci. Rep.* **5**, 9481 (2015).

75. Jacoby, G., Portnaya, I., Danino, D., Diamant, H. & Beck, R. Delayed nucleation in lipid particles. *Soft Matter* **16**, 247–255 (2020).

76. Chang, H. & Epand, R. M. The existence of a highly ordered phase in fully hydrated dilauroylphosphatidylethanolamine. *Biochim. Biophys. Acta - Biomembr.* **728**, 319–324 (1983).

77. Tari, A. & Huang, L. Structure and function relationship of phosphatidylglycerol in the stabilization of phosphatidylethanolamine bilayer. *Biochemistry* **28**, 7708–7712 (1989).

78. Rivkin, I., Cohen, K., Koffler, J., Melikhov, D., Peer, D. & Margalit, R. Paclitaxel-clusters coated with hyaluronan as selective tumor-targeted nanovectors. *Biomaterials* **31**, 7106–7114 (2010).

79. Bachar, G., Cohen, K., Hod, R., Feinmesser, R., Mizrachi, A., Shpitzer, T., Katz, O. & Peer, D. Hyaluronan-grafted particle clusters loaded with Mitomycin C as selective nanovectors for primary head and neck cancers. *Biomaterials* **32**, 4840–4848 (2011).

80. Cohen, K., Emmanuel, R., Kisin-Finfer, E., Shabat, D. & Peer, D. Modulation of Drug Resistance in Ovarian Adenocarcinoma Using Chemotherapy Entrapped in Hyaluronan-Grafted Nanoparticle Clusters. *ACS Nano* **8**, 2183–2195 (2014).

81. Rand, R. P. & Parsegian, V. A. Hydration forces between phospholipid bilayers. *BBA - Rev. Biomembr.* **988**, 351–376 (1989).

82. Helfrich, W. & Servuss, R. M. Undulations, steric interaction and cohesion of fluid membranes. *Nuovo Cim. D* **3**, 137–151 (1984).

83. McIntosh, T. J. & Simon, S. A. Area per Molecule and Distribution of Water in Fully Hydrated Dilauroylphosphatidylethanolamine Bilayers. *Biochemistry* **25**, 4948–4952 (1986).

84. Pan, J., Heberle, F. A., Tristram-Nagle, S., Szymanski, M., Koepfinger, M., Katsaras, J. & Kučerka, N. Molecular structures of fluid phase phosphatidylglycerol bilayers as determined by small angle neutron and X-ray scattering. *Biochim. Biophys. Acta - Biomembr.* **1818**, 2135–2148 (2012).

85. Tayebi, L., Ma, Y., Vashaee, D., Chen, G., Sinha, S. K. & Parikh, A. N. Long-range interlayer alignment of intralayer domains in stacked lipid bilayers. *Nat. Mater.* **11**, 1074–1080 (2012).

86. Hoshino, T., Komura, S. & Andelman, D. Correlated lateral phase separations in stacks of lipid membranes. *J. Chem. Phys.* **143**, 243124 (2015).

87. Kornreich, M., Avinery, R., Malka-Gibor, E., Laser-Azogui, A. & Beck, R. Order and disorder in intermediate filament proteins. *FEBS Lett.* **589**, 2464–2476 (2015).

88. Laser-Azogui, A., Kornreich, M., Malka-Gibor, E. & Beck, R. Neurofilament assembly and function during neuronal development. *Curr. Opin. Cell Biol.* **32**, 92–101 (2015).

89. Kornreich, M., Malka-Gibor, E., Laser-Azogui, A., Doron, O., Herrmann, H. & Beck, R. Composite bottlebrush mechanics: α-internexin fine-tunes neurofilament network properties. *Soft Matter* **11**, 5839–5849 (2015).

90. Malka-Gibor, E., Kornreich, M., Laser-Azogui, A., Doron, O., Zingerman-Koladko, I., Harapin, J., Medalia, O. & Beck, R. Phosphorylation-Induced Mechanical Regulation of Intrinsically Disordered Neurofilament Proteins. *Biophys. J.* **112**, 892–900 (2017).

91. Black, M., Trent, A., Kostenko, Y., Lee, J. S., Olive, C. & Tirrell, M. Self-assembled peptide amphiphile micelles containing a cytotoxic T-cell epitope promote a protective immune response in vivo. *Adv. Mater.* **24**, 3845–3849 (2012).

92. Ishida, T. & Kinoshita, K. PrDOS: prediction of disordered protein regions from amino acid sequence. *Nucleic Acids Res.* **35**, W460–W464 (2007).

93. Klausen, M. S., Jespersen, M. C., Nielsen, H., Jensen, K. K., Jurtz, V. I., Sønderby, C. K., Sommer, M. O. A., Winther, O., Nielsen, M., Petersen, B. & Marcatili, P. NetSurfP-2.0: Improved prediction of protein structural features by integrated deep learning. *Proteins Struct. Funct. Bioinforma.* **87**, 520–527 (2019).

94. Konarev, P. V., Volkov, V. V., Sokolova, A. V., Koch, M. H. J. & Svergun, D. I. PRIMUS: A Windows PC-based system for small-angle scattering data analysis. *J. Appl. Crystallogr.* **36**, 1277–1282 (2003).

95. Harpaz, Y., Gerstein, M. & Chothia, C. Volume changes on protein folding. *Structure* **2**, 641–649 (1994).

96. Putnam, C. D., Hammel, M., Hura, G. L. & Tainer, J. A. X-ray solution scattering (SAXS) combined with crystallography and computation: Defining accurate macromolecular structures, conformations and assemblies in solution. *Q. Rev. Biophys.* **40**, 191–285 (2007).

97. Lerche, D., Kozlov, M. M. & Markin, V. S. Electrostatic free energy and spontaneous curvature of spherical charged layered membrane. *Biorheology* **24**, 23–34 (1987).

98. Bassereau, P. & Sens, P. *Physics of Biological Membranes* (Springer International Publishing, 2018).

99. Rawicz, W., Olbrich, K. C., McIntosh, T., Needham, D. & Evans, E. A. Effect of chain length and unsaturation on elasticity of lipid bilayers. *Biophys. J.* **79**, 328–339 (2000).

100. Beck, R., Deek, J., Jones, J. B. & Safinya, C. R. Gel-expanded to gel-condensed transition in neurofilament networks revealed by direct forcemeasurements. *Nat. Mater.* **9**, 40–46 (2010).

101. Littlewood, P. B. & Chandra, P. Delayed Nucleation at a Weakly First-Order Transition. *Phys. Rev. Lett.* **57**, 2415–2418 (1986).

102. DeForte, S. & Uversky, V. N. Order, disorder, and everything in between. *Molecules* **21**, 1090 (2016).

103. Uversky, V. N. Intrinsically disordered proteins and their ‘Mysterious’ (meta)physics. *Front. Phys.* **7**, 8–23 (2019).

104. Sarkar, Y., Majumder, R., Das, S., Ray, A. & Parui, P. P. Detection of Curvature-Radius-Dependent Interfacial pH/Polarity for Amphiphilic Self-Assemblies: Positive versus Negative Curvature. *Langmuir* **34**, 6271–6284 (2018).

105. Wang, D., Nap, R. J., Lagzi, I., Kowalczyk, B., Han, S., Grzybowski, B. A. & Szleifer, I. How and why nanoparticle’s curvature regulates the apparent pKa of the coating ligands. *J. Am. Chem. Soc.* **133**, 2192–2197 (2011).

106. Nap, R., Gong, P. & Szleifer, I. Weak polyelectrolytes tethered to surfaces: Effect of geometry, acid–base equilibrium and electrical permittivity. *J. Polym. Sci. Part B Polym. Phys.* **44**, 2638–2662 (2006).

107. Harnoy, A. J., Rosenbaum, I., Tirosh, E., Ebenstein, Y., Shaharabani, R., Beck, R. & Amir, R. J. Enzyme-responsive amphiphilic PEG-dendron hybrids and their assembly into smart micellar nanocarriers. *J. Am. Chem. Soc.* **136**, 7531–7534 (2014).

108. Segal, M., Avinery, R., Buzhor, M., Shaharabani, R., Harnoy, A. J., Tirosh, E., Beck, R. & Amir, R. J. Molecular precision and enzymatic degradation: From readily to undegradable polymeric micelles by minor structural changes. *J. Am. Chem. Soc.* **139**, 803–810 (2017).

109. Rosenbaum, I., Avinery, R., Harnoy, A. J., Slor, G., Tirosh, E., Hananel, U., Beck, R. & Amir, R. J. Reversible Dimerization of Polymeric Amphiphiles Acts as a Molecular Switch of Enzymatic Degradability. *Biomacromolecules* **18**, 3457–3468 (2017).

תקציר

אמפיפילים הן מולקולות בעלות קבוצות כימיות הידרופיליות והידרופוביות. מאפיין זה מקנה להן את תכונת ההתארגנות העצמית או *הרכבה עצמית* למגוון מבנים, כגון מיצלות, בועיות, מוטות או מבנים המשכיים. הצבירים המולקולריים האלה, אשר ידועים בתור מצבי-צבירה ביניים, מצויים באופן נרחב בטבע, למשל בקרום התא או גרעין התא. אמפיפילים משמשים גם ביישומים שונים בתחום הננו-טכנולוגיה, ביו-רפואה ומדע החומרים.

האנרגיה החופשית התרמודינמית של הרכבה עצמית יכולה להיות מונעת על ידי אנתלפיה או אנטרופיה, אך לרוב היא מאופיינת באינטראקציות חלשות יותר, לא-קוולנטיות, כמו ואן דר וואלס, קשרי מימן או כוחות אנטרופיים. מערכות הרכבה עצמית מאופיינות גם ביציבות התרמודינמית שלהן, כלומר המבנים המורכבים יציבים תרמודינמית בהשוואה למולקולות בודדות. שתי תכונות אלה מובילות מערכות הרכבה עצמית להיות רגישות לסביבה החיצונית, אך גם גמישות לסידור מחדש של המולקולות למבנים חדשים, כפי שנקבע על ידי התרמודינמיקה.

מעברים בין מצבי צבירה במערכות הרכבה עצמית יכולים להתבצע בתגובה לשינויים במשתנים תרמודינמיים, כמו טמפרטורה ולחץ, או בתנאי הסביבה של המערכת, כגון ריכוז המלחים או רמת החומציות. ניתן להשתמש בפרמטרים אלה כדי לבדוק את התנהגות מצבי הצבירה של המערכת, ללמוד את תכונותיה הפיזיות הייחודיות ולבחון את ישימותה.

אף על פי שמעברי מצב צבירה במערכות אמפיפיליות נחקרו בהרחבה, ורבים מהם ניתנים לתאר באמצעות מודלים תיאורטיים מבוססים, מערכות חדשות המציגות דינמיקה לא קלאסית מהוות אתגר מעניין. בעבודה זו בחנתי באופן ניסויי שני סוגים של אמפיפילים ואת תכונות מעברי מצב הצבירה שלהם באמצעות טכניקות שונות של אפיון חומר רך. בנוסף, אני מציע מודל לתיאור כל אחד מהמנגנונים העומדים בבסיסם ואת מאפייניהם.

המערכת האמפיפילית הראשונה מורכבת מפוספוליפידים, מולקולות ביולוגיות טבעיות הידועות ביותר כמרכיב העיקרי של קרום התא. באופן ספציפי, אני חוקר באופן ניסויי מצב צבירה גבישי-נוזלי יציב למחצה , בעל אורך חיים של עשרות שעות ויותר, ואת המעבר הקואופרטיבי שלו למצב הצבירה הגבישי היציב. אני מראה שיש כמה סקלות זמנים הקשורות לדינמיקה של התופעה, בניגוד למה שצפוי מהתיאוריה הקלאסית של התגרענות. אני מראה כי היציבות של מצב הצבירה הגבישי-נוזלי ניתנת לשליטה על ידי שינוי פרמטרי מערכת שונים, כגון מספר סוגי המולקולות, ריכוז המלחים וטמפרטורת היעד. אני מפרט מודל המתאר את המנגנון שמאחורי העיכוב בהתגבשות; מנגנון שניתן להכליל למערכות עם תכונות דומות.

הסוג השני של אמפיפיל שנחקר בעבודה זו הוא מולקולה סינתטית היברידית, בעלת פפטיד לא מסודר כקבוצת ראש ושרשראות פחמימניות דומות לאלו של פוספוליפידים. מולקולה זו, השייכת לקבוצה שנחקרת לאחרונה בשם אמפיפילים פפטידיים, תוכננה עם שתי מטרות. הראשונה היא להשתמש בהרכבה העצמית שלה כדי לחקור את האינטראקציות בין סוג נוסף ומעניין של מולקולות - חלבונים לא מסודרים. המטרה השנייה, התואמת יותר לעבודות שפורסמו לאחרונה, היא לתכנן אמפיפילים פפטידיים חדשים ליישומים ביו-רפואיים.

אני חוקר באופן ניסויי שתי גרסאות של אמפיפילים פפטידיים ומראה את קיומו של מעבר מצב צבירה מבני ממיצלות למבניים גליליים, שנגרם על ידי שינוי ברמת החומציות. אני מציג מודל אנרגיה חופשית לתאר את האיזון בין כוחות אלקטרוסטטיים ואלסטיים, שיכול להביא למעבר. בנוסף, אני משתמש במודל כדי לחזות אינטראקציות ספציפיות לרצף הפפטידי בין קבוצות ראש פפטידיות שכנות במבנים המורכבים. בהתבסס על התחזיות, הוכנסו שני שינויים

בפפטיד של קבוצת הראש, שהביאו לשינויים מקרוסקופיים באינטראקציות בין המבנים. שינויים אלה מדגישים את הרגישות של מאפייני ההרכבה לאינטראקציות של קבוצות הראש.

הממצאים המוצגים בעבודה זו מדגימים את העושר והמורכבות שאנו נתקלים במחקר מעברי מצב צבירה במערכות אמפיפיליות. מצד אחד, גם מערכות שניתן לחשוב עליהן שנחקרו בצורה ממצה יכולות להציג דינמיקה ייחודית וחדשה. מצד שני, אני מאמין שמערכות אמפיפיליות, ובמיוחד אמפיפילים פפטידיים, רק התחילו להראות את הפוטנציאל האמיתי שלהן, וכי עבודתי תעזור לסלול את הדרך למחקרים עתידיים על השימוש בהן ביישומים ביו-רפואיים.

עבודה זו נעשתה בהנחיית פרופ' רועי בק.

מעברי-פאזה במערכות הרכבה עצמית אמפיפיליות

חיבור לשם קבלת התואר

"דוקטור לפילוסופיה"

מאת

גיא יעקבי

בהנחיית

פרופ' רועי בק

הוגש לסנאט של אוניברסיטת תל אביב

מאי 2020